# UNIVERSITÉ DE STRASBOURG

***ÉCOLE DOCTORALE MATHÉMATIQUES, SCIENCES DE L'INFORMATION ET DE L'INGÉNIEUR***

**LABORATOIRE ICUBE UMR 7357**

# THESIS DISSERTATION by:


## Silvère SÉGAUD


Defended on: **April 6th, 2022**

Pour obtenir le grade de : **Docteur de l'Université de Strasbourg**

Discipline/ Spécialité : Physique, Photonique

# Multispectral Optical Imaging in Real-Time for Surgery

**DIRECTORS:**

| | |
|---|---|
| **GIOUX Sylvain** | Professor, Université de Strasbourg |
| **LECLER Sylvain** | Professor, INSA Strasbourg |

**REVIEWERS:**

| | |
|---|---|
| **BLONDEL Walter** | Professor, Université de Lorraine, Nancy |
| **VIBERT Éric** | Professor, M.D., Hôpital Paul Brousse, Villejuif |

---

**INVITED JURY MEMBERS:**

| | |
|---|---|
| **VAHRMEIJER Alexander** | M.D., Ph.D., Leiden University Medical Center |
| **DIANA Michele** | M.D., Ph.D., IRCAD Strasbourg |

# Acknowledgments

Before presenting this thesis work and my personal contributions to it, I will dedicate this one page to briefly express my thankfulness towards everyone who enabled, participated in or facilitated this work.

First of all, I would like to sincerely thank the members of the jury: Pr. Walter Blondel, Pr. Éric Vibert, Dr. Alexander Vahrmeijer and Dr. Michele Diana; for their interest in this thesis work, their insightful feedback and future discussions we will have following reading this manuscript.

Next, I would send my thesis directors my gratefulness for all I could learn during my time at the lab and the work we accomplished. To Sylvain Gioux, for welcoming me into your lab, for your mentorship, insight, dedication, but also incredible amount of time, energy, and resources I benefited from you. To Sylvain Lecler, for your cheerfulness, insight, and watchful eye seeing my work through a different prism.

No matter how exciting or inspiring a project can be, being surrounded by amazing people makes all the difference. I warmly thank my dear colleagues and friends at the Institut de Physique Biologique, present and former: Luca, Agathe, Emmanuel, Fabrice, Amir, Jesse, Sara, Joseph, Jason, Henrique, Murielle, Lucille… I will surely miss sharing offices, flammkuchen, optical benches, beers, lab meetings and coffee breaks with you.

Many thanks to the fellow ICube members from the Institut de Physique Biologique and staff, for the cheerful hallway chat, assistance and support. Special thanks go to Christelle, for flawlessly managing the countless orders we kept sending your way.

I have been lucky to step into the world of cutting-edge image-guided surgery, in the company of my favorite surgeons and collaborators from IRCAD: Rita and Nariaki; and from LUMC: Labrinus, Lizzie and Sven. To Pablo, thank you the vivid and fruitful discussions we could have, the time and efforts you put into giving me precious insight. Finally, I could not thank enough the all the staff from IHU and IRCAD, for providing us with amazing working conditions.

Last but not least, I would like to conclude these acknowledgments with special thoughts for my family and friends, for their constant support and encouragement, as always.

# Abstract

The deployment of technology in operating rooms dramatically accelerated over the last decades. However, surgeons still mostly rely on their senses (vision and touch) combined with their own experience to navigate the surgical field. In other words, their ability to distinguish healthy from diseased tissues is based on subjective inputs. Tissue status assessment is of utmost importance in oncologic surgery, both for resecting target tissues (e.g. tumors) or for avoiding critical structures (e.g. vessels). Such subjectivity to guide decision-making is leading to high failure rates and healthcare costs. Thus, the ability to objectively assess the tissues intraoperatively and in real-time over a large field is crucial for improving surgical outcomes.

Near-infrared (NIR) imaging can be employed to probe the tissues in depth in a non-contact and safe manner. When travelling through tissues, light interacts with molecular compounds and the tissue microstructures. These interactions are characterized by optical properties – namely absorption and scattering. The family of methods measuring optical properties over a wide field of view (> 100 $cm^2$) are gathered in the domain called diffuse optical imaging (DOI). DOI methods enable the measurement of chromophore concentrations and the study of tissue microstructure. Additionally, fluorescent contrast agents may be employed to highlight anatomical structures or investigate physiological activities.

Spatial Frequency Domain Imaging (SFDI) is a DOI method well-suited for real-time quantitative imaging of optical properties. Measuring these properties at several wavelengths allows to extract the concentrations of the molecular compounds such as hemoglobin, lipids or water. In turn, SFDI is capable of measuring the oxygenation of tissue, as an indicator of blood perfusion. Additionally, fluorescence imaging and laser speckle imaging (LSI) can be employed to assess blood perfusion by highlighting vessels and measuring blood flow, respectively. Blood perfusion assessment is a longstanding issue that could benefit from additional objective input in real-time, from both functional and structural imaging modalities.

The lack of tools for biological intraoperative tissue status assessment has been the main source of motivation for this doctoral project. To address this need, a clinically-compatible imaging platform has been developed for oxygenation and fluorescence imaging in real-time. Its design makes it effortlessly integrated into the surgical workflow while providing the surgeons with critical input regarding the surgical procedures. The capability of the platform to detect and quantify ischemia has been demonstrated through preclinical trials, by comparison with standard of care methods. A field of application is blood perfusion assessment for reconstructive procedures in the context of colorectal cancer surgery. Such technique bears potential for multiple additional applications, such as hepatic transplantation.

The multimodal nature of the developed imaging device has been exploited by combining endogenous imaging of optical properties with exogenous fluorescence imaging, in the context of oncologic surgery. A fluorescence quantification technique validated in preclinical trials with colorectal and pancreatic cancer

models, highlighting the limitations of conventional fluorescence imaging. In order to take further the clinical translation of this technique, a real-time implementation should be tested and validated.

**Keywords**: Image-guided surgery, Oxygenation imaging, Fluorescence imaging, Clinical translation, Spatial Frequency Domain Imaging, Diffuse Optical imaging

# Résumé

Le développement technologique des salles d'opérations a accéléré de manière spectaculaire ces dernières années. Cependant, les chirurgiens basent leur navigation à travers le champ chirurgical principalement sur leur perception au toucher et à la vue, et leur expérience. En conséquence, une évaluation subjective guide le geste chirurgical et impacte notamment la capacité des praticiens à différencier les tissus sains des tissus malsains. Ceci est pourtant d'une importance majeure en chirurgie oncologique, tant pour la résection de tumeurs que pour les actes de reconstruction. Cet impact sur la prise de décision se traduit par de hauts taux d'échec et des coûts importants pour le système de santé. C'est pourquoi la capacité d'évaluer le statut des tissus biologiques à travers des zones étendues en temps réel est cruciale.

L'imagerie proche-infrarouge peut être employée pour sonder les tissus sans contact en toute sécurité. En se propageant dans les tissus, la lumière interagit avec les composants moléculaires et microstructures présents. Ces interactions sont caractérisées par les propriétés optiques des tissus, notamment l'absorption et la diffusion. Les méthodes permettant la mesure des propriétés optiques à travers de larges champs de vue (> 100 $cm^2$) sont regroupées sous le terme d'optique diffuse. L'optique diffuse permet la mesure de concentrations de chromophores et l'étude de microstructures au sein des tissus. De plus, l'utilisation d'agents de contraste fluorescents permet la mise en évidence de structures anatomiques et l'étude d'activités physiologiques.

Spatial Frequency Domain Imaging (SFDI) est une technique d'optique diffuse particulièrement adaptée pour la mesure quantitative des propriétés optiques en temps-réel. De la mesure de ces paramètres à plusieurs longueurs d'onde peuvent être extraites les concentrations de composants moléculaires tels que l'hémoglobine, les lipides ou l'eau. En conséquence, la méthode SFDI est capable de mesurer l'oxygénation des tissus, reflétant la perfusion sanguine. De plus, l'imagerie de fluorescence et l'imagerie de speckle peuvent être employées respectivement pour détecter les vaisseaux et mesurer les flux sanguins. L'évaluation de la perfusion sanguine est une procédure à l'impact critique pour lesquelles une objectivité accrue serait bénéfique, de par l'apport d'informations objectives en temps-réel, provenant de modalités d'imagerie structurelles et fonctionnelles.

Le manque d'outils permettant l'évaluation de la viabilité des tissus biologique dans un contexte intra opératoire a été la motivation principale de ce projet. Un prototype d'imageur multimodal clinique a été développé pour l'imagerie d'oxygénation et de fluorescence en temps-réel. Son implémentation particulière permet de minimiser les interférences avec le processus chirurgical tout en apportant des informations cruciales pour le bon déroulement des procédures. La capacité de la plateforme à quantifier l'ischémie a été démontrée lors de tests précliniques, par comparaison avec les méthodes standards. Un champ d'application visé est l'évaluation de la perfusion sanguine lors de procédures de reconstruction

dans les chirurgies du cancer colorectal. Une telle méthode serait également très prometteuse pour suivre les procédures de transplantation hépatique.

Le caractère multimodal de la plateforme d'imagerie a été exploité pour combiner l'imagerie endogène mesurant les propriétés optiques des tissus et l'imagerie exogène par fluorescence, dans le cadre de la chirurgie du cancer. Une méthode de quantification a été employée lors d'essais précliniques sur des modèles de cancers colorectaux et pancréatiques, mettant en évidence les défaillances de l'imagerie de fluorescence conventionnelle. Afin de poursuivre la translation clinique d'une telle technique, il serait néanmoins nécessaire d'en réaliser une implémentation fonctionnant en temps-réel.

**Mots-clés** : Chirurgie guidée par l'image, Imagerie d'oxygénation, Imagerie de fluorescence, Translation clinique, Spatial Frequency Domain Imaging, Optique diffuse

# Table of contents

# List of figures

# List of tables

# Acronyms and abbreviations

| | |
|---|---|
| **2D** | Two-Dimensional |
| **3D** | Three-Dimensional |
| **AC** | Alternating current |
| **AI** | Artificial Intelligence |
| **AL** | Anastomotic Leak |
| **APD** | Avalanche PhotoDiode |
| **AR** | Augmented Reality |
| **BGA** | Blood Gas Analysis |
| **BOLD** | Blood-Oxygen-Level Dependent |
| **CB** | Control Biopsy |
| **CLE** | Confocal Laser Endomicroscopy |
| **CNN** | Convolutional Neural Network |
| **CT** | Computed Tomography |
| **CW** | Continuous-Wave |
| **DA** | Diffusion Approximation |
| **DC** | Direct Current |
| **DL** | Deep Learning |
| **DMD** | Digital Micromirror Device |
| **DMSO** | DiMethyl SulfOxide |
| **DOI** | Diffuse Optical Imaging |
| **EAES** | European Association of Endoscopic Surgery |
| **EMA** | European Medicines Agency |
| **EpCAM** | Epithelial Cell Adhesion Molecule |
| **FA** | Fluorescence Angiography |
| **FD** | Frequency Domain |
| **FDA** | Food and Drugs Administration |
| **Fe** | Iron atom |
| **FI** | Fluorescence Imaging |
| **FIGS** | Fluorescence Image-Guided Surgery |
| **FLER** | FLuorescence-based Enhanced Reality |

| | |
|---|---|
| **fMRI** | functional Magnetic Resonance Imaging |
| **fNIR** | functional Near-InfraRed |
| **FOV** | Field Of View |
| **GB** | GigaByte |
| **GC** | Gastric Conduit |
| **GPU** | Graphics Processing Unit |
| **$H_2O$** | Water molecule |
| **Hb** | Hemoglobin |
| **$HbO_2$** | Oxygenated Hemoglobin |
| **HE** | Hematoxylin-Eosin |
| **HHb** | Deoxygenated Hemoglobin |
| **HSI** | Hyperspectral Imaging |
| **HYPER** | HYPerspectral Enhanced Reality |
| **ICG** | IndoCyanine Green |
| **IHU** | Insitut Hospitalo-Universitaire |
| **IRCAD** | Institut de Recherche contre les Cancers de l'Appareil Digestif |
| **LCL** | Local Capillary Lactates |
| **LD** | Laser Diode |
| **LED** | Light-Emitting Diode |
| **LSI** | Laser Speckle Imaging |
| **LUT** | Look-Up Table |
| **MB** | Methylene Blue |
| **MC** | Monte Carlo |
| **MESR** | Ministère de l'Enseignement Supérieur et de la Recherche |
| **MHz** | MegaHertz |
| **MIS** | Minimally Invasive Surgery |
| **MP** | Mega Pixel |
| **MPE** | Mean Percentage Error |
| **MRI** | Magnetic Resonance Imaging |
| **MSI** | MultiSpectral Imaging |
| **MTF** | Modulation Transfer Function |
| **NBI** | Narrow-Band Imaging |

| | |
|---|---|
| **NIR** | Near-InfraRed |
| **NIRS** | Near-InfraRed Spectroscopy |
| **NMR** | Nuclear Magnetic Resonance |
| **$O_2$** | Dioxigen molecule |
| **OCT** | Optical Coherence Tomography |
| **OP** | Optical Properties |
| **PCA** | Principal Component Analysis |
| **PD** | PhotoDiode |
| **PET** | Positron-Emission Tomography |
| **PMT** | PhotoMultiplier Tube |
| **PpIX** | Protoporphyrin IX |
| **QuantSURG** | Quantitative Surgical Guidance for colorectal surgery |
| **RAM** | Random Access Memory |
| **RGB** | Red Green Blue |
| **ROI** | Region Of Interest |
| **RTE** | Radiative Transfer Equation |
| **SD** | Standard Deviation |
| **SEM** | Standard Error of Mean |
| **SFDI** | Spatial Frequency Domain Imaging |
| **s-MTF** | spatial Modulation Transfer Function |
| **SNL** | Sentinel Lymph Node |
| **SPECT** | Single Photon Emission Computed Tomography |
| **s-PSF** | Spatial Point-Spread Function |
| **SRS** | Spatially Resolved Spectroscopy |
| **SSOP** | Single Snapshot of Optical Properties |
| **$StO_2$** | Oxygen Saturation |
| **TB** | TeraByte |
| **TBR** | Tumor-to-Background Ratio |
| **TCSPC** | Time-Correlated Single Photon Counting |
| **TD** | Time Domain |
| **TEC** | ThermoElectric Cooler |
| **$TiO_2$** | Titanium dioxide |

| | |
|---|---|
| **t-MTF** | temporal Modulation Transfer Function |
| **ToF** | Time-of-Flight |
| **t-PSF** | temporal Point-Spread Function |
| **USAF** | United States Air Force |
| **USB** | Universal Serial Bus |

# Introduction

Innovation in healthcare is driven by the need for optimizing the care provided to patients. Among others, effectiveness, efficiency, safety and affordability are levers to be actuated to improve healthcare, by joining efforts from scientific, business, and social fields. Scientific and technological innovation consists in the creation, adoption and diffusion of new technologies and products, with the prime objective of offering clear benefits compared to currently available solutions.

Over the last decades, the field of surgery has dramatically evolved, marked by successive technological breakthroughs. The massive deployment of imaging technologies throughout a patient's surgical journey for diagnostic, surgery planning and post-surgery monitoring purposes improved the overall health outcome, but also drastically impacted the surgical workflow [1]. However, despite these transformations, intraoperative navigation of the surgical field and decision-making remain based on the surgeons' perception and experience. Consequently, their ability to distinguish diseased from healthy tissue and vital structures are based on subjective inputs, leading to high failure rates and healthcare costs. Tissue status assessment is of utmost importance in oncologic surgery, both for tumor resection and reconstructive procedures [2]. Thus, the ability to intraoperatively probe and assess the tissue objectively and in real-time over large areas is crucial. This longstanding issue constitutes an unmet clinical need, calling for innovation.

When travelling through biological tissues, photons undergo a series of physical phenomena, through interactions with the various constituents of the tissues. These interactions are characterized by optical properties – namely absorption and scattering – reflecting the presence of molecular compounds and microstructural features within the tissues, respectively. These compounds and structures have specific spectral signatures, causing a wavelength dependency in the overall tissue optical properties. Non-invasive observation of the tissues coupled to light propagation models enable the measurement of these optical properties, eventually yielding extraction of compounds concentrations such as hemoglobin, lipids or water, but also identification of the tissue type [3]. This observation in biological tissues is best favored in the near-infrared (NIR) wavelength range (600 to 1000 nm) where it benefits from a transparency window: typically low absorption and scattering facilitate the deeper penetration of photons.

In turn, a wide array of NIR optical spectroscopy methods emerged for the non-invasive investigation of tissues [4]. While the first developed systems were limited to qualitative measurements using point probes, quantitative mapping of functional parameters has witnessed a very rapid growth, paving the way for advanced optical technologies into clinical use. However, point probes methods present critical limitations such as the need for contact with the patient, the limited area of investigation, the long time required to extract the results and their cumbersome implementation.

The introduction of a widefield, non-contact and quantitative method named Spatial Frequency Domain Imaging (SFDI) drafted a solution to overcome the limitations of conventional NIR spectroscopy techniques [5]. By using spatially structured illumination and a camera, optical properties imaging over large areas can be achieved with high resolution and rapidly. Oxygenation imaging was performed using SFDI at several wavelengths (i.e. multispectral), and validated in clinical settings for blood perfusion assessment [6]. While the current standards of care are based on invasive tissue and blood sampling, or exogenous fluorescence imaging to highlight blood flow, SFDI provides an endogenous non-invasive imaging alternative for blood perfusion assessment. However, this method was not yet suitable for intraoperative use, with data acquisition and processing being rapid but not real-time.

A series of technological breakthroughs improved the capabilities of SFDI by first introducing a real-time compatible implementation named Single Snapshot imaging of Optical Properties (SSOP) [7]. The use of high-performance parallel computing further improved the SSOP workflow, yielding video-rate optical properties imaging [8]. Ultimately, a deep learning implementation of SSOP has been developed, producing high-quality real-time imaging [9]. The demonstration of this real-time implementation in clinical settings and validation by comparison with gold standards is key for its clinical translation.

Based on these observations, the end goal of this thesis work has been set to enable the clinical translation of state-of-the-art technologies for tissue status assessment. To this purpose, a multimodal imaging platform dedicated to the clinical environment has been developed. This platform implements the latest available technologies for oxygenation imaging in real-time. Secondly, the versatility of the platform has enabled the demonstration of quantitative fluorescence imaging. With upcoming tumor-targeting tracers, quantification might be required to circumvent the qualitative nature of conventional fluorescence imaging. This manuscript presents the achieved work according to the following structure:

- Chapter I provides an overview of medical imaging for surgery. Each surgical phase can be assisted using imaging modalities. A comparison of these for intraoperative use is established, considering specific constraints relative to unmet clinical needs. A number of criteria designate NIR optical imaging as most the suitable candidate for intraoperative imaging.
- Chapter II covers the fundamentals of light-matter interactions and basics of light propagation modeling in biological tissues. This lays foundation for understanding the different established methods for tissue optical characterization, especially in the NIR range.
- Chapter III introduces advanced NIR optical imaging techniques for tissue status assessment. Endogenous imaging yielding physiological parameters for hemodynamics monitoring is presented. Exogenous imaging highlighting vital structures and its application for tumor surgery is detailed. A selection of available imaging systems is presented to depict a set of currently deployed tools.
- Chapter IV emphasizes various limitations of the standard of care and states corresponding work objectives to bring novel solutions.

- Chapter V presents the main contribution of this work with the development of a novel clinically-compatible multimodal imaging platform. The validation for real-time oxygenation and fluorescence imaging *in-vitro* and *in-vivo* is detailed.
- Chapter VI reports results of preclinical trials for blood perfusion assessment in the small bowel, yielding validation of oxygenation imaging as a label-free ischemia quantification method. These results were correlated to the analysis of robust biomarkers such as local capillary lactates.
- Chapter VII extends the validation of the imaging platform and oxygenation imaging to ischemia monitoring in the stomach for esophagectomy purposes. Further blood gas analysis and histologic analysis confirmed the correlation with local capillary lactates, comforting the position of oxygenation imaging as a strong tool for blood perfusion assessment.
- Chapter VIII demonstrates the combination of endogenous and exogenous imaging using the multimodal platform, yielding quantitative fluorescence imaging for tumor surgery. The potential for tumor detection and margin assessment is discussed.

The manuscript ends with a conclusion summarizing the achieved work and offering future work perspectives. Hardware and software further developments of the imaging platform are discussed. Future milestones for this device's clinical translation are also outlined. Finally, continuation of the fluorescence quantification study is considered.

**References**


[1] Zaffino P., Moccia S., De Momi E., Spadea M.F., ''A Review on Advances in Intra-operative Imaging for Surgery and Therapy: Imagining the Operating Room of the Future'', Annals of Biomedical Engineering, 48, pp. 2171–2191, (2020)

[2] Alam I.S., Steinberg I., Vermesh O., van den Berg N.S., Rosenthal E.L., van Dam G.M., Ntziachristos V., Gambhir S.S., Hernot S., Rogalla S., ''Emerging Intraoperative Imaging Modalities to Improve Surgical Precision'', Molecular Imaging and Biology, 20(5), pp. 705-715, (2018)

[3] Keereweer S., Van Driel P.B., Snoeks T.J., Kerrebijn J.D., Baatenburg de Jong R.J., Vahrmeijer A.L., Sterenborg H.J., Löwik C.W., ''Optical image-guided cancer surgery: challenges and limitations'', Clinical Cancer Research. 19(14), pp. 3745-3754, (2013)

[4] Applegate M.B., Istfan R.E., Spink S., Tank A., Roblyer D., ''Recent advances in high speed diffuse optical imaging in biomedicine'', APL Photonics, 5, 040802, (2020)

[5] Cuccia D.J., Bevilacqua F., Durkin A.J., Ayers F.R., Tromberg B.J., "Quantitation and mapping of tissue optical properties using modulated imaging", Journal of Biomedical Optics, 14(2), 024012, (2009)

[6] Gioux S., Mazhar A., Lee B.T., Lin S.J., Tobias A.M., Cuccia D.J., Stockdale A., Oketokoun R., Ashitate Y., Kelly E., Weinmann M., Durr N.J., Moffitt L.A., Durkin A.J., Tromberg B.J., Frangioni J.V., "First-in-human pilot study of a spatial frequency domain oxygenation imaging system", Journal of Biomedical Optics, 16(8), 086015, (2011)

[7] Vervandier J., Gioux S., "Single snapshot imaging of optical properties", Biomedical Optics Express, 4, pp. 2938-2944, (2013)

[8] Aguénounon E., Dadouche D., Uhring W., Gioux S., "Single snapshot of optical properties image quality improvement using anisotropic 2D windows filtering", Journal of Biomedical Optics, 24(7), 071611, (2019)

[9] Aguénounon E., Smith J.T., Al-Taher M., Diana M., Intes X., Sylvain Gioux S., "Real-time, wide-field and high-quality single snapshot imaging of optical properties with profile correction using deep learning", Biomedical Optics Express, 11(10), pp. 5701-5716, (2020)

# I. Medical imaging for surgery

Even though the contribution brought with this doctoral work is bound to the intraoperative environment, imaging impacts all phases of a patient's journey through surgery. This chapter is designed to give an overview of the use of medical imaging throughout the perioperative period.

## I.1. The need for imaging in the surgical workflow

Operating rooms have been equipped with more and more technology-advanced devices over the past few years. However, surgeons still mostly rely on their touch and vision senses together with their experience to navigate the surgical field. More precisely, their ability to distinguish healthy from diseased tissues is based on subjective inputs. Tissue status assessment is of utmost importance in oncologic surgery, both for tumor resection and reconstruction procedures. Yet, it remains an unmet clinical need. The subjectivity impacting the decision-making is consequently leading to high failure rates and healthcare costs. For this reason, computer-assisted surgery is widely employed throughout the perioperative period to improve the care provided to the patient. A large set of imaging techniques is implemented in each of the perioperative phases.

Starting from the preoperative phase, image-guidance impacts the diagnosis, planning and surgical simulation phases of the patient's journey. A number of scanning techniques enable the virtual reconstruction of the patient's anatomy. The reconstructed region can be manipulated and compared to the normal and pathological anatomy to establish an appropriate diagnosis and surgical plan. Moreover, the surgeons can take advantage of this virtual environment to simulate the procedure on the reconstructed model and assess the defined planning.

During the intraoperative phase, imaging devices producing real-time feedback offer greater control over the procedures [1,2]. Both surgical field navigation and decision-making can benefit from providing additional information. Indeed, the outcome of structural imaging can be confronted to the preoperative data as the surgical plan is completed. Moreover, functional imaging enables the status monitoring of tissues and organs of interest. Altogether, surgeons gain access to objective information, leading to minimized trauma and risk for complications but also increased success rates.

Image-guided surgery also paved the way for minimally invasive procedures. In this approach, interventional instruments and imaging devices are directed inside the patient body through small incisions, as opposed to open surgery where a large incision is made, and the surgical field is exposed to the air. By essence, minimally invasive surgery reduces the incidence of complications and speeds the recovery, thus

improving surgical outcomes, reducing the hospitalization time and healthcare cost [3]. This paradigm shift impacts more and more fields in surgery as it greatly enhances the health outcome and benefits to the patient's safety and comfort.

This always improving patient-centered care is also profitable to the entire healthcare system as the health outcome tends to consistently improve across practitioners and hospitals. However, this cutting-edge technology represents a considerable investment for hospitals in terms of equipment acquisition and staff training. Additionally, the presence of new devices in already crowed operating rooms create the need for new hybrid rooms, adapted to the specific requirements of the implemented technologies.

## I.2. Conventional imaging techniques

A wide range of imaging techniques are currently standard-of-care, each of them meeting specific clinical needs all along the surgical process. This section gives a quick overview of the different forms of imaging employed for surgical act guidance.

### I.2.1. X-ray imaging and computed tomography

Radiography has been used for diagnostic purposes for over a century now. Indeed, the ability of X-rays to greatly penetrate biological tissues makes it an ideal candidate to probe the internal structures of the human body. A very simple setup consisting of an X-ray generator and a photographic film enable the imaging of a large portion of the body. In this configuration, the X-ray beam is directed towards the region of interest and penetrates the biological tissues. Depending on the local composition and density, the primary beam is attenuated through two main processes: photoelectric absorption and Compton scattering. The remaining rays – commonly called the remnant beam – finally expose the photographic film, accordingly to the attenuation occurring along the path of each ray. This method commonly referred to as projectional radiography produces a two-dimensional (2D) static scan of a region limited to the size of the photographic film [4].

Given the X-rays higher absorption by calcium and lower absorption by carbon, the images yield good contrast between respectively hard and soft tissues. In order to reveal structures of interest such as blood vessels, a contrast agent can be employed such as iodine and barium. Iodine is commonly used for circulatory system investigation after intravenous investigation, while barium is used for enhancing contrast in the digestive system after administration by swallowing or by enema. Though this technique enables the investigation of internal structures, it is limited to two-dimensional still images.

By replacing the photographic film with a fluorescent screen converting the X-ray radiations into visible light, radiographers and radiologists were able to directly view the resulting images. This method named fluoroscopy thus enables motion capture, which is a considerable improvement. Later developments include X-ray image intensifiers to enhance the image brightness and the addition of a digital camera to display the images on a remote screen. Finally, flat-panel detectors were implemented [5]. Similarly to digital photography and video, these sensors convert the X-ray radiations into an electrical signal, producing images for remote display, storing and even processing [6]. This allows visualization in real-time with lower radiation doses increasing the safety of both operators and patients [7].

Additionally, its implementation in a compact form makes fluoroscopy suitable for interventional imaging such as angiography or venography, but also to assist biopsy procedures. Such imaging devices are usually built in a C-shape and are mounted on an articulated arm so they can be moved around the patient and oriented optimally. For this reason, they are commonly referred to as C-arm systems. Many fluoroscopy imaging systems are nowadays commercially available, to name a few: Allura Xper FD10 By Philips, Innova™ IGS 540 by GE Healthcare and Alphenix Core+ by Canon. Illustrations of such devices is shown in **Figure I.1**.

**Figure I.1– A typical C-arm fluoroscopy device. (Allura Xper FD10 By Philips) [8]**

Despite the flexibility offered by the mobility of C-arm fluoroscopy systems, this imaging method is by essence limited to a two-dimensional scanning of the body. Computed tomography (CT) offers instead cross-sectional images of the body. After rotating the X-ray generator and detector pair and recording the attenuation from different angles, a reconstruction algorithm is applied to produce tomographic images of a region [9]. When paired to the rotation, translation enables three-dimensional (3D) full-body scanning of the patient within minutes. Consequently, multi-plane reconstructions and volume visualization are made possible, representing a considerable advantage over 2D imaging. Slices can be analyzed down to the sub-millimeter scale thickness [10]. Additional processing including segmentation enable structures extraction such as blood vessels.

Overall, its versatility for trauma and disease diagnosis, intervention planning and treatment monitoring made CT scan a routine medical examination. Over 80 million scans a year are performed in the United States alone [11]. A variety of options are available on the market such as the following products: Aquilion LB by Canon, IQon by Philips and Revolution Frontier by GE Healthcare. A typical CT scanner setup is shown in **Figure I.2**.

**Figure I.2 – A full-body CT scanner device. (Aquilion LB by Canon) [12]**

Even though CT scanners imaging capabilities surpass fluoroscopy and conventional radiography, its larger footprint and slower scanning process make it less versatile for interventional imaging. Additionally, the radiation dose received by the patient during a CT scan significantly increases compared to simpler 2D imaging techniques. Due to the ionizing nature of X-ray, excessive exposition to such radiations can damage biological tissues at the cellular level [13]. An estimation of nearly 30,000 new radiation-induced cancer cases due to CT scans was established for scans performed in the United States in 2007 alone [14]. Larger footprint and higher cost compared to fluoroscopy are additional drawback to be considered, as they represent an important investment.

### I.2.2. Magnetic resonance imaging

Just like X-ray radiations, nuclear magnetic resonance (NMR) can be exploited to produce internal images of the human body. NMR spectroscopy consists in observing the local magnetic field around atomic nuclei, to further determine their environment and investigate intramolecular structures. In particular, proton nuclear magnetic resonance focuses on the hydrogen nuclei within molecules which are present in most

organic compounds, especially water ($H_2O$) and fat tissues [15]. A magnetic resonance imaging (MRI) device is composed of a strong electromagnet and a set of radiofrequency transmitter and receiver coils. The electromagnet produces a very intense static and homogenous magnetic field – typical between 1 and 3 Tesla (T). When placed in this static magnetic field, the nuclei spin polarization will align with the field. Additionally, the nuclei are able to absorb radiofrequency waves at resonant frequencies depending on the intensity of the static magnetic field. In turn, the transmitter coils are tuned to the resonance frequency of protons specifically. This absorption process leads to a change in the polarization state of the proton, followed by a relaxation mechanism. The receiver coils capture the resultant signal to be analyzed.

Due to the high penetration depth of radiofrequency waves in biological tissues, MRI can produce full-body images by scanning the patient. By combining a particular setting of pulses and field gradients, MRI sequences are built and produce images with specific contrast. Among the wide array of MRI sequences, most common are T1-weighted, T2-weighted and proton density-weighted [16]. T1-weighted images highlight for instance fat tissues and paramagnetic contrast agents such as gadolinium-based complexes. T2-weigthed images rather highlight higher water content as in tumor tissues or inflammation and infection sites. Proton density-weighted images produce better contrast between gray and white matter. These multiple outcomes enable tissue and structure identification in three dimensions with slightly poorer resolution than a CT scan but considerably enhanced contrast in soft tissues [17]. In addition to enabling tissue identification, MRI can detect neural activation making it particularly adapted for brain imaging. Using a dedicated sequence named blood-oxygen-level dependent (BOLD) contrast, brain activity associated with blood flow could be measured, yielding functional MRI (fMRI) [18]. **Figure I.3** displays examples of reconstructed slices from different MRI sequences exhibiting the different purposes of each contrast image [19].

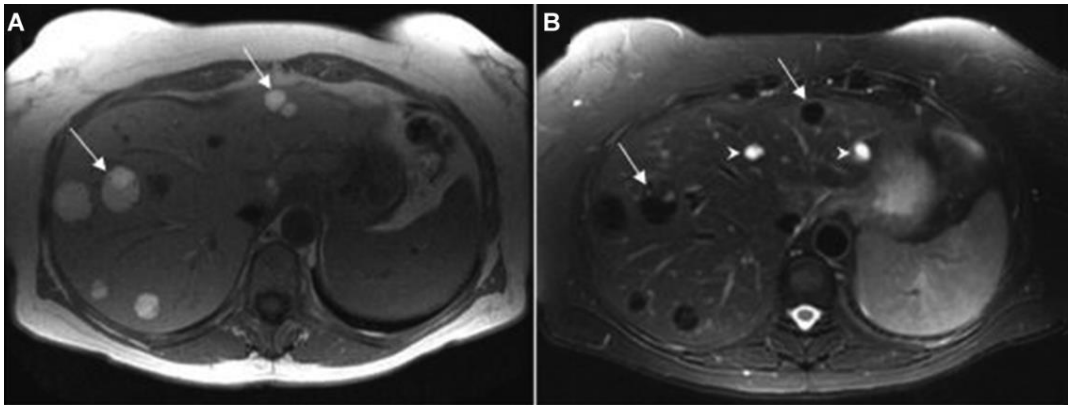


**Figure I.3 – MRI multiple outputs comparison of hepatic metastatic melanoma. The lesions appear bright in the T1-weighted image (left) and dark in the T2-weighted image (right) [19].**

Overall, MRI provides high resolution and high contrast 3D images of the human body without using ionizing radiations. In appearance, MRI scanners resemble CT scanners, as depicted in **Figure I.4**. Many commercial

systems are available, such as the SIGNA™ Explorer by GE Healthcare, the Vantage Orian 1.5T by Canon and the OPENMARK 4000 by Anke.


**Figure I.4 – A typical full-body MRI scanner. (SIGNA™ Explorer by GE Healthcare) [20]**

Inherently to the use of very strong magnetic fields, MRI prohibits the presence of magnetizable objects near the scanner. Also, patients with implants such as pacemakers and stimulators or implants containing iron cannot undergo an MRI examination. The intraoperative use of MRI thus requires adaptation of the whole surgical workflow and equipment. Additionally, the sequences acquisition is a time-consuming process – typical duration is around 1 hour – and is very sensitive to motion artifacts. Overall, these are detrimental to the patient discomfort in comparison to less constraining methods.

### I.2.3. Ultrasound imaging

Mechanical waves also propagate in the body and can alternatively be used to image internal structures of the body. Soundwaves in the megahertz (MHz) range are typically employed, trading-off penetration depth and resolution. An ultrasonography probe is composed of piezoelectric transducers, emitting soundwaves that propagate inside the biological tissues at an average velocity of 1540 m/s. At the interface of two different tissues, a fraction of the wave is reflected back towards the probe, while the rest of the incident wave continues to propagate. This phenomenon stems from the acoustic impedance mismatch between two materials. The impedance is defined as the product of material density and soundwave velocity and is characteristic of each type of biological tissue [21]. Thus, the signal recorded by the receiving transducers in the probe contain depth information about the structure below the probe. More precisely, by analyzing

the intensity and time-of-flight (ToF) of the echo waves, the distances between different tissues interfaces along the propagation axis are extracted.

Several imaging modes exist [22]. The A-mode or amplitude mode produces a line scan using a single transducer. The B-mode or brightness mode consists in scanning a line of transducers to create a 2D cross-section image. By extension, an array of transducers enables a 3D reconstruction. Alternatively, by gating the A-mode signal and scanning a region of interest, a normal plane to a B-mode image can be imaged. This way, bi-plane image can be achieved. As A-mode and B-mode signals can be obtained very quickly, video-rate imaging can be provided. The M-mode or motion mode allows video capturing. In addition to imaging anatomical structures, flowing blood can be visualized by adapting the B-mode. Indeed, through the Doppler shift induced in the soundwave by the reflectors motion speed, blood flow can be monitored. Alternatively, in the B-flow mode moving reflectors like red blood cells are highlighted by suppressing stationary components [23].

Ultrasonography produces in-depth imaging for direct viewing of internal structures of the body. As this imaging modality is not based on ionizing radiation, or on the use of strong magnetic fields, its integration in the surgical workflow is straightforward. Moreover, given the simplicity of an ultrasonography setup, very compact and portable system can be implemented. Hence, ultrasound imaging is employed as a routine examination tool, for diagnostic or intraoperative use, but also in a point-of-care setting. It is particularly adapted for assisting procedures such as biopsies and injections. By miniaturizing the probe, major organs of the abdomen can be examined non-invasively in a transesophageal or endorectal fashion. Highly portable and user-friendly systems are widely available on the market, including MyLab$^{TM}$X8 Platform by Esaote, Aplio a by Canon and T-lite by Sonoscanner. Typical imaging devices are depicted in **Figure I.5**.


**Figure I.5 – Two ultrasound imaging devices. An imaging platform (*left:* Aplio α by Canon) and a handheld device (*right:* T-lite by Sonoscanner) [24,25]**

Despite its flexibility and compactness, ultrasound imaging presents drawbacks, especially for intraoperative use. Indeed, given the acoustic mismatch between air and soft tissues such as skin, the probe needs to be placed in contact with the patient, in addition to using a water-based gel as a coupling medium to optimize impedance matching. Acoustic waves also show poor penetration in bone tissue or tissue-gas interfaces, making it challenging to image organs such as brain or pancreas. Moreover, contrast between soft tissues is moderate due to very similar impedances across tissues. Finally, this imaging modality requires training and skill to obtain high-quality images. This outcome is thus operator-dependent, impacting the patient's outcome [26].

### I.2.4. Nuclear medicine imaging

Contrary to the previously described tomography techniques, nuclear medicine does not recover the anatomical structures within the body but reveals the spatial distribution of specific tracers instead. This imaging modality is based on radioactive tracers. Radioactive isotopes are unstable nuclide with excessive energy. When undergoing radioactive decay, the energy excess can be emitted from the nucleus as ionizing radiations, including gamma-rays and positrons. Some radionuclides can be incorporated to ligands designed to bind specifically to receptor systems in the body, while others are simply included in physiological activities [27]. This way, specific tissues of interest can be highlighted, or functional imaging can be achieved. Two main imaging methods exist, depending on the type of radioactive decay. Single-photon emission computed tomography (SPECT) consists in directly imaging gamma-rays emitted by the nuclide [28]. Alternatively, positron emission tomography (PET) employs positron-emitting radiotracers instead. The emitted particle travels in the tissue – typically as far as 1 millimeter – until annihilating with an electron, producing a pair of gamma photons travelling in opposite directions [29]. Consequently, both techniques are based on gamma radiations imaging. Like fluoroscopy, scintigraphy takes advantage of luminescence induced by gamma-rays in specific materials. Digital sensors are built combining these scintillators with photomultipliers or avalanche photodiodes and are commonly referred to as gamma cameras [30].

SPECT imaging consists in recording 2D projections of the region of interest. A complete 3D scan can be achieved using a setup with multiple cameras, reducing the acquisition time to around 15 minutes. PET imaging slightly differs as facing sensors and additional gating devices are employed. Both methods are complementary with CT and MRI techniques, making it possible to merge functional imaging with anatomical imaging. Overall, this yields full body scanning for applications including bone structures assessment, brain perfusion imaging or tumor screening and staging. Commercially available options offer

different combinations of these imaging technologies. For instance, AnyScan by Mediso is a hybrid SPECT / PET / CT scanner. This imaging device is shown as an example in **Figure I.6**.


**Figure I.6 – A hybrid SPECT / PET / CT scanner. (AnyScan by Mediso) [31]**

Yet, SPECT and PET intrinsically represent increased hazards for the patients and operators as both radioactive materials and ionizing radiations are involved. Additionally, the typically low signal-to-noise ratio (SNR) and the spatial resolution limited to a few millimeters. The benefit-risk balance is therefore more prone to be unfavorable in comparison to other methods using ionizing radiations.

### I.2.5. Optical imaging

Optical imaging is dedicated to enhancing the sight capabilities of surgeons. The human eye is naturally sensitive to the so-called ''visible'' range (400 – 700 nm) of the electromagnetic spectrum. The detection of light by our eyes grants us sight, enabling the viewing of shapes and colors. In turn, surgeons can visually assess the surgical field. Optical imaging encompasses techniques exploiting light-matter interactions across the ultraviolet, visible, and infrared wavelength ranges, typically between 200 nm and 2000 nm. Reflection and transmission, but also absorption and scattering are commonly observed phenomena within biological tissues, yielding information about biological tissues and physiological activities. This way, tissues can be probed up to several millimeters deep [32]. More theoretical descriptions of light-tissue interactions and biological tissue optical characterization are given in Chapter II. Optical imaging is not only offering a way to extend the eyes detection capabilities to larger wavelength ranges, but also investigating tissues at different scales: macroscopic and microscopic.

In contrast to the previously presented imaging modalities, optical imaging features the use of non-ionizing radiations, high resolution and sensitivity, high portability and represents a moderate investment as the involved technologies are often cost-efficient. This section focuses on clinically approved systems, representing the standard of care currently in use in clinics. Further state-of-the-art imaging techniques are detailed in Chapter III.

White light imaging is the simplest form of optical imaging, where a camera is used to capture visible light from a scene, as human eyes would do. This way, the anatomical view of the surgical field can be recorded and compared to the outcome of concurrent imaging techniques. This also provides guidance during minimally invasive procedures, where the surgical field in accessed through either natural orifices or small ports. In this configuration, a camera system is inserted along with the surgical tools and provides direct guidance. White light imaging is also used in situations where delicate tasks at a small scale need to be performed, as it can offer significant zoom.

While white light imaging is based on capturing separately red, green and blue light, multispectral imaging (MSI) consists in imaging several wavelength bands – typically up to a dozen – including outside of the visible range. The selection of these spectral bands is based on the optical behavior of molecular compounds of interest within the tissues. This way, narrow-band imaging (NBI) has been used for highlighting the presence of hemoglobin, revealing vasculature. This way, the use of NBI for gastric cancer diagnosis was demonstrated [33]. Olympus released the EVIS EXERA III, an imaging platform featuring white light imaging and NBI for endoscopy – shown in **Figure I.7**. Blood perfusion can also be assessed by thermography using longer infrared wavelengths – typically around 10 micrometers. Increasing the spectral resolution improves the capacity to distinguish different chromophores. Hyperspectral imaging (HSI) further increases the number of observed spectral bands up to several hundreds.

**Figure I.7 – A multispectral narrow-band imaging column. (EVIS EXERA III by Olympus) [34]**

Fluorescence imaging is based on the detection of endogenous or exogenous fluorophores to highlight anatomical structures and targeted receptor systems or exhibit physiological activities. When excited with incident light, these compounds emit part of the absorbed light at a slightly longer wavelength by fluorescence. Using appropriate filters, the fluorescence emission can be detected, thus revealing the location of the fluorophores. Such dedicated imaging systems are typical multispectral imaging devices featuring visible light detection for anatomical imaging and adapted filtering and detection windows according to the employed fluorophores. Given the typical optical properties of biological tissues, light attenuation is lower in the near-infrared range. Consequently, excitation and emission photons benefit from higher penetration depth. For this purpose, NIR fluorescence is preferred and the markets for both contrast agents and imaging systems is growing. This way, fluorescence imaging represents a great asset for surgical field navigation but also tumor margin delineation and resection assistance for various types of tumors [35]. Both open-air and endoscopic implementations of fluorescence imaging devices are currently deployed for clinical use. Typical examples include the Quest Spectrum® by Quest medical imaging and the VITOM® ICG by Karl Storz. Illustrations are shown in **Figure I.8**.


**Figure I.8 – An interventional fluorescence imaging device; including its endoscopic implementation (Quest Spectrum® by Quest medical imaging) [36]**

In order to analyze the tissues at the microscopic scale and further assess their viability, biopsies are performed to collect tissue samples. These are examined under a microscope to produce a histopathological analysis, leading to a medical diagnosis. This process is very time-consuming, and the screening is limited to the number of biopsies taken. For this purpose, confocal microscopy has been incorporated into endoscopes to enable the non-destructive, live tissue examination at the micrometer scale [37]. Endomicroscopy thus grants surgeons access to histology images intraoperatively. Since confocal microscopy offers optical sectioning, in-depth images and 3D reconstructions of tissues are made possible. Cellvizio by Mauna Kea and Convivo by Zeiss are two commercially available platforms. An illustration is shown in **Figure I.9**. Additional imaging technologies are being implemented in this framework such as optical coherence tomography (OCT), already widely used for retinal imaging or coronary artery imaging [38,39,40].


**Figure I.9 – An endomicroscopy platform. (Convivo by Zeiss) [41]**

## I.2.6. Augmented reality

Medical imaging is dedicated to enhancing the surgeon's perception by revealing hidden features, highlighting physiological activities and providing parameters measurements. The imaging outcome is usually displayed on remote screens distributed over the operating room, or supported by ceiling-mounted arms for more flexibility. However, this configuration leads to surgeons looking back-and-forth at the screen and the surgical field. In turn, hand-eye coordination is challenging, and inaccurate assessment of the images might lead to errors or even damage when acting on the surgical field. By merging the surgeon's view with the preoperative or intraoperative imaging outcome in real-time, augmented reality (AR) directly

increases the visual perception, thus improving comfort. This technology is based on wearable heads-up display devices like headsets or glasses [42]. Additional processing including features recognition, hands and surgical tools tracking further increases the capabilities of AR and enables interaction with the 3D displayed dynamic images. Commercial systems are more and more available, such as the HoloLens2 by Microsoft, the Xvision by Augmedics or the PARADIGM$^{TM}$ by Proprio Vision. An illustration of these devices is shown in **Figure I.10**.

**Figure I.10 – Augmented-reality assisting a surgical procedure using a headset device (Hololens2 by Microsoft) [43]**

## I.3. Summary

The previous section gave an overview of conventional medical imaging techniques in the context of image-guided surgery. A comparison of these imaging modalities is established in **Table I.1**. The selected criteria are based on the clinical environment and inherent requirements. Medical imaging is designed to improve the patients' outcome throughout their journey. Yet, each phase of surgery sets different requirements in terms of imaging and implementation. For instance, tomography methods such as X-ray, CT, MRI and nuclear imaging are mostly used for preoperative and postoperative purposes. To overcome the limitations of each modality alone, their complementarity is exploited to create hybrid devices. However, the large footprints, higher cost and large number of safety measures to be implemented when using these systems make their intraoperative use challenging. Indeed, adapted facilities and surgical workflow are required,

along with specific staff training. NIR optical imaging seems to be best suited for intraoperative use. It features structural and functional imaging, real-time capabilities, portability, cost efficiency, minimal interference with the surgical workflow. The use of NIR optical imaging for intraoperative guidance is discussed in Chapter III.

| Features | X-ray | Computed tomography | Magnetic resonance | Ultrasound | Nuclear | Optical |
|---|---|---|---|---|---|---|
| Spatial resolution | ●●● | ●●● | ●● | ●● | ● | Variable |
| Penetration depth | ●●● | ●●● | ●●● | ●● | ●●● | ● |
| Structural parameters | ✓ | ✓ | ✓ | ✓ | ✗ | ✓ |
| Functional parameters | ✗ | ✗ | ✓ | ✓ | ✓ | ✓ |
| Non-ionizing radiations | ✗ | ✗ | ✓ | ✓ | ✗ | ✓ |
| Real-time capability | ✓ | ✗ | ✗ | ✓ | ✗ | ✓ |
| Portability | ✗ | ✗ | ✗ | ✓ | ✗ | ✓ |
| Cost | ●● | ●● | ●●● | ● | ●● | ● |

**Table I.1 – Medical imaging modalities comparison for image-guided surgery**

According to these considerations, the objective of this thesis project is the development of a novel multimodal imaging platform, capable of performing widefield quantitative oxygenation and fluorescence imaging in real-time, as part of the surgical workflow. Using diffuse optical imaging to measure tissues optical properties, oxygenation rate mapping can be achieved and used as an input for blood perfusion assessment. Furthermore, the multimodal feature of the platform enables fluorescence imaging, making possible the direct comparison with oxygenation imaging. This same device offers the possibility to combine diffuse optical imaging with conventional fluorescence imaging, yielding widefield quantitative imaging. The increased objectivity granted by the quantitative feature aims at making more reliable the use of fluorescence imaging, especially during tumor resection procedures. More detailed objectives are presented in Chapter IV.

The next chapter introduces the basics of NIR optical imaging. Tissue-light interaction and the modeling of light propagation are first covered. Second, methods for tissue optical characterization are presented.

**References**


[1] Schwaiger J., Markert M., Shevchenko N., Lueth T.C., ''The effects of real-time image navigation in operative liver surgery'', International Journal of Computer Assisted Radiology and Surgery, 6(6), pp. 785-796, (2011)

[2] Sarode S.C., Sarode G.S., ''Real-time fluorescence imaging for cancer surgery: a pathologist's perspective'', The Lancet Oncology, 22(7), e282, (2021)

[3] Darzi S.A., Munz Y., ''The impact of minimally invasive surgical techniques'', Annual Review of Medicine, 55, pp. 223-37, (2004)

[4] Ou X., Chen X., Xu X., Xie L., Chen X., Hong Z., Bai H., Liu X., Chen Q., Li L., Yang H., ''Recent development in X-Ray imaging technology: future and challenges'', Research, 2021, 9892152, (2021)

[5] Nickoloff, E.L.,''AAPM/RSNA Physics Tutorial for Residents: Physics of Flat-Panel Fluoroscopy Systems''. RadioGraphics, 31 (2), pp. 591–602, (2011)

[6] Lança L., Silva A, ''Digital Imaging Systems for Plain Radiography'', Springer, pp. 9-20, (2012)

[7] Balter S., Hopewell J.W., Miller D L., Wagner L.K., Zelefsky M.J., "Fluoroscopically Guided Interventional Procedures: A Review of Radiation Effects on Patients' Skin and Hair", Radiology, 254 (2), pp. 326–341, (2010)

[8] https://www.philips.fr/healthcare/product/HC722022CA/systeme-de-radiologie-cardio-vasculaire-allura-xper-fd10 (Accessed 15.02.2022)

[9] Shi L., Liu B., Yu H., Wei C., Wei L., Zeng L., Wang G, ''Review of CT image reconstruction open source toolkits'', Journal of X-ray Science and Technology, 28(4), pp. 619-639, (2020)

[10] Ginat D.T., Gupta R., ''Advances in Computed Tomography Imaging Technology'', Annual Review of Biomedical Engineering, 16(1), pp. 431-453, (2014)

[11] Brenner D.J., ''Slowing the increase in the population dose resulting from CT scans'', Radiation Research, 174(6b), pp. 809–815, (2010)

[12] https://fr.medical.canon/product-solutions/computed-tomography/aquilion-lb/ (accessed 15.02.2022)

[13] Brenner D.J., Hall E.J., "Computed tomography – an increasing source of radiation exposure", The New England Journal of Medicine, 357(22), pp. 2277–84, (2007)

[14] Berrington de González A., Mahesh M., Kim K.P., Bhargavan M., Lewis R., Mettler F., Land C., "Projected cancer risks from computed tomographic scans performed in the United States in 2007", Archives of Internal Medicine, 169(22), pp. 2071–7, (2009)

[15] Roth C., Deshmukh S., ''Fundamentals of body MRI, 2nd edition'', Elsevier, 2016.

[16] Gaillard F., Murphy A., ''MRI sequences (overview)'', Reference article, Radiopaedia.org https://doi.org/10.53347/rID-37346 (reviewed 2020, accessed 15.02.2022)

[17] Chang A. E., Matory Y. L., Dwyer A. J., Hill S. C., Girton M. E., Steinberg S. M., Knop R. H., Frank J. A., Hyams D., Doppman J. L., ''Magnetic resonance imaging versus computed tomography in the evaluation of soft tissue tumors of the extremities'', Annals of surgery, 205(4), pp. 340–348, (1987)

[18] Singleton M.J., ''Functional Magnetic Resonance Imaging'', Yale Journal of Biology and Medicine, 82(4), pp. 233, (2009)

[19] Vu L.N., Morelli J.N., Szklaruk J., ''Basic MRI for the liver oncologists and surgeons'', Journal of Hepatocellular Carcinoma, 5, pp. 37-50, (2018)

[20] https://www.gehealthcare.com/products/magnetic-resonance-imaging/1-5t/signa-explorer (accessed 15.02.2022)

[21] Tole N.M., Ostensen H., ‘’Basic physics of ultrasound imaging’’, World Health Organisation, pp. 24, (2005)

[22] Cobbold R.S.C., ‘’Foundations of Biomedical Ultrasound’’, Oxford University Press, pp. 422–423, (2007)

[23] Wachsberg R.H., "B-Flow Imaging of the Hepatic Vasculature: Correlation with Color Doppler Sonography", American Journal of Roentgenology, 188(6), pp. 522-533, (2007)

[24] https://fr.medical.canon/product-solutions/product-solutionsdiagnostic-ultrasound/aplio-a-series/aplio-a/ (accessed 15.02.2022)

[25] https://www.sonoscanner.com/nos-produits/t-lite/ (accessed 15.02.2022)

[26] Beggs A.D., Thomas P.R.S., ''Point of use ultrasound by general surgeons: Review of the literature and suggestions for future practice'', International Journal of Surgery, 11(1), pp. 12-17, (2013)

[27] Wadsak W., Mitterhauser M., "Basics and principles of radiopharmaceuticals for PET/CT", European Journal of Radiology, 73(3), pp. 461–469, (2010)

[28] Livieratos, L., ‘’Chapter 12 – Basic principles of SPECT and PET imaging’’, in Radionuclide and Hybrid Bone Imaging, edited by Fogelman I., Gnanasegaran G., van der Wall H., Springer, pp.345-359, (2012)

[29] Bailey D.L., Karp J.S., Surti S., ‘’Physics and Intrumentation in PET’’, in Positron Emission Tomography: Basic Sciences, edited by Bailey D.L., Townsend D.W., Valk P.E., Valk, Maisey M.N., Springer, pp. 13-39, (2005)

[30] Khalil M.M., ‘’Basic sciences of nuclear medicine’’, Springer, pp. 231-257, (2010)

[31] https://mediso.com/global/en/product/anyscanr-family/anyscanr (accessed 15.02.2022)

[32] Pirovano G., Roberts S., Kossatz S., Reiner T., ''Optical Imaging Modalities: Principles and Applications in Preclinical Research and Clinical Settings'', Journal of Nuclear Medicine, 61(10), pp. 1419-1427, (2020)

[33] Kurumi H., Nonaka K., Ikebuchi Y., Yoshida A., Kawaguchi K., Yashima K., Isomoto H., ‘’Fundamentals, Diagnostic Capabilities and Perspective of Narrow Band Imaging for Early Gastric Cancer’’, Journal of Clinical Medicine, 10(13), pp. 2918, (2021)

[34] https://www.olympus-europa.com/medical/en/Products-and-Solutions/Products/Product/EVIS-EXERA-III-Endoscopy-System-GI.html (accessed 15.02.2022]

[35] Hoffman R., Bouvet M., ‘’Strategies for Curative Fluorescence-Guided Surgery of Cancer, 1st Edition’’, Elsevier, (2020)

[36] https://www.quest-mi.com/products.html (accessed 15.02.2022]

[37] Goetz M., Malek N., Kiesslich R., ''Microscopic imaging in endoscopy: endomicroscopy and endocytoscopy'', Nature Reviews Gastroenterology & Hepatology, 11, pp. 11–18, (2014)

[38] Carrasco-Zevallos O. M., Viehland C., Keller B., Draelos M., Kuo A. N., Toth C. A., Izatt J. A., ''Review of intraoperative optical coherence tomography: technology and applications'', Biomedical optics express, 8(3), pp. 1607–1637, (2017)

[39] Muijzer M.B., Schellekens P.A., Beckers H.J.M., de Boer J.H., Imhof S.M., Wisse R.P.L., ''Clinical applications for intraoperative optical coherence tomography: a systematic review'', Eye, 36, pp. 379–391, (2022)

[40] Bezerra H.G., Costa M.A., Guagliumi G., Rollins A. M., Simon D.I., ''Intracoronary optical coherence tomography: a comprehensive review clinical and research applications. JACC. Cardiovascular interventions, 2(11), pp. 1035–1046, (2009)

[41] https://www.zeiss.fr/meditec/wbc/produits/neurochirurgie/endomicroscope-confocal-convivo.html (accessed 15.02.2022)

[42] Eckert M., Volmerg J. S., Friedrich C. M., ''Augmented Reality in Medicine: Systematic and Bibliographic Review'', JMIR mHealth and uHealth, 7(4), e10967, (2019)

[43] https://med.stanford.edu/bmrgroup/Publications/PublicationHighlights/HoloLensSurgicalPlanning.html (accessed 15.02.2022)

# II. Near-infrared optical imaging

This chapter covers the basics of light-matter interaction and different approaches for modeling light propagation in biological tissues. From this standpoint, the main tissue optical characterization methods are detailed. Focus is made on the near infrared wavelength range which is particularly adapted for biological tissue imaging and spectroscopy.

## II.1. Tissue-light interaction

### II.1.1. Refractive index

The refractive index $n$ of a material is characteristic of its interactions with light. It is defined as the ratio of the speed of light in vacuum $c$ and the phase velocity of light $v$ in this material **(EII.1)**. This index is wavelength-dependent. Typically, the refractive index of water in the visible range is 1.33. For biological tissues, it ranges between 1.33 and 1.65 [1].

$$n = \frac{c}{v} \qquad (EII.1)$$

At the interface of two materials, part of the incident light undergoes refraction depending on the refractive index of each medium and on the angle of incidence at the interface. This results in a change in propagation speed and direction of light according to the Snell-Descartes law **(EII.2)**, where $n_1$ and $i_1$ are the incident refractive index and angle of incidence, and $n_2$ and $i_2$ are the refractive medium index and angle of refraction.

$$n_1.\sin(i_1) = n_2.\sin(i_2) \qquad (EII.2)$$

The part of light which is not refracted is reflected within the incidence plane with an angle $i_r = i_1$. This mechanism is commonly referred to as specular reflection. An illustration of the refraction phenomenon is shown in **Figure II.1**. The amount of reflected light depends on the angle of incidence and refractive indices of both media, according to the Fresnel equations. For a normal incidence, the reflectivity $R_0$ is only function of the refractive indices **(EII.3)**.

$$R_0 = \left|\frac{n_1 - n_2}{n_1 + n_2}\right|^2 \qquad (EII.3)$$

A special case of refraction is observed for $n_2 < n_1$. When reaching a critical angle of incidence $i_c$, the refracted angle $i_2$ increases up to 90°. Past that angle given by $\sin(i_c) = {}^{n_2}/_{n_1}$, the light is entirely reflected in the incident medium. This phenomenon is named total internal reflection.

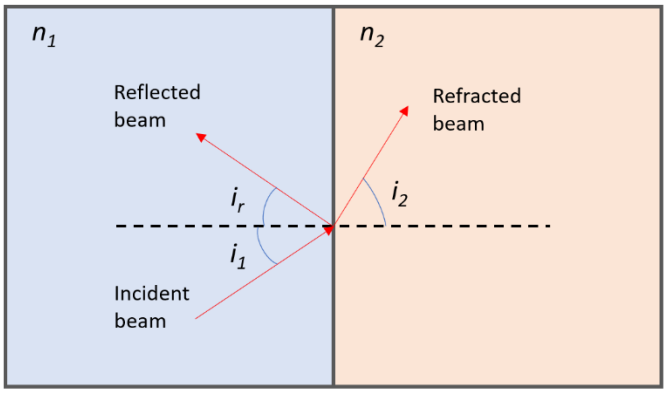


**Figure II.1 – Refraction of light at the interface of two media with $n_1 > n_2$.**

## II.1.2. Absorption

In its complex form, the refractive index $\underline{n}$ is composed of a real part $n$ and an imaginary part $\kappa$. The latter represents the extinction coefficient of the material. Given the electric field $\boldsymbol{E}$ of a plane electromagnetic wave propagating in the $z$-direction, with a pulsation ω and wave number $\underline{k} = 2\pi\underline{n}/\lambda_0$ ($\lambda_0$ being the wavelength in the wave in vacuum) the extinction coefficient introduces an exponential decay of the wave intensity throughout the medium of index $\underline{n}$ **(EII.4)**. This decay is described as absorption of light by the medium at the microscopic scale. Most of the absorbed energy results in vibrations, creating heat [2].

$$\boldsymbol{E}(z,t) = \boldsymbol{E_0}.e^{i(\underline{k}z-\omega t)}$$

$$\boldsymbol{E}(z,t) = \boldsymbol{E_0}.e^{i\left({}^{2\pi(n+i\kappa)z}/_{\lambda_0} - \omega t\right)}$$

$$\boldsymbol{E}(z,t) = e^{{}^{-2\pi\kappa z}/_{\lambda_0}} . \boldsymbol{E_0} . e^{i\left({}^{2\pi nz}/_{\lambda_0} - \omega t\right)} \qquad (EII.4)$$

At the macroscopic level, absorption by the medium is described by its absorption coefficient $\mu_a(\lambda_0)$, often given in $mm^{-1}$ or $cm^{-1}$ and function of the wavelength λ. Considering a beam of light of intensity $I$ travelling through a thin slice of a medium, the lost fraction of intensity $dI$ due to propagating through the thickness $dL$ of the slice is given by **(EII.5)**. An illustration of the beam propagation is shown in **Figure II.2**. The integration of **(EII.5)** along the thickness dimension yields the exponential decay of the total intensity $I_0$ throughout the propagation **(EII.6)**. This relation is known as Beer's law.

$$\frac{dI}{I} = -\mu_a(\lambda_0).dL \qquad (EII.5)$$

$$I = I_0.e^{-\mu_a(\lambda).L} \qquad (EII.6)$$

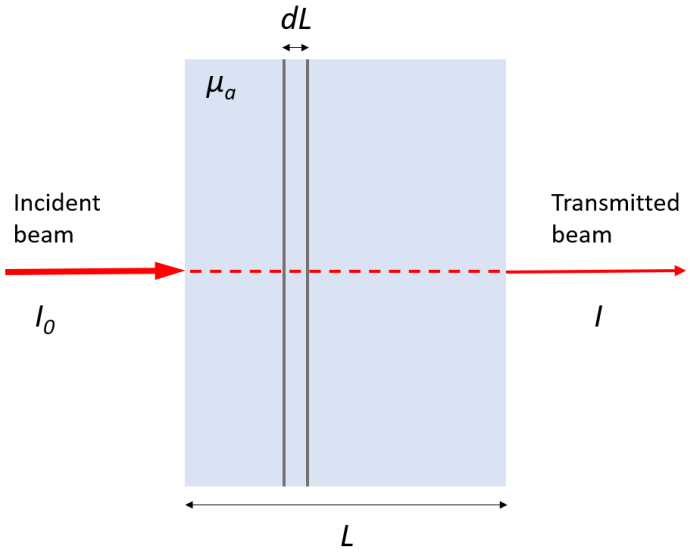


**Figure II.2 – Light propagation through an absorbing medium.**

### II.1.3. Scattering

As described previously, refractive index mismatch leads to refraction of light. Particles of small sizes may be at the origin of index inhomogeneities inside a medium. When the size of the particles is smaller than the incident wavelength, light is scattered by these particles. In turn, photons are deviated from their incident direction of propagation, while conserving their energy. In biological tissues, typical scatterers include cells and cellular components. Depending on the size and shape of the particles, different models are employed to describe the scattering phenomenon. Rayleigh's scattering describes the scattering of light by particles much smaller than the incident wavelength. This phenomenon is isotropic, and its intensity is inversely proportional to the fourth power of the wavelength. Alternatively, for larger particles Mie's scattering can be employed. Mie scattering mostly results in anisotropic forward scattering. Though this model describes scattering of light by round particles only, it is valid regardless of the particle size, thus representing an alternative to Rayleigh scattering when considering larger particles.

At the macroscopic level, scattering is described by its scattering coefficient $\mu_s(\lambda_0)$, typically given in $mm^{-1}$ or $cm^{-1}$. Given a non-absorbing medium of thickness $L$, a total incident light of intensity $I_0$ would result as the output intensity $I$ as described in **(EII.7)**. An illustration of scattering through such a medium is shown in **Figure II.3**.

$$I = I_0 . e^{-\mu_s(\lambda).L} \qquad (EII.7)$$

In the case of anisotropic scattering, the trajectory of a photo is deflected with angle $\vartheta$. The phase function $p(\vartheta)$ describes the angular dependance of the scattering, while the mean value of $cos(\vartheta)$ represents the

preferred direction of scattering. The anisotropy factor $g$ is defined by **(EII.8)**. Thus, forward and backward scattering are described by $g=1$ and $g=-1$, respectively. For isotropic scattering, $g=0$. Typically for soft biological tissue $g$ is considered close to 0.9. The scattering anisotropy directly impact the transmission rate through a medium. Consequently, the so-called reduced scattering coefficient $\mu_s'$ includes the anisotropy factor **(EII.9)**.

$$g = \int_{-1}^{1} p(\cos(\theta)).\cos(\theta).d(\cos(\theta)) \qquad (EII.8)$$

$$\mu_s' = \mu_s.(1-g) \qquad (EII.9)$$

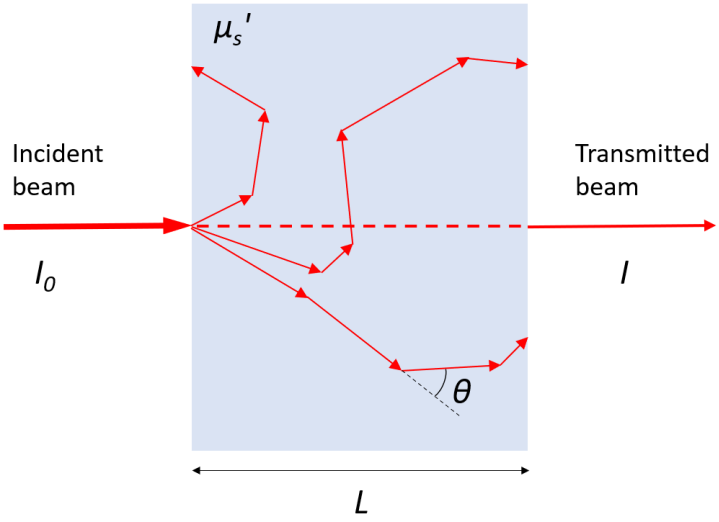


**Figure II.3 – Light propagation through a scattering medium.**

## II.1.4. Fluorescence

Fluorescence describes the conversion of absorbed light by a compound into photons. The absorption of light by a molecule results in the translation of electrons from their energy ground state to excited states of higher energy. When the de-excitation process induces the emission of photons, the emitted light wavelength is shifted towards longer wavelengths in comparison to the excitation light. This phenomenon is commonly referred to as Stokes shift and represents energy losses through non-radiative processes such as vibrational relaxation, internal conversion, or intersystem crossing. The energy transitions and various relaxation processes are illustrated in **Figure II.4**.

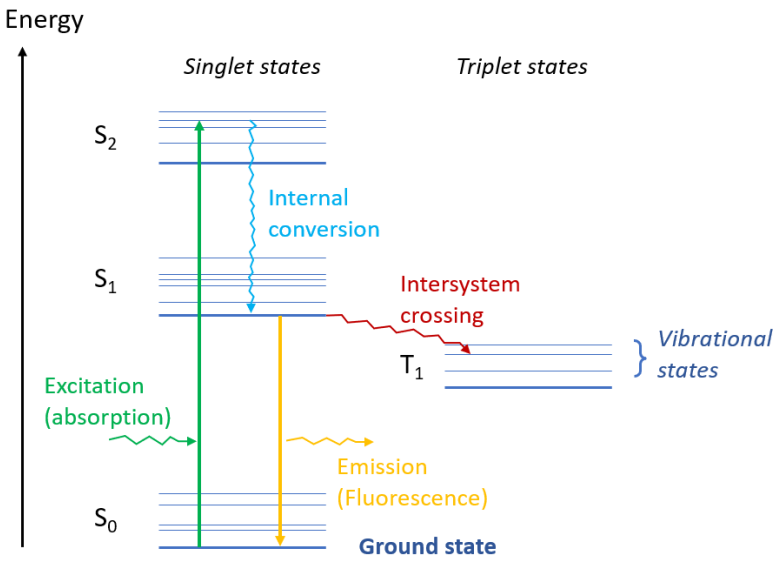


**Figure II.4 – A conceptual Jablonski diagram.**

The quantum yield $\eta$ of a fluorophore measures the photon conversion rate as the ratio of the number of absorbed photons $N_{absorbed}$ and the number of emitted photons $N_{emitted}$ **(EII.10)**. For most fluorophores, $\eta$ is below 10%. If the quantum yield is primarily based on the electronic configuration of the fluorophore, the chemical environment may also affect $\eta$. Indeed, dipole-dipole interaction – or resonance energy transfer – may induce additional non-radiative energy transfers [3].

$$\eta = \frac{N_{emitted}}{N_{absorbed}} \qquad (EII.10)$$

The molecule de-excitation rate leading to fluorescence emission follows an exponential decay, characterized by the radiative decay rate $\tau_{rad}$ and non-radiative decay rate $\tau_{non\text{-}rad}$. The number of molecules in the excited state $N^{S1}{}_0$ at a time $t$ decreases from the initial number of molecules in the excited state $N^{S1}{}_0$ **(EII.11)**. The total rate $\tau$ – referred to as fluorescence lifetime – is also intrinsic to the electronic configuration of the fluorophore, and is also impacted by its environment. For most fluorophores in the visible range, fluorescence lifetime is in the nanosecond scale [4].

$$N^{S1}(t) = N_0^{S1}.e^{-t/\tau} \qquad (EII.11)$$

Fluorescence compounds can be naturally encountered in biological tissues. This endogenous process named autofluorescence enables the imaging of particular biological structures such as the extracellular matrix thanks to the fluorescent properties of collagen and elastin [5]. Alternatively, fluorophores can be synthetized for further use as contrast agent.

## II.2. Modeling of light propagation in tissue

When propagating through biological tissues, light undergoes both absorption and scattering processes. In order to model these concurrent phenomena, analytical and statistical approaches have been established. This section first covers the radiative transfer equation (RTE) and its approximation in the diffusive regime. Second, the so-called Monte Carlo statistical model is described.

### II.2.1. Radiative transfer equation

Standing from a radiometric point of view, light propagation in a medium can be described as a photon flux undergoing absorption and scattering processes. Given a surface element of area $dA$ within a medium, the radiance $L$ represents the power flux $\Phi$ through this area per solid angle $d\Omega$ per unit projected area $dA.cos(\vartheta)$ **(EII.12)**. The radiance $\boldsymbol{L}$ principle is illustrated in **Figure II.5**.

$$\boldsymbol{L} = \frac{\partial^2 \Phi}{\partial \Omega . \partial \mathrm{A} . \cos(\theta)} \qquad (EII.12)$$

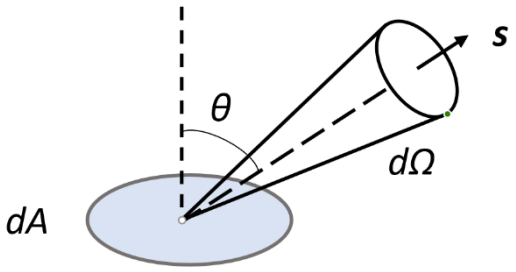


**Figure II.5 – Radiance from a surface *dA* into a solid angle *dΩ*.**

Based on the principle of conservation of energy, the radiative transfer equation describes the gains and losses through the area $dA$ located at a position $\boldsymbol{r}$ over time $t$ **(EII.13)** [6]. It links the radiance from a direction $\boldsymbol{s}$ through a solid angle $d\Omega$ to the radiance from a different direction $\boldsymbol{s'}$ through a solid angle $d\Omega$.

$$\frac{1}{c} . \frac{\partial \boldsymbol{L}(\boldsymbol{r},\boldsymbol{s},t)}{\partial t} = -\boldsymbol{s} . \nabla \boldsymbol{L}(\boldsymbol{r},\boldsymbol{s},t) - [\mu_a(\boldsymbol{r}) + \mu_s(\boldsymbol{r})] . \boldsymbol{L}(\boldsymbol{r},\boldsymbol{s},t) + \mu_s(\boldsymbol{r}) . \int_{4\pi} p(\boldsymbol{s},\boldsymbol{s}') . \boldsymbol{L}(\boldsymbol{r},\boldsymbol{s},t) . d\Omega' + S(\boldsymbol{r},\boldsymbol{s},t) \quad (EII.13)$$

Thus, the temporal variations of radiance represented by the term $\frac{1}{c} . \frac{\partial \boldsymbol{L}(\boldsymbol{r},\boldsymbol{s},t)}{\partial t}$ can be decomposed as the sum of the following terms:

- Divergence losses: $-\boldsymbol{s} . \nabla \boldsymbol{L}(\boldsymbol{r},\boldsymbol{s},t)$
- Absorption and scattering losses: $-[\mu_a(\boldsymbol{r}) + \mu_s(\boldsymbol{r})] . \boldsymbol{L}(\boldsymbol{r},\boldsymbol{s},t)$

- Scattering gains: $\mu_s(\boldsymbol{r}).\int_{4\pi} p(\boldsymbol{s},\boldsymbol{s}').\boldsymbol{L}(\boldsymbol{r},\boldsymbol{s},t).d\Omega'$
- Emission gains: $S(\boldsymbol{r},\boldsymbol{s},t)$

The complexity of this equation requires simplifications to be easily solved. Analytic solutions exist that are valid for simple cases of homogenous media. For more realistic media modeling, numerical methods are employed to derive solutions describing light transport.

### II.2.2. Diffusion approximation

In most biological tissues, scattering is considered to be predominant. Under such circumstances, the RTE can be simplified by admitting approximations. This way, the RTE is reduced to a partial-differential equation which solves for the fluence rate $\Phi$. The diffusion approximation (DA) stems from the following assumptions:

- Scattering is predominant over absorption: $\mu_s(\boldsymbol{r}) \gg \mu_a(\boldsymbol{r})$
- The scattering phase function $p(\boldsymbol{s},\boldsymbol{s'})$ depends on $\vartheta$ alone
- The light source is considered isotropic

Given a light source distribution $S(\boldsymbol{r},t)$, considering a medium of transport coefficient $\mu_{tr} = \mu_a + \mu_s{}'$ the DA equation is given by **(EII.14)** [7].

$$\frac{1}{c}.\frac{\partial\Phi(\boldsymbol{r},t)}{\partial t} - \boldsymbol{\nabla}.\left[\frac{1}{3.\mu_{tr}}.\boldsymbol{\nabla}\Phi(\boldsymbol{r},t)\right] + \mu_a(\boldsymbol{r}).\Phi(\boldsymbol{r},t) = S(\boldsymbol{r},t) \qquad (EII.14)$$

The DA equation has an analytical solution for $\Phi$ considering the simple case of a short-pulsed point-source inside an infinite homogenous medium given by $S(\boldsymbol{r},t,\boldsymbol{r}',t') = \delta(\boldsymbol{r}-\boldsymbol{r}').\delta(t-t')$ **(EII.15)**. The obtained solution in in accordance with Beer's law, characterized by an exponential decay due to absorption.

$$\Phi(\boldsymbol{r},t,\boldsymbol{r}',t') = \frac{c}{\left({}^{4\pi.}/_{3\mu_{tr}.ct}\right)^{\frac{3}{2}}}.e^{-\left[\frac{|\boldsymbol{r}-\boldsymbol{r}'|^2}{{}^{4}/_{3\mu_{tr}.c(t-t')}}\right]}.e^{-\mu_a(\boldsymbol{r})c(t-t')} \qquad (EII.15)$$

However, solving the equation in the case of complex heterogenous media requires the use of numerical methods such as finite-elements methods. Such implementation is computationally intensive and time-consuming.

## II.2.3. Monte Carlo model

The Monte Carlo (MC) model is a statistical approach used for modelling the photon transport. Light propagation in a medium is thus modeled as individual photons travelling between sites of interaction. In the case of biological tissues, interactions include absorption and scattering processes. Each is represented as an event associated with probabilities, related to the absorption and scattering coefficients. Thus, each movement of the simulated photons is dictated by their probability of being scattered or absorbed. This framework enables the simulation of media with less constraints compared to the diffusion approximation. Its flexibility also enables the modelling of complex geometries such as multi-layer materials [8].

A typical workflow for a semi-infinite homogenous medium is presented in **Figure II.6**. The multiple inputs determine the possible interaction and their respective probabilities. When a photon encounters a scattering site, the anisotropy factor determines its scattering angle, defining the next travelling direction. If an absorbing site is encountered, the photon is considered absorbed, and its location is recorded. In case the photon reaches the medium boundary, the refractive indices from either sides of the interface and the direction of propagation of the photon are taken into account to determine if the photon is reflected internally or exits the medium. Thus, diffuse reflectance can be established from the medium optical properties (OP).

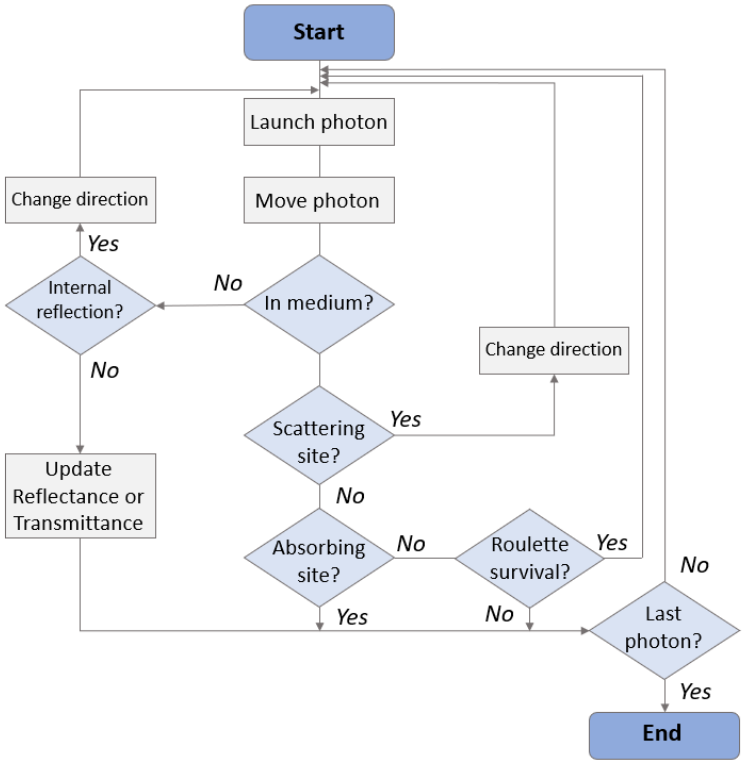


**Figure II.6 – Monte Carlo photon propagation simulation flowchart**

In order to respect the principle of energy conservation, photons can be terminated using a so-called roulette method. Practically, a weight is assigned to the photon and becomes progressively smaller as propagation through the medium goes on. When this weight drops below a chosen threshold value, the photon is randomly terminated according to a fixed probability. If the photon survives this roulette step, it weight is increased, and its propagation continues.

However, in order to achieve accurate approximations, a large number of samples must be considered. Typically, millions of photons are launched during one simulation. The MC model is fortunately adapted to parallel computing and graphics processing units (GPU) can be employed to dramatically decrease processing times [9]. The flexibility of the MC model and its ability to decouple degrees of freedom make it advantageous for inverse problem solving. For instance, the optical characterization of biological tissues consists in the estimation of the tissues optical properties based on diffuse reflectance measurements. MC simulations can be performed to create an array of diffuse reflectance values based on pairs of $\mu_a$ and $\mu_s'$ coefficients, which constitutes a look-up table (LUT) to yield an estimate the tissue optical properties from diffuse reflectance measurements [10]. Pre-computed LUTs can thus be employed to optimize processing for tissue optical characterization.

## II.3. Tissue optical characterization methods

Three main near-infrared spectroscopy (NIRS) groups of techniques for optical characterization of tissues can be distinguished. First, continuous-wave (CW) NIRS consists in space and time-independent illumination and detection of light reflected by the tissues. Collecting this information over a large spectrum enables the unmixing of contribution from the fluorophore, based on the a priori knowledge of their spectral signature, but does not provide quantitative measurements of tissue optical properties. Separating the absorption from scattering contributions to the remitted light from the tissues requires characterization of the light propagation over time or space.

To this purpose, two groups of quantitative methods were derived, either time-resolved or space-resolved. Time-domain (TD) NIRS is based on measuring the temporal point-spread function (t-PSF) by analyzing the spread of a pulse of light over time as it propagates through the tissues. Reciprocally, time frequency-domain (TFD) NIRS consists in measuring the temporal modulation transfer function (t-MTF) by characterizing the attenuation and phase delay over time of an oscillating wave propagating through the medium.

By analogy with time-resolved measurements, spatially-resolved measurements can be broken-down into two reciprocal approached. In space-domain (SD) NIRS, the measurement of the spatial point-spread function (s-PSF) is performed by measuring the spread of a point-like illumination from multiple distances. Reciprocally, spatial frequency-domain (SFD) NIRS consists in measuring the spatial modulation transfer

function (s-MTF) by using spatially structured illumination and analyzing the modulation induced by the propagation in tissue.

### II.3.1. Continuous wave near-infrared spectroscopy

CW-NIRS is solely based on the measurement of diffusively reflected light intensity after illuminating the tissue. The intensity ratio between the source and the diffusively reflected light is directly impacted by absorption and scattering within the tissues, but its measurement is neither time nor space-resolved, and consequently does not yield quantitative measurements of $\mu_a$ and $\mu_s'$ [11]. Collecting this information at several wavelengths over a large spectrum enables the unmixing of contribution from the fluorophore, provided the a priori knowledge of their spectral signature. Although, it does not provide absolute concentration extraction of chromophores but enables the monitoring of trends. A hyperspectral approach can be employed to provide information about the tissue physiology, morphology, and composition [12].

### II.3.2. Time domain near-infrared spectroscopy

TD-NIRS consists in following the light propagation over time by registering the time of arrival of reflected photons [13,14]. The travelling time through the tissue between the source and the detector is referred to as time of flight. It is characteristic of the tissue scattering and geometry. The observed intensity losses relate to both scattering and absorption phenomena. In practice, a pulse of light is sent to the tissue – typically at the picosecond scale – and detected after propagation by a synchronized photon counting system. To this purpose, time-correlated single photon counting (TCSPC) are widely employed [15]. Pulses are sent with a high repetition rate – generally in the megahertz range – to obtain significant sampling. Thus, TD-NIR measures t-PSF of tissues. The light pulse spreads according to the photons travelling paths inside the tissue: the deeper the photons travel, the later they reach the detector. The simple case of a setup with one source and one detector is illustrated in **Figure II.7**.

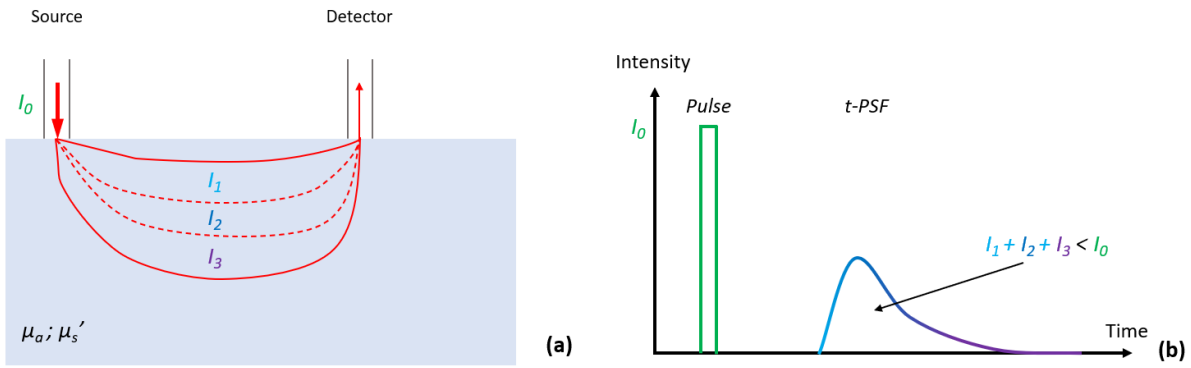


**Figure II.7 – Time-domain NIR spectroscopy principles.**

## II.3.3. Time frequency domain near-infrared spectroscopy

FD-NIRS is a derivation of TD-NIRS, using temporally modulated light instead of pulses [16-18]. Reciprocally to the measurement of the temporal point spread function with TD-NIRS, the attenuation, phase shift and modulation amplitude of the reflected signal are extracted to measure the tissue t-MTF [19]. **Figure II.8** provides an illustration of FD-NIRS for a simple configuration.

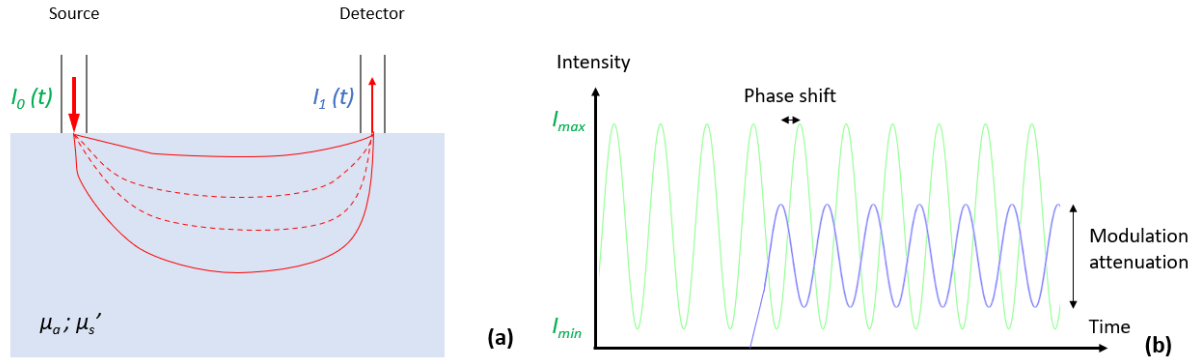


**Figure II.8 – Time frequency-domain NIR spectroscopy principles.**

Such implementation enables fast imaging, at the cost of decreased precision due to higher noise levels. Real-time quantitative mapping of optical properties and quantification of hemodynamics were demonstrated using multispectral FD-NIRS [20]. Although 2D mapping is achieved, the reconstructed images are limited to small areas of tens of cm² with a spatial resolution in the millimeter scale.

## II.3.4. Spatial domain near-infrared spectroscopy

SD-NIRS is commonly used for blood perfusion monitoring through the assessment of hemoglobin concentration in tissues. This method relies on the injection of light in the tissue and collection of the diffusively reflected light using a source-detector pair [21,22]. Measurements at different source-detector separations yield the s-PSF, characteristic of the optical properties of the medium. Multiplying the number of detectors enables the mapping of relative chromophore concentration, resulting in spatially resolved spectroscopy (SRS), and yielding functional NIR (fNIR) imaging [23]. Additionally, specific spatial arrangement of the detectors enables tomography [24].

In practice, the source-detector pairs need to be placed in contact with the tissue. In order to prevent electrical hazards when placing devices directly on the patient, the source and detectors are generally fiber-coupled. Fiber-coupling requires additional hardware and suffers from coupling losses, but offers more flexibility. As light sources, laser diodes (LD), light-emitting diodes (LED) or filtered broadband sources are commonly employed. Detectors include photodiodes (PD), avalanche photodiodes (APD) and photomultiplier tubes (PMT) [25]. An illustration in the simple case of a homogenous diffusive and absorbing medium with one source and one detector is given in **Figure II.9**.

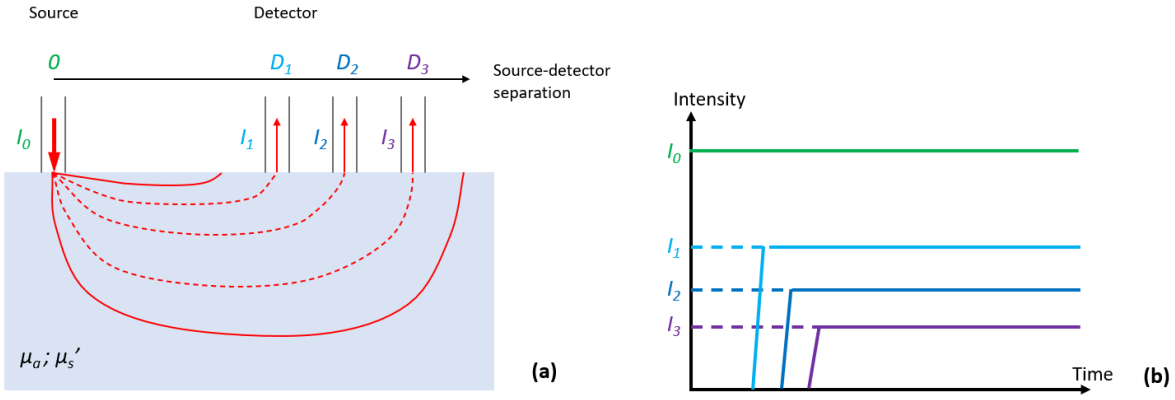


**Figure II.9 – Spatial-domain NIR spectroscopy principles.**

Overall, the three presented fNIR imaging technologies are not optimal solutions for intraoperative use. Indeed, their limited spatial resolution and their cumbersome implementation requires an array of detectors across the region of interest which must be placed in contact with the patient. However, fNIR-based wearable devices are developed for use in more naturalistic environments, improving patient comfort [26].

## II.3.5. Spatial frequency domain imaging

SFD-NIRS, also referred to as SFDI, is a technique using spatial modulation of light to measure the s-MTF of tissues [27-29]. Similarly to FD-NIRS, tissues optical properties impact the spatial modulation amplitude. The resulting diffuse reflectance is thus recorded to analyze the modulation amplitude attenuation. In practice, SFDI relies on the use of structured illumination to project on the surface of tissues a 2D sinusoidal pattern. A projection system – typically based on a digital micromirror device (DMD) coupled to a narrowband light source – creates a large illumination field. The illumination spatial frequency is analogous to the source-detector separation in the previous presented NIR spectroscopy techniques. Reflectance images are then collected using a camera. This way, widefield imaging can be achieved with high resolution, from a large working distance. Crossed polarizers are placed in the projection and detection paths to eliminate the specular reflection from the reflectance, yielding the modulated diffuse reflectance alone.

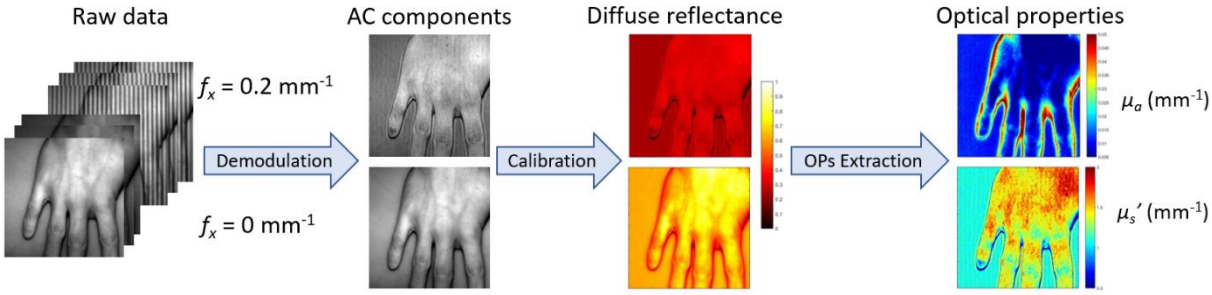


**Figure II.10 – Typical workflow for spatial frequency domain imaging. The projected spatial frequencies are 0 mm$^{-1}$ and 0.2 mm$^{-1}$. Illumination wavelength is 665 nm.**

The standard SFDI workflow is presented in **Figure II.10**. It can be decomposed in four main steps:

- Acquisition:

  Structured light is projected onto the tissues. The resulting reflectance is recorded using a camera.

- Demodulation:

  Raw reflectance data is demodulated to extract the amplitude modulation for each pixel of the image.

- Calibration:

  A calibration sample with known optical properties is imaged in the same conditions as the tissues. Using a Monte Carlo-based model, the calibration sample diffuse reflectance is predicted. By comparing the tissue amplitude modulation to that of the calibration sample, the tissue diffuse reflectance is measured.

- Optical properties extraction:

OPs extraction is an inverse problem that solves from the tissue absorption coefficient $\mu_a$ and reduced scattering coefficient $\mu_s'$. The decoupling of absorption and scattering is performed by measuring the diffuse reflectance at several illumination spatial frequencies.

*Acquisition*

The illumination part of an SFDI system consists in a light source coupled to a projection system. Narrowband light sources such as a filtered broadband source, an LED or a laser diode are employed. The projection system typically consists in a DMD-based projector. The micromirror chip is controlled to create a grayscale pattern representing the 2D sinusoidal pattern to be projected. Projection through a lens thus creates a desired structured illumination. Among the several existing demodulation methods, the most standard one is phase-shifting demodulation. This algorithm requires images with several patterns with successive phase-shifts – typically three images with successive 120° phase shifts. Consequently, the input pattern to the DMD is refreshed and images are acquired. As the OPs extraction requires diffuse reflectance measurement at several spatial frequencies, the acquisition is repeated with varying sinusoids periods. The most common implementation of SFDI requires two distinct spatial frequencies. In practice, one is chosen to be 0 $mm^{-1}$, while the second is a high frequency – generally ranging from 0.1 $mm^{-1}$ and 0.5 $mm^{-1}$.

*Demodulation*

The acquired data are then demodulated to extract the amplitude modulation at a given spatial frequency. Phase-shifting demodulation is a standard method for this purpose. Multiple algorithms exist, requiring different number and values of phase shifts [30]. Three phase shifts of 120° is the most commonly encountered scheme for SFDI. The detected reflected intensity *I* by the camera can be expressed as the sum of a planar component $I_{DC}$ (DC) and a spatially modulated component $I_{AC}$ (AC). Given the illumination spatial frequency $f_x$ along the $x$ direction and $\varphi$ the pattern phase shift, the AC component is expressed as follows, with $M_{AC}$ being the modulation amplitude of the detected signal **(EII.16)**:

$$I_{AC} = M_{AC}(x, f_x).\cos(2\pi.f_x.x + \phi) \qquad (EII.16)$$

With three phase shifts $\varphi_1$, $\varphi_2$ and $\varphi_3$ of 0°, 120° and 240°, respectively, the corresponding recorded images $I_1$, $I_2$ and $I_3$ can be manipulated to calculate the modulation amplitude for each pixel of the image **(EII.17)**. The amplitude of the DC component can be extracted from any illumination frequency **(EII.18)**, yielding the amplitude modulation for $f_x = 0\ \mathrm{mm}^{-1}$. In practice, it is instead preferable to acquire a separate set of images with $f_x = 0\ \mathrm{mm}^{-1}$ and use **(EII.17)** to obtain the DC component, as this operation eliminates features common to all three images such as dark noise or constant ambient light. Indeed, the DC component obtained using **(EII.18)** contains the mean of background and noise components present in $\mathrm{I}_1$, $\mathrm{I}_2$ and $\mathrm{I}_3$, which must not be taken into account as contribution to the reflectance.

$$M_{AC} = \frac{2^{1/2}}{3}[(I_1 - I_2)^2 + (I_2 - I_3)^2 + (I_3 - I_1)^2]^{1/2} \quad (EII.17)$$

$$M_{DC} = \frac{1}{3}.(I_1 + I_2 + I_3) \quad (EII.18)$$

*Calibration*

In such a configuration, the modulation amplitude $M_{AC}$ is the product of the source intensity $I_0$; the MTF of the projection illumination and detection systems $MTF_{system}$; and the diffuse reflectance of the tissue $R_d$ **(EII.19)**. Consequently, it is possible to calibrate simultaneously for the source intensity and optical system MTF by measuring the modulation amplitude $M_{AC,ref}$ on a tissue-mimicking phantom with known optical properties as calibration sample. Typically, a Monte Carlo-based model is employed to predict the calibration phantom diffuse reflectance $R_{d,ref,pred}$. The diffuse reflectance of the tissue in each pixel of the image is then computed **(EII.20)**. $R_d$ being a function of $f_x$, the system must be calibrated for every spatial frequency employed.

$$M_{AC} = I_0.MTF_{system}.R_d \quad (EII.19)$$

$$R_{d(f_x)} = \frac{M_{AC}(f_x)}{M_{AC,ref}(f_x)}.R_{d,ref,pred}(f_x) \quad (EII.20)$$

*Optical properties extraction*

The extraction of the tissue optical properties maps consists in solving the inverse problem for $\mu_a$ and $\mu_s'$ at each pixel of the image, from the measurements of diffuse reflectance at different spatial frequencies. A popular solution employed is the generation of lookup tables using Monte Carlo models. Such LUTs are built by generating an array of diffuse reflectance based on pairs of $\mu_a$ and $\mu_s'$ coefficients over large ranges. LUTs can be efficiently pre-computed using GPUs. A set of two diffuse reflectance measurements at two distinct spatial frequencies is thus sufficient to determine a unique solution for $\mu_a$ and $\mu_s'$. An interpolation step is involved to estimate the coefficients, since the LUTs are generated with a finite sampling rate. This step is computationally inexpensive and enables fast processing of the images.

In practice, this workflow produces valid measurement only in the case where the measured sample is flat and placed at the same working distance the calibration was performed. Indeed, varying working distance within the field of view would introduce bias in the modulation amplitude, thus distorting the optical properties maps. To this purpose, profilometry measurements and a height calibration can be introduced in the workflow [31]. An illustration of profile-corrected SFDI is shown in **Figure II.11**. Taking advantage of the projection system, a phase shifting-profilometry can be implemented. An additional set of images is acquired and demodulated to extract the phase shift profile of the sample, with respect to the reference calibration plane. The phase shift with respect to the calibration plane is proven to be linked to the height

shift with a simple relationship [32]. By performing the calibration step at different working distances, the reference modulation amplitude can be adapted to compensate for varying working distances, given the topography of the sample. Thus, height-corrected $M_{AC}$ maps are computed, yielding accurate optical properties extraction.

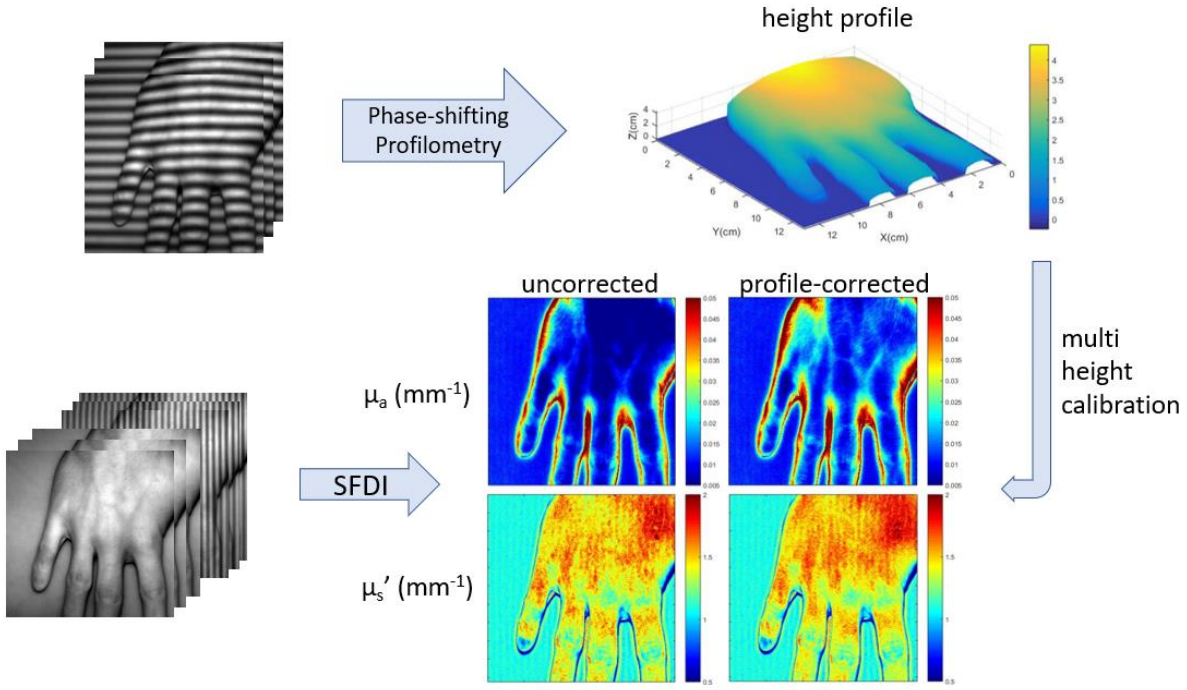


**Figure II.11 – Profile-corrected SFDI workflow.**

Overall, the processing steps are not computationally intensive, leading to fast image processing. Moreover, workflow can be optimized using highly parallelized computing on GPUs. However, the multiple image acquisition is time consuming and as such SFDI is not real-time compatible, thus unsuitable for intraoperative use.

An alternative implementation of SFDI named Single Snapshot imaging of Optical Properties (SSOP) has been derived, reducing the number of required images to only one high frequency image by performing the demodulation in the Fourier space [33]. An adapted SSOP workflow for profile-corrected measurements has also been proposed [34]. A pair of low-pass and high-pass filters are used for filtering the DC and AC components, respectively. The Fourier space filtering being prone to creating artifacts and causing resolution loss in the images, a combination of anisotropic filters has been proposed, increasing the image quality [35]. Finally, an approach using deep learning (DL) for demodulation has been developed, yielding high-quality, profile-corrected imaging also from a single high frequency image input [36].

For more practical information about SFDI, an open-source guide for building a low-cost, compact, multispectral SFDI system has been proposed, along with a dedicated website providing detailed assembling

instruction and comprehensive resources to operate the system. In Chapter III, the applications of SFDI for endogenous functional and structural imaging are detailed [37].

**References**


[1] Khan R., Gul B., Khan S., Nisar H., Ahmad I., ‘’Refractive index of biological tissues: Review, measurement techniques, and applications’’, Photodiagnosis and Photodynamic Therapy, 33, (2021)

[2] G.C. Psarras, ''2 - Fundamentals of Dielectric Theories'', in Plastics Design Library, Dielectric Polymer Materials for High-Density Energy Storage, edited by Dang Z.M., William Andrew Publishing, pp. 11-57, (2018)

[3] Gaponenko S., Demir H., ''Applied Nanophotonics'', Cambridge University Press, pp. 210-226, (2018)

[4] Datta R., Heaster T. M., Sharick J. T., Gillette A. A., Skala, M. C., ‘’Fluorescence lifetime imaging microscopy: fundamentals and advances in instrumentation, analysis, and applications’’, Journal of biomedical optics, 25(7), pp. 1–43, (2020)

[5] Monici M., ‘’Cell and tissue autofluorescence research and diagnostic applications’’, Biotechnology Annual Review, 11, pp. 227–56, (2005)

[6] Carminati R., Schotland J., ''Radiative Transport and Diffusion'', in Principles of Scattering and Transport of Light, Cambridge University Press, pp. 145-146, (2021)

[7] Carminati R., Schotland J., ''Diffusion Approximation'', in Principles of Scattering and Transport of Light, Cambridge University Press, pp. 172-178, (2021)

[8] Wang L.H., Jacques S.L., Zheng L.Q., "MCML—Monte Carlo modeling of light transport in multi-layered tissues", Computer Methods and Programs in Biomedicine, 47(2), pp. 131–146, (1995)

[9] Alerstam E., Svensson T., Andersson-Engels S.,‘’Parallel computing with graphics processing units for high speed Monte Carlo simulation of photon migration’’, Journal of Biomedical Optics Letters, 13, 060504, (2008)

[10] Hennessy R., Lim S.L., Markey M.K., Tunnell J.W., ‘’Monte Carlo lookup table-based inverse model for extracting optical properties from tissue-simulating phantoms using diffuse reflectance spectroscopy’’, Journal of Biomedical Optics, 18(3), 037003, (2013)

[11] Scholkmann F., Kleiser S., Metz A.J., Zimmermann R., Mata Pavia J., Wolf U., Wolf M., ‘’A review on continuous wave functional near-infrared spectroscopy and imaging instrumentation and methodology’’, NeuroImage, 85(1), pp. 6-27, (2014)

[12] Lu G., Fei B., ‘’Medical hyperspectral imaging: a review’’, Journal of Biomedical Optics, 19(1), 010901, (2014)

[13] Welch A.J., Yoon G., van Gemert M.J., ''Practical models for light distribution in laser-irradiated tissue'', Lasers in Surgery and Medicine, 6(6), pp. 488–493, (1987)

[14] Yoo K., Alfano R., ''Determination of the scattering and absorption lengths from the temporal profile of a backscattered pulse'', Optics Letters, 15(5), pp. 276–278, (1990)

[15] O’connor D.V., Phillips D., ‘’Time Correlated Single Photon Counting’’, Academic Press: London, UK, (1984)

[16] O’Leary M.A., Boas D.A., Chance B., Yodh A.G., ''Refraction of diffuse photon density waves'', Physical Review Letters, 69(18), pp. 2658–2661, (1992)

[17] Fishkin J.B., Gratton E., ''Propagation of photon-density wavesin strongly scattering media containing an absorbing semi-infinite plane bounded by a straight edge'', Journal of the Optical Society of America, 10(1), pp. 127–140, (1993)

[18] Svaasand L.O., Spott T., Fishkin J.B., Pham T., Tromberg B.J., Berns M.W., ''Reflectance measurements of layered media with diffuse photon-density waves: a potential tool for evaluating deep burns and subcutaneous lesions'', Physics in Medicine and Biology, 44(3), pp. 801–813, (1999)

[19] Davies D.J., Clancy M., Lighter D., Balanos G.M., Lucas S.J.E., Dehghani H., Su Z., Forcione M., Belli A., ‘’Frequency-domain vs continuous-wave near-infrared spectroscopy devices: a comparison of clinically viable monitors in controlled hypoxia’’, Journal of Clinical Monitoring and Computing, 31, pp. 967–974, (2017)

[20] Stillwell R.A., Kitsmiller V.J., Wei A.Y., Chong A., Senn L., O’Sullivan T.D., "A scalable, multi-wavelength, broad bandwidth frequency-domain near-infrared spectroscopy platform for real-time quantitative tissue optical imaging", Biomedical Optics Express, 12, pp. 7261-7279, (2021)

[21] Bonner R.F., Nossal N., Havlin S., Weiss G.H., ''Model for photon migration in turbid biological media'', Journal of the Optical Society of America, 4(3), pp. 423–432, (1987)

[22] Farrell T.J., Patterson M.S., Wilson B., ''A diffusion theory model of spatially resolved, steady-state diffuse reflectance for the noninvasive determination of tissue optical properties in vivo'', Medical Physics, 19(4), pp. 879–888, (1992)

[23] Ferrari M., Quaresima V., ‘’A brief review on the history of human functional near-infrared spectroscopy (fNIRS) development and fields of application’’, Neuroimage, 63(2), pp. 921–935, (2012)

[24] Joseph D.K., Huppert T.J., Franceschini M.A., Boas D.A., ‘’Diffuse optical tomography system to image brain activation with improved spatial resolution and validation with functional magnetic resonance imaging’’, Applied Optics, 45(31), pp. 8142–8151, (2006)

[25] Liu J., ‘’Photonic Devices’’, Cambridge: Cambridge University Press, (2005)

[26] Pinti P., Aichelburg C., Gilbert S., Hamilton A., Hirsch J., Burgess P., Tachtsidis I., ‘’A Review on the Use of Wearable Functional Near-Infrared Spectroscopy in Naturalistic Environment’’ Japanese Psychological Research, 60(4), pp. 347–373, (2018)

[27] Dognitz N., Wagnieres G., ''Determination of tissue optical properties by steady-state spatial frequency-domain reflectometry'', Lasers in Medical Science, 13, pp. 55–65, (1998)

[28] Cuccia D.J., Bevilacqua F., Durkin A.J., Tromberg B.J., ''Modulated imaging: quantitative analysis and tomography of turbid media in the spatial-frequency domain'', Optics Letters, 30(11), pp. 1354–1356, (2005)

[29] Cuccia D.J., Bevilacqua F., Durkin A.J., Ayers F.R., Tromberg B.J., "Quantitation and mapping of tissue optical properties using modulated imaging", Journal of Biomedical Optics, 14(2), 024012, (2009)

[30] Novák J., Novák P., Mikš A., "Multi-step phase-shifting algorithms insensitive to linear phase shift errors", Optics Communications, 281(21), pp. 5302-5309, (2008)

[31] Gioux S., Mazhar A., Cuccia D.J., Durkin A.J., Tromberg B.J., Frangioni J.V., ‘’Three-dimensional surface profile intensity correction for spatially modulated imaging’’, Journal of Biomedical Optics, 14(3), 034045, (2009)

[32] Zhou W.-S., Su X.-Y., “A direct mapping algorithm for phase-measuring profilometry,” Journal of Modern Optics, 41, pp. 89-94, (1994)

[33] Vervandier J., Gioux S., "Single snapshot imaging of optical properties", Biomedical Optics Express, 4, pp. 2938-2944, (2013)

[34] van de Giessen M., Angelo J.P., Gioux S., "Real-time, profile-corrected single snapshot imaging of optical properties", Biomedical Optics Express, 6(10), pp. 4051-4062, (2015)

[35] Aguénounon E., Dadouche D., Uhring W., Gioux S., “Single snapshot of optical properties image quality improvement using anisotropic 2D windows filtering”, Journal of Biomedical Optics, 24(7), 071611, (2019)

[36] Aguénounon E., Smith J.T., Al-Taher M., Diana M., Intes X., Sylvain Gioux S., “Real-time, wide-field and high-quality single snapshot imaging of optical properties with profile correction using deep learning”, Biomedical Optics Express, 11(10), pp. 5701-5716, (2020)

[37] Applegate M.B., Karrobi K., Angelo J., Austin W.M., Tabassum S.M., Aguénounon E., Tlbury K., Saager R.B., Gioux S., Roblyer D.M., ‘’OpenSFDI: an open-source guide for constructing a spatial frequency domain imaging system’’, Journal of Biomedical Optics, 25(1), 016002, (2020)

# III.Intraoperative guidance using near-infrared optical imaging

In this chapter, the use of advanced diffuse optical near-infrared imaging for intraoperative guidance is discussed. Endogenous imaging is first described, presenting the use of SFDI for the extraction of absolute chromophore concentration, but also physiological parameters and structural parameters. This label-free method has the potential to yield crucial information for intraoperative tissue status assessment. Second, the use of exogenous fluorescence imaging for routine clinical care is discussed. Finally, current commercially available imaging devices are presented.

## III.1. Endogenous near-infrared imaging

### III.1.1. Chromophore extraction

Light absorption in biological tissues is caused by molecular constituents. Each molecule has a unique spectral signature characterized by its extinction coefficient. Thus, the optical absorption results in the combined contributions of each chromophore contained in the tissues. A combined plot of the most represented chromophores with significant absorption in the visible and NIR ranges is shown in **Figure III.1**. The data were compiled from various sources [1-3]. These constituents include: hemoglobin (Hb), water and lipids.

- Hemoglobin

  Hemoglobin is a metalloprotein found in red blood cells responsible for oxygen transport from the lungs to the rest of the body. Within hemoglobin are four heme groups based on an iron (Fe) ion. Dioxygen molecules ($O_2$) can bind to this site and consequently be carried through the body. The captured oxygen is then released to enable cellular respiration and metabolic functions. When carrying oxygen, hemoglobin is referred to as oxyhemoglobin ($HbO_2$) whereas without bound oxygen it is called deoxyhemoglobin (HHb). Typically for a healthy human individual, hemoglobin concentration per liter of whole blood is around 150 g/L. Hemoglobin represents 35 % of the red blood cells' content, while most of the rest in mainly water [4]. Given its high content within blood, the hemoglobin concentration is thus a good indicator for blood perfusion monitoring. The significant spectra differences yield the ability to optically distinguish HHb from $HbO_2$ enables the assessment of cellular metabolism and consequently tissue viability [5,6].

- Water

  Water is a major constituent of the human body. It constitutes a solvent in which metabolic functions occur. This molecule is also itself involved in metabolic functions such as respiration. Its negligeable contribution in tissue optical absorption in the visible and NIR ranges is offering a transparency optical window to observe tissue. Water absorption significantly increases past 1000 nm.

- Lipids

  Lipids designate macromolecules such as fatty acids, phospholipids, triglycerides. These are main components of cellular and intracellular membranes. Lipids also constitute the majority of adipose tissue – or fat – generated for energy storage. Being irrelevant for most clinical applications, their absorption is considered a constant contribution to the overall absorption of the tissues. As such, the presence of lipids does not interfere with other dynamic relative measurements of chromophores such as Hb or $HbO_2$.

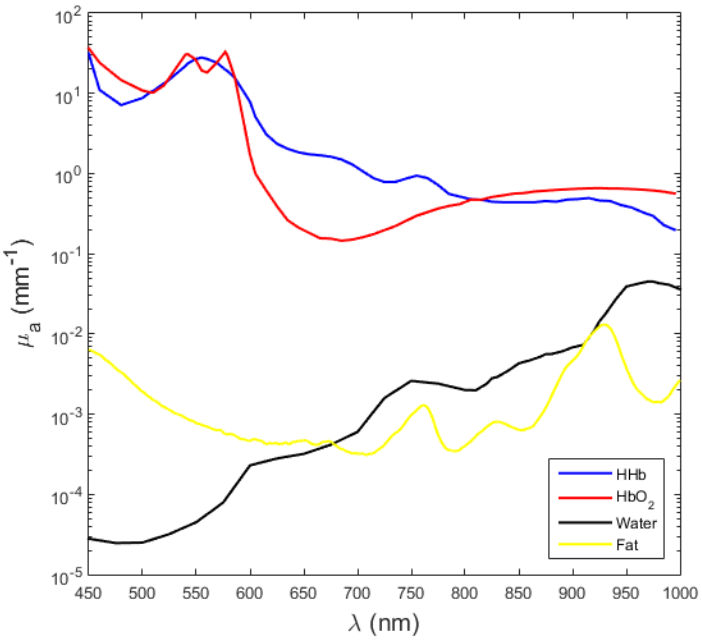


**Figure III.1 – Absorption spectra of selected chromophore present in biological tissue.**

Beer's law describes the absorbance $A$ at a wavelength $\lambda_0$ of a medium containing an attenuating compound as the product of the molar attenuation coefficient of the compound $\varepsilon$, the optical path length $d$ and the molar concentration $C$ of the compound **(EIII.1)**. Considering a mixture of chromophores in a medium, the absorbance at the macroscopic level is thus given by the sum of each individual contribution **(EIII.2)**. Thus, the absorption coefficient of such a medium is given by **(EIII.3)**.

$$A(\lambda) = \epsilon(\lambda).d.C \qquad (EIII.1)$$

$$A(\lambda) = \sum_i \epsilon_i(\lambda).d.C_i \qquad (EIII.2)$$

$$\mu_a(\lambda) = \ln(10).\sum_i \epsilon_i(\lambda).d.C_i \qquad (EIII.3)$$

From the measurement of $\mu_a$ at multiple wavelengths, **(EIII.3)** can be inverted to retrieve the contribution of each individual component. This spectral unmixing is based on the *a priori* knowledge of the presence of each constituent in the medium and their respective extinction coefficients. Ultimately it yields the chromophores concentrations. Tabulated values of extinction coefficient are widely available.

The inversion of Beer's law requires a multispectral measurement of absorption, consequently requiring extensive data acquisition. If SFDI is capable of imaging µa in real-time quantitatively over large FOVs with high spatial resolution, the acquisition of images at several wavelengths considerably slows down the imaging process, compromising the real-time capabilities of the method. The next sub-section presents approaches to achieve real-time chromophore concentration imaging with SFDI, along with applications to functional imaging.

### III.1.2. Functional imaging: physiological parameters monitoring

Physiological activities within the body can be monitored through the evolution of molecular concentrations or indicators derived from these concentrations. For instance, tissue oxygen saturation ($StO_2$) represents the fraction of oxyhemoglobin relative to the total hemoglobin in the blood. Its value – usually expressed in percents – is calculated as the ratio of the $HbO_2$ concentration *[$HbO_2$]* and the total Hb concentration *[HbT] = [HHb] + [$HbO_2$]* **(EIII.4)**. The oxygenation rate in tissues being directly related to the blood flow and cellular respiration, it represents a major indicator of blood perfusion. For instance, a decrease in $StO_2$ is characteristic of a lack of blood supply to the tissue – referred to as ischemia. In complement to $StO_2$ monitoring, variations in oxyhemoglobin and deoxyhemoglobin concentrations may reflect occurring arterial and venous occlusions [7].

$$StO_2 = \frac{[HbO_2]}{[HHb] + [HbO_2]} \qquad (EIII.4)$$

In practice, *[HHb]* and *[$HbO_2$]* are extracted from absorption coefficients measured in the 650nm to 900nm range. This window features low absorption from most of the biological tissues constituents, enabling in-depth probing. HHb and $HbO_2$ being the main absorbers in this range, Beer's law can be extracted from $\mu_a$ measured at two wavelengths. For an accurate separation of the two contributions, the wavelengths must be chosen in accordance with the individual spectra of HHb and $HbO_2$. An optimal wavelength pair of 670 nm and 850 nm wavelengths for *in-vivo* hemodynamic tissue measurements has been proposed [8].

SFDI-based $StO_2$ imaging has been demonstrated in human studies for skin flap oxygenation assessment during reconstructive breast surgery [7]. The measured $StO_2$ rate was proven to be accurate, showing results within 10 % of those made with an independent FDA-approved local probe device (ViOptix). Additionally, the visualization of oxygenation over large areas of tissue comforts the added value of using SFDI for $StO_2$ imaging. Although the employed imaging system was based on several cameras for performing fast multispectral acquisitions, the standard implementation of SFDI did not yield real-time imaging.

Temporal modulation of illumination has been proposed to achieve wavelength multiplexing as an alternative for achieving multispectral acquisition of SSOP data with a fast framerate [9]. In complement, the development of a dedicated GPU processing implementation demonstrated the extraction 1 mega-pixel (MP) oxygenation images in 1.6 milliseconds, making the whole imaging process real-time compatible [10]. This workflow is illustrated in **Figure III.2**. The remaining image artifacts inherent to the SSOP processing and lack of profile-correction may be addressed by employing a deep learning-based approach for spatial demodulation [11].

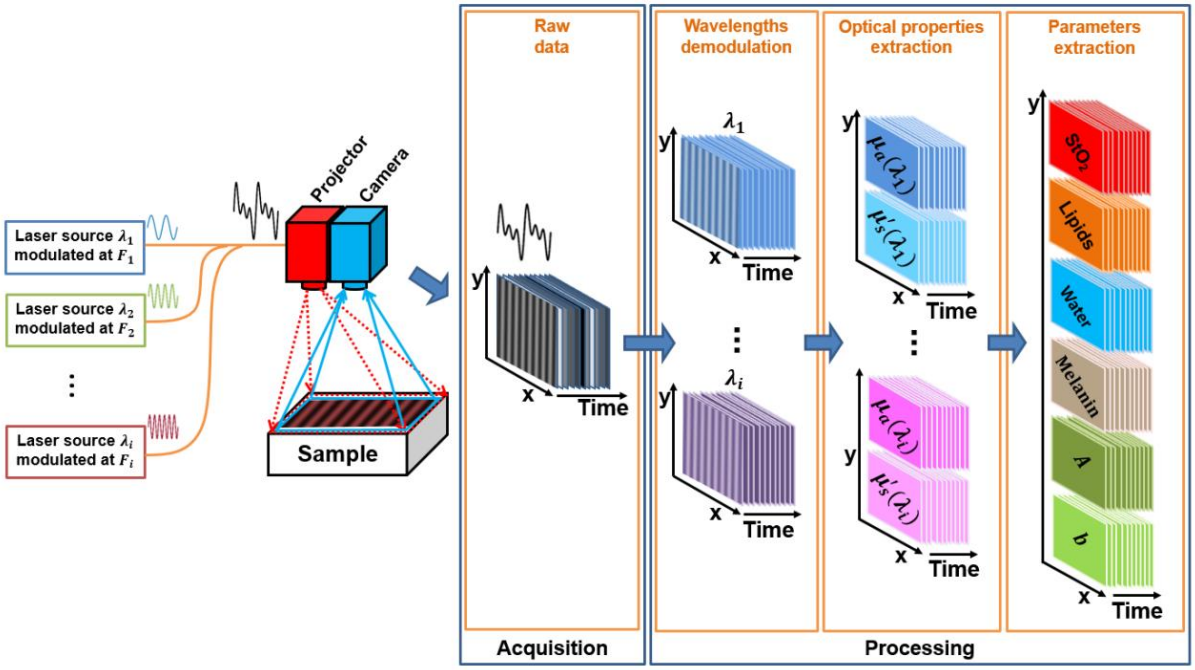


**Figure III.2 – SSOP imaging using spatio-temporal modulation of light [9].**

## III.1.3. Structural imaging: scattering parameters extraction

Light scattering in tissues is representative of the interaction with nanometric and micrometric biological structures. At the macroscopic level, the observed scattering is a combination of the contributions from structures scaling from cellular membranes to organelles to whole cells with typical sizes ranging from 10 nm to 10 µm. Given the variety of scatterer sizes and shapes, the Rayleigh's scattering model or Mie's

scattering model alone cannot describe accurately the structure of the tissue. Scattering of light in tissue is thus often modeled by a mixed Rayleigh-Mie power law over the wavelength $\lambda$ around a reference wavelength $\lambda_0$ with the following parameters: the scattering amplitude $A$, and the scattering power $b$ related to the Mie scattering model **(EIII.5)**. Typical values for these parameters per tissue type can be found in the literature [12].

$$\mu_s'(\lambda) = A.\left(\frac{\lambda}{\lambda_0}\right)^{-b} \qquad (EIII.5)$$

**Figure III.2** shows a workflow for the extraction of scattering parameters in real-time using SSOP. In practice, the model fitting can be achieved from the measurement of $\mu_s'$ at three different wavelengths, yielding scattering amplitude and power maps. The scattering amplitude is directly related to the density of scatterers, while the scattering power is related to the size distribution of the scatterers.

In turn, SFDI is capable of providing contrast imaging based on the scattering power $b$ and amplitude $A$ of tissues. Its ability to characterize structural microscopic changes within the tissues make it a powerful tool for various clinical applications, such as the prevention of chronic foot ulceration in patients with diabetes, the monitoring of tumor treatment response or the time categorization of burn wounds severity [13-15].

## III.2. Exogenous near-infrared imaging

While endogenous imaging takes advantage of light interaction with the tissues structural features and molecular constituents, exogenous imaging makes use of contrast agents to highlight structural features within the body including vasculature or the lymphatic system, but also lesions such as tumors of all types. This section focuses on the use of near-infrared fluorescent contrast agents in macroscopic NIR fluorescence imaging.

### III.2.1. Fluorescent contrast agents

Similarly to other medical imaging modalities, fluorescent contrast agents are employed in optical imaging to enhance the detection of structures of interest or highlight physiological activities. These agents are injected preoperatively or intraoperatively depending on the application and the molecule's characteristics. Both targeted and non-targeted fluorophores exist.

Two of the most frequently employed non-targeted fluorophores for fluorescence image-guided surgery (FIGS) are methylene blue (MB) and indocyanine green (ICG). Both of these agents are approved by United States Food and Drug Administration (FDA) and the European Medicines Agency (EMA). MB and ICG are respectively referred to as 700 nm and 800 nm dyes in relation to their emission spectra located in these ranges. Since these fluorescent dyes feature peak excitation and detection in the NIR range, they enable in-depth assessment of structures of interest [16]. Moreover, these radiations being invisible to the surgeon, no interference with clinical workflow is noticeable. The use of such contrast agents for structural imaging is detailed below.

Targeted fluorescent agents are the combination of a fluorophore and a targeting agent such as antibodies or peptide fragments. Popular fluorescent tracers include 800 nm dyes such as cRGD-ZW800-1, bevacizumab-800CW and SGM-101, all currently involved in advanced clinical trial phases [17]. Their promising application to cancer surgery comforts the need for fluorescence imaging in the operating room [18].

### III.2.2. Structural features imaging

NIR FIGS can be used as an alternative to other medical imaging modalities for structural imaging. There are numerous applications in cancer surgery, from the tumor detection and margin assessment to the reconstruction procedures. Another use of fluorescence imaging is dedicated to preserving vital structures from damage during surgery by highlighting them. A non-exhaustive list of examples is presented below.

- Sentinel lymph nodes mapping

  A sentinel lymph node (SLN) is the first lymph node draining a tumor. This site is thus most prone to the development of lymphogenic metastases and must generally be resected. The use of fluorescence imaging enables inspection of the lymph drainage and accumulation in the lymph node after peritumoral injection of a fluorophore. In turn, the SLNs can be mapped, and resected while preserving as much as healthy tissue as possible [19]. ICG and MB have been widely used for this application.
- Hepatic metastases imaging:

  Hepatic metastases can be delineated using ICG. This compound is exclusively cleared by the liver, where lesions might be located. Their presence perturbates the excretion of ICG into bile, causing the ICG to accumulate around the tumor. A rim of fluorescence is thus visible around the tumor site, enabling margin assessment [20].
- Ureter imaging:

The ureter can be highlighted during distal colon and rectum surgery to avoid any accidental damage to it. The use of dyes such as MB, ZW800-1, IS-001 and IRDye-800BK have been reported for this application [21]. Alternatively, the use of a fluorescent coated catheter has been reported, enabling constant visualization of the ureter as opposed to injected dyes [22].

- Anastomotic perfusion:

  ICG fluorescence angiography can be performed to assess blood perfusion during reconstruction procedures [23,24]. In bowel surgery, anastomoses are prone to leakage if the reconstruction includes ischemic tissue. Anastomotic leakage is a frequent complication inherent to colorectal cancer surgery that can benefit from enhanced blood perfusion assessment.

- Nerves imaging:

  Using targeted agents, nerves imaging can be achieved during surgery in order to preserve them during resection procedures. Fluorescent probes are in development but still need to be translated to the clinic [25].

### III.2.3. Fluorescent tumor tracers

A very promising application for targeted fluorescent agents is tumor surgery. By employing tracers targeting tumor cells, fluorescence imaging yields enhanced tumor detection and margin assessment. Such tracers are obtained by the combination of a fluorophore and an antibody or peptide fragment, capable of binding to tumor cells or compounds overexpressed by these cells. This aims at achieving more complete resections, while preserving healthy surrounding tissue. Typically, these tracers exhibit higher signal at the tumor site with a tumor-to-background ratio (TBR) over 2. Currently undergoing clinical translation fluorophores include: cRGD-ZW800-1, SGM-101, IS-002 and bevacizumab-800CW [26-28]. The ONM-100 tracer offers a slightly different approach for tumor targeting. It consists in a pH-sensitive nanoparticle conjugated with ICG which exploits the metabolic microenvironment of solid tumors to create an activable fluorophore [29].

Therefore, the concurrent development of fluorescent agents and fluorescence imaging systems bears potential to enhance intraoperative guidance, consequently improving the patient's outcome [30].

## III.3. Commercially available imaging systems

Considering the growing number of applications for NIR optical imaging for intraoperative guidance, the market for imaging devices is expanding rapidly. This section presents a non-exhaustive panel of commercially available systems, their capabilities to assist procedures in a clinical environment and their impact on specific surgical procedures. First, exogenous fluorescence imaging systems are discussed. This technology being more mature, it is currently involved in routine clinical care. Second, functional endogenous imaging devices are presented. Based on a more recent technology, these have the potential to yield more objective and accurate tissue status assessment.

### III.3.1. Fluorescence imaging

The deployment of NIR fluorescence image-guided surgery has intensified with the multiple developments of fluorophores and imaging systems [31]. Their use in clinical routines ranges from blood flow and tissue perfusion imaging, transfer circulation imaging in free flaps, plastic surgery, reconstructive surgery, or lymphatic imaging. While ICG is almost the only fluorophore used in the clinic, NIR fluorescence imaging systems are also extensively use for the clinical translation of new molecules, especially the emerging targeted agents [32].

Several key features can be set as desirable criteria for such imaging devices [33]:

- Real-time overlay of visible and fluorescence images

  The overlay in real time of color images and fluorescence images is important to easily associate the anatomical view with fluorescence signals. This directly improves the surgical field navigation. To this purpose, imaging systems feature processing including co-registration of images, color mapping and overlay algorithms. Guidelines for overlaying visible and fluorescence images have been proposed to optimize the visualization [34].
- Operation with ambient room light

  Ambient room lightning can feature a strong emission in the NIR spectral range. Consequently, background noise in the fluorescence images can rise, leading to decreased sensitivity for the imaging device. If simply switching off the operating room lights is a solution, it greatly interferes with the surgical workflow. Alternatively, ambient light can be provided by white LEDs that feature low NIR light emission. Technical solutions can be implemented as well to circumvent this issue: imaging devices exist with parasite light rejection systems such as excitation modulation paired with lock-in detection.

- High sensitivity

  The ability to image fluorescence emissions efficiently while maintaining a large working distance and high framerate is inherent to the sensitivity of an imaging system. High sensitivity along with suitable imaging conditions results in high signal-to-background ratio (SBR), enabling a better appreciation of contrast and finer structures details retrieval. Moreover, high sensitivity is key when using targeted agents, as their concentration in tissue is typically low. To this purpose, imaging systems can be equipped with high performance sensors, coupling high efficiency, low noise levels and gain control ability.

- Multiple fluorophores imaging

  Multiple fluorophores imaging is typically interesting when imaging a combination of targeted and non-targeted agents, highlighting vital structures and diseased tissues for instance. This multichannel functionality requires the implementation of multiple excitation sources combined with a multiple detection system, featuring complex sensors and filtering configurations. This criterium represents additional hardware and software requirements, especially considering overlaying images.

- Ergonomic use

  Even if such systems are designed to be integrated to the surgical workflow with minimum interference, different ergonomics approaches can be distinguished. A few handheld devices exist in very compact and portable forms, suitable for providing access to complex geometries. However, such systems show limited capabilities due to design compromises. The majority of systems consist in wheel-based platforms with larger footprints but also extended capabilities in terms of acquisition, processing and visualization. Finally, laparoscopic implementations are emerging, introducing fluorescence guidance into minimally invasive surgical workflows, where the visual capabilities of the surgeons are very limited, in addition to being deprived of palpation for navigation.

A non-exhaustive list of FDA-approved devices is presented in **Table III.1**. A selection of devices is shown as illustration in **Figure III.3**. Fluorescence imaging produces contrast images, representing the presence or absence of fluorophore in the tissue. The qualitative aspect of this imaging modality limits its impacts on consensus finding while investigating new clinical procedures. To this purpose, functional imaging can provide objective, quantitative and reliable inputs for better-founded decision making and improved patient outcome.

| Company | product | Mode | NIR channels | Real-time overlay | FDA approval |
|---|---|---|---|---|---|
| Fluoptics | Fluobeam® | Handheld | 1 | No | 2014 |
| Hamamatsu | PDE Neo II | Handheld | 1 | No | 2012 |
| Stryker | SPY-PHI | Handheld | 2 | No | 2017 |
| Stryker | SPY Elite | Open air | 2 | Yes | 2005 |
| Medtronic | EleVision™ IR | Open air | 1 | Yes | |
| Quest | Spectrum® | Open air Laparoscopy | 3 | Yes | 2015 |
| Karl Storz | Vitom® ICG | Open air Laparoscopy | 2 | No | 2016 |
| Stryker | Pinpoint | Laparoscopy | 1 | Yes | 2018 |
| Intuitive | Firefly | Robotic laparoscopy | 1 | No | 2014 |

**Table III.1 – Comparison of various fluorescence image-guided surgery devices. Information compiled from various reviews [33,34].**


**Figure III.3 – A selection of various fluorescence image-guided surgery devices [35-39].**

## III.3.2. Functional imaging

HSI has the capability to measure relative concentrations of multiple chromophores, suitable for tissue identification, and extraction of clinical indices such as $StO_2$, organ hemoglobin index, NIR perfusion index,

tissue water index, and tissue lipid index [40]. The Tivita® 2.0 and Tivita® Mini are commercially available HSI devices developed by Diaspective Vision GmbH for open surgery and minimally invasive surgery, respectively. The use of such technology has been demonstrated in clinical studies for visceral surgery and transplantation surgery:

- Visceral surgery

  The vascularization and integrity of tissues can be assessed to assist anastomoses procedures, as HSI produces inputs to determine the optimal resection line or anastomotic region. The intraoperative feasibility was demonstrated for various organs across the abdominal cavity such as the esophagus, pancreas, small bowel, colon and liver [41,42].
- Transplantation surgery

  The use of HSI for assessment of donor kidney quality and function in human kidney allotransplantation was demonstrated, enabling the prediction of delayed graft function, but also providing information about the kidney parenchyma and ureter viability throughout the surgical procedure [43].

However, due to the extensive data acquisition and processing inherent to HSI, such devices do not enable real-time monitoring of the forementioned parameters and indices, as the acquisition time alone is approximately 6 seconds long.

Since the emergence of SFDI a decade ago, its relevance for various clinical applications has been demonstrated. Two SFDI-based devices are currently commercially available, both developed by Modulim (Irvine, CA, USA) as shown in **Figure III.4**. Clarifi® is a multispectral imaging platform capable of non-invasive transcutaneous measurements of five biomarkers as metrics for oxygenation and perfusion, including $StO_2$, [$HbO_2$], [HHb] but also total hemoglobin concentrations in either superficial or deeper tissues. Clinicians are thus able to assess non-invasively within seconds the microvascular system. Its primary clinical application is the prevention of diabetic foot ulcers and peripheral arterial diseases, and the monitoring of post-surgery recovery [44]. Reflect RS® is a customizable research platform for academia and industry, with similar features than the Clarifi system. The Clarifi system received in 2018 FDA clearance for determining oxygenation levels in superficial tissues for patients with potential circulatory compromise. The use of such technology extends to several clinical applications, as demonstrated in human studies:

- Diabetic foot ulcers

  Poor peripheral circulation in diabetes patients accentuates silent vascular changes, possibly leading to a diabetic foot ulcer and peripheral arterial disease. The lack of non-invasive testing can lead to underdiagnosed diseases and eventually amputation. SFDI was used to identify unique signatures of compromised circulation in patients, providing a non-invasive way of assessing risks [44].

- Reconstructive surgical flaps

  Reconstructive flap procedures following mastectomies or other surgeries require accurate oxygenation and perfusion assessment. In contrast to the current standard of care relying on the subjective evaluation of tissue discoloration and temperature, SFDI provides clinicians with objective metrics of tissue oxygenation and perfusion [45].
- Burn wounds

  The diagnosis of burn wounds is based on visual inspection of wound coloring, tissue necrosis, burn surface area, and edema. This subjective assessment makes it difficult to assess the severity of the wound and apply an adapted treatment. SFDI has been proven to improve the burn depth assessment [46].


**Figure III.4 – Commercially available SFDI devices [47,48].**

Although this technology provides objective quantitative imaging of physiological parameters, its implementation does not allow real-time imaging. Recent developments of SFDI introduced alternative approaches to achieve oxygenation imaging, but also structural and functional imaging in real-time, paving the way for its clinical translation to intraoperative use [49].

## III.4. Conclusion

Based on the fundamental principles of NIR optical imaging described in Chapter II, this chapter detailed the current use of exogenous and endogenous imaging technologies in the clinic. Commercially available

systems were presented along with their respective applications. However, encountered limitations restrain their impact on surgical guidance. Specifically, the subjectivity inherent to fluorescence imaging and the absence of real-time imaging capability for functional endogenous imaging greatly impact their suitability for intraoperative use. Limitations of these commercially available systems are further discussed in Chapter IV. For this standpoint, the objectives of this thesis work will be detailed.

**References**


[1] Takatani S.,Graham M.D., "Theoretical analysis of diffuse reflectance from a two-layer tissue model", IEEE Transactions on Biomedical Engineering, BME-26, pp. 656-664, (1987)

[2] van Veen R.L.P., H.J.C.M. Sterenborg H.J.C.M., Pifferi A., Torricelli A., Cubeddu R., ''Determination of VIS-NIR absorption coefficients of mammalian fat, with time- and spatially resolved diffuse reflectance and transmission spectroscopy'', OSA Annual BIOMED Topical Meeting, (2004)

[3] Hale G.M., Querry M.R., "Optical constants of water in the 200 nm to 200 micron wavelength region," Applied Optics, 12, pp. 555-563, (1973)

[4] Weed R.I.; Reed C.F., Berg G., "Is hemoglobin an essential structural component of human erythrocyte membranes?". Journal of Clinical Investigations, 42(4), pp. 581–88, (1963)

[5] Uludag K., Steinbrink J., Villringer A., Obrig H., "Separability and cross talk: optimizing dual wavelength combinations for near-infrared spectroscopy of the adult head," Neuroimage 22(2), 583–589 (2004)

[6] Yamashita Y., Maki A., Koizumi H., "Wavelength dependence of the precision of noninvasive optical measurement of oxy-, deoxy-, and total-hemoglobin concentration," Med. Phys. 28(6), 1108–1114 (2001).

[7] Gioux S., Mazhar A., Lee B.T., Lin S.J., Tobias A.M., Cuccia D.J., Stockdale A., Oketokoun R., Ashitate Y., Kelly E., Weinmann M., Durr N.J., Moffitt L.A., Durkin A.J., Tromberg B.J., Frangioni J.V., "First-in-human pilot study of a spatial frequency domain oxygenation imaging system", Journal of Biomedical Optics, 16(8), 086015, (2011)

[8] Mazhar A., Dell S., Cuccia D.J., Gioux S., Durkin A.J., Frangioni J.V., "Wavelength optimization for rapid chromophore mapping using spatial frequency domain imaging," Journal of Biomedical Optics, 15(6), 061716, (2010)

[9] Schmidt M., Aguénounon E., Nahas A., Torregrossa M., Tromberg B.J., Uhring W., Gioux S., "Real-time, wide-field, and quantitative oxygenation imaging using spatiotemporal modulation of light", Journal of Biomedical Optics, 24(7), 071610, (2019)

[10] Aguénounon E., Dadouche F., Uhring W., Gioux S., ''Real-time optical properties and oxygenation imaging using custom parallel processing in the spatial frequency domain'', Biomedical Optics Express, 10(8), pp. 3916-3928, (2019)

[11] Aguénounon E., Smith J.T., Al-Taher M., Diana M., Intes X., Sylvain Gioux S., "Real-time, wide-field and high-quality single snapshot imaging of optical properties with profile correction using deep learning", Biomedical Optics Express, 11(10), pp. 5701-5716, (2020)

[12] Jacques S.L., "Optical properties of biological tissues: a review," Physics in Medicine and Biology, 58, pp. R37-R61, (2013)

[13] Lee S., Mey L., Szymanska A.F., Takhar H.S., Cuccia D.J., Mazhar A., Yu K., ''SFDI biomarkers provide a quantitative ulcer risk metric and can be used to predict diabetic foot ulcer onset'', Journal of Diabetes and its Complications, 34(9), 107624, (2020)

[14] Tabassum S., Tank A., Wang F., Karrobi K., Vergato C., Bigio I.J., Waxman D.J., Roblyer D., ''Optical scattering as an early marker of apoptosis during chemotherapy and antiangiogenic therapy in murine models of prostate and breast cancer'', Neoplasia, 23(3), pp. 294-303, (2021)

[15] Ponticorvo A., Rowland R., Baldado M., Kennedy G.T., Hosking A.-M.Buremeister D.M., Christy R.J., Bernal N.P., Durkin A.J., ''Spatial Frequency Domain Imaging (SFDI) of clinical burns: A case report'', Burns Open, 4(2), pp. 67-71, (2020)

[16] van Manen L., Handgraaf H.J.M, Diana M., Dijkstra J., Ishiwaza T., Varhmeijer A.L., Mieog J.S.D., ''A practical guide for the use of indocyanine green and methylene blue in fluorescence-guided abdominal surgery'', Journal of Surgical Oncology, 118(2), pp. 283-300, (2018)

[17] Hernot S., van Manen L., Debie P., Mieog J.S.D., Vahrmeijer A.L., ''Latest developments in molecular tracers for fluorescence image-guided cancer surgery'', Lancet Oncology, 20(7), pp. 354-367, (2019)

[18] Galema H.A., Meijer R.P.J., Lauwerends L.J., Verhoef C., Burggraaf J., Vahrmeijer A.L., Hutteman M., Keereweer S., Hilling D.E., ''Fluorescence-guided surgery in colorectal cancer; A review on clinical results and future perspectives'', European Journal of Surgical Oncology, 0748-7983, (2021)

[19] Verbeek F.P., Troyan S.L., Mieog J.S., Liefers G.J., Moffitt L.A., Rosenberg M., Hirshfield-Bartek J., Gioux S., van de Velde C.J., Vahrmeijer A.L., Frangioni J.V., ''Near-infrared fluorescence sentinel lymph node mapping in breast cancer: a multicenter experience'', Breast Cancer Research and Treatment, 143(2), pp. 333-342, (2014)

[20] Van Der Vorst J.R., Schaafsma B.E., Hutteman M., Verbeek F.P.R., Liefers G.J., Hartgrink H.H., Smit V.T.BH.B.M., Löwik C.W.G.M., van de Velde C.J.H., Frangioni J.V., Vahrmeijer A.L., ''Near-infrared fluorescence-guided resection of colorectal liver metastases'', Cancer, 119(18), pp. 3411-3418, (2013)

[21] Verbeek F.P., van der Vorst J.R., Schaafsma B.E., Swijnenburg R.J., Gaarenstroom K.N., Elzevier H.W., van de Velde C.J., Frangioni J.V., Vahrmeijer A.L., ''Intraoperative near infrared fluorescence guided identification of the ureters using low dose methylene blue: a first in human experience'', Journal of Urology, 190, pp. 574-579, (2013)

[22] Barberio M., Al-Taher M., Felli E., Ashoka A.H., Marescaux J., Klymchenko A., Diana M., ''Intraoperative ureter identification with a novel fluorescent catheter'', Scientific Reports, 11, (2021)

[23] Van den Hoven P., Weller F.S., Van De Bent M., Goncalves L.N., Ruig M., Van Den Berg S.D., Ooms S., Mieog J.S.D., Van De Bogt K.E.A., van Schaik J., Schepers A., Vahrmeijer A.L., Hamming J.F., Van Der Vorst J.R., ''Near-infrared fluorescence imaging with indocyanine green for quantification of changes in tissue perfusion following revascularization'', Vascular, (2021)

[24] Goncalves L.N., van den Hoven P., van Schaik J., Leeuwenburgh L., Hendricks C.H.F., Verduijn P.S., van der Bogt K.E.A., van Rijswijk C.S.P., Schepers A., Vahrmeijer A.L., Hamming J.F., van der Vorst J.R., ''Perfusion Parameters in Near-Infrared Fluorescence Imaging with Indocyanine Green: A Systematic Review of the Literature'', Life, 11(5), (2021)

[25] Wang L.G., Barth C.W., Hitts C.H., Mebrat M.D., Montaño A.R., House B.J., McCoy M.E., Antaris A.L., Galvis S.N., McDowall I., Sorger J.M., Gibbs S.L., "Near-infrared nerve-binding fluorophores for buried nerve tissue imaging", Science Translational Medicine, 12(542), (2020)

[26] de Valk K.S., Deken M.M., Handgraaf H.J.M., Bhairosingh S.S., Bijlstra O.D., van Esdonk M.J., Terwisscha van Scheltinga A.G.T., Valentjin A.R.P.M., March T.L., Vuijk J., Peeters K.C.M.J., Holman F.A., Hiling D.E., Mieog J.S.D., Frangioni J.V., Burggraaf J., Vahrmeijer A.L., ''First-in-Human assessment of cRGD-zw800-1, a zwitterionic, integrin-targeted, near-infrared fluorescent peptide in colon carcinoma'', Clinical Cancer Research, 26(15), pp.3990-3998, (2020)

[27] Boogerd L.S.F., Hoogstins C.E.S., Schaap D.P., Kusters M., Handgraaf H.J.M., van der Valk M.J.M., Hiling D.E., Holman F.A., Peeters K.C.M.J., Mieog J.S.D., van de Velde C.J.H., Farina-Sarasqueta A., van Lijnschoten I., Framery B., Pèlegrin A., Gutowski M., Nienhuijs S.W., de Hingh I.H.J.T., Nieuwenhuijzen G.A.P., Rutten H.J.T, Cailler F., Burggraaf J., Vahrmeijer A.L., ''Safety and effectiveness of SGM-101, a fluorescent antibody targeting carcinoembryonic antigen, for intraoperative detection of colorectal cancer: a dose-escalation pilot study'', Lancet Gastroenterology & Hepatology, 3(3), pp. 181-191, (2018)

[28] de Jongh S.J., Tjalma J.J.J., Koller M., Linssen M.D., Vonk J., Dobosz M., Jorritsma-Smit A., Kleibeuker J.H., Hospers G.A.P., Havenga K., Hemmer P.H.J., Karrenbeld A., van Dam G.M., van Etten B., Nagengast W.B., ''Back-table fluorescence-guided imaging for circumferential resection margin evaluation using bevacizumab-800CW in patients with locally advanced rectal cancer'', Journal of Nuclear Medicine, 61(5), pp. 655-661, (2020)

[29] Voskuil F.J., Steinkamp P.J., Zhao T., van der Vegt B., Koller M., Doff J.J., Jayalakshmi Y., Hartung J.P., Gao J., Sumer B.D., Witjes M.J.H., van Dam G.M., SHINE study group, ''Exploiting metabolic acidosis in solid cancers using a tumor-agnostic pHactivatable nanoprobe for fluorescence-guided surgery'', Nature Communications, 11(1), (2020)

[30] Mieog J.S.D., Achterberg F.B., Zlitni A., Hutteman M., Burggraaf J., Swijnenburg R.J., Gioux S., Vahrmeijer A.L., ''Fundamentals and developments in fluorescence-guided cancer surgery'', Nature Reviews Clinical Oncology, 19(1), (2022)

[31] Sajedi S., Sabet H., Choi H.S., "Intraoperative biophotonic imaging systems for image-guided interventions", Nanophotonics, 8(1), pp. 99-116, (2019)

[32] Zhu B., Sevick-Muraca E.M., ''A review of performance of near-infrared fluorescence imaging devices used in clinical studies'', The British Journal of Radiology, 88(1045), (2015)

[33] Dsouza A.V., Lin H., Henderson E.R., Samkoe K.S., Pogue B.W., "Review of fluorescence guided surgery systems: identification of key performance capabilities beyond indocyanine green imaging", Journal of Biomedical Optics, 21(8), 080901, (2016)

[34] Elliott J.T., Dsouza A.V., Davis S.C., Olson J.D., Paulsen K.D., Roberts D.W., Pogue B.W., "Review of fluorescence guided surgery visualization and overlay techniques", Biomedical Optics Express, 6, pp. 3765-3782, (2015)

[35] https://www.stryker.com/us/en/endoscopy/products/spy-elite.html (accessed 15.02.2022)

[36] https://www.medtronic.com/covidien/en-gb/products/visualization-solutions/elevision-ir-platform.html (accessed 15.02.2022)

[37] https://surgicalone.com/item/hamamatsu-pde-neo/ (accessed 15.02.2022)

[38] https://fluoptics.com/fluobeam/ (accessed 15.02.2022)

[39] https://www.karlstorz.com/de/en/highlights-micro.htm (accessed 15.02.2022)

[40] Barberio M., Benedicenti S., Pizzicannella M., Felli E., Collins T., Jansen-Winkeln B., Marescaux J., Viola M.G., Diana M., ''Intraoperative Guidance Using Hyperspectral Imaging: A Review for Surgeons'', Diagnostics, 11(11), 2066, (2021)

[41] Jansen-Winkeln B., Maktabi M., Takoh J.P., Rabe S.M., Barberio M., Köhler H., Neumuth T., Melzer A., Chalopin C., Gockel I., ''Hyperspektral-Imaging bei gastrointestinalen Anastomosen [Hyperspectral imaging of gastrointestinal anastomoses]'', Der Chirurg, 89(9), pp. 717-725, (2018)

[42] Mehdorn M., Köhler H., Rabe S.M., Niebisch S., Lyros O., Chalopin C., Gockel I., Jansen-Winkeln B., ''Hyperspectral imaging (HSI) in acute mesenteric ischemia to detect intestinal perfusion deficits'', Journal of Surgical Research, 254, pp. 7-15, (2020)

[43] Sucher R., Athanasios A., Köhler H., Wagner T., Brunotte M., Lederer A., Gockel I., Seehofer D., ''Hyperspectral Imaging (HSI) in anatomic left liver resection'', International Journal of Surgery Case Reports, 62, pp. 108-111, (2019)

[44] Weinkauf C., Mazhar A., Vaishnav K., Hamadani A.A., Cuccia D.J., Armstrong D.G., ''Near-instant noninvasive optical imaging of tissue perfusion for vascular assessment'', Journal of Vascular Surgery, 69(2), pp. 555-562, (2019)

[45] Nguyen J.T., Lin S.J., Tobias A.M., Gioux S., Mazhar A., Cuccia D.J., Ashitate Y., Stockdale A., Oketokoun R., Durr N.J., Moffitt L.A., Durkin A.J., Tromberg B.J., Frangioni J.V., Lee B.T., ''A novel pilot study using spatial frequency domain imaging to assess oxygenation of perforator flaps during reconstructive breast surgery'', Annals of plastic surgery, 71(3), pp. 308–315, (2013)

[46] Ponticorvo A., Rowland R., Baldado, M., Kennedy G. T., Hosking A. M., Burmeister D. M., Christy R. J., Bernal N. P., Durkin A. J., ''Spatial Frequency Domain Imaging (SFDI) of clinical burns: A case report'', Burns Open, 4(2), pp. 67-71, (2020)

[47] https://modulim.com/clarifi/ (accessed 15.02.2022)

[48] https://modulim.com/technology/research-applications/ (accessed 15.02.2022)

[49] Gioux S., Mazhar A., Cuccia D.J., "Spatial frequency domain imaging in 2019: principles, applications, and perspectives", Journal of Biomedical Optics, 24(7), 071613, (2019)

# IV. Doctoral work objectives

The previous chapters offered an overview of current medical imaging technologies deployed at the service of surgeons, with a focus on the intraoperative phase of the patient's surgical journey. Considering the respective strengths and weaknesses of conventional imaging technologies, near-infrared optical imaging was identified as a promising candidate for providing guidance through surgical acts. After covering the basics of topical light-matter interaction and light propagation modeling in biological tissues, advanced NIR optical imaging technologies were presented. Their relevance for specific clinical applications were demonstrated along with related commercially available imaging devices. Although part of them is currently involved in routine clinical care, these imaging technologies suffer from critical limitations, representing as many obstacles in their way of being adopted as standard of care. This chapter reports these limitations and presents the work axes and objectives of this thesis work.

## IV.1. Overall objective

The end goal of this project is to bring the latest suitable imaging modalities for tissue status assessment to the clinic. To this purpose, a first objective is the development of a clinically-compatible imaging platform. This device should be capable of widefield, high quality, real-time imaging of tissue oxygenation parameters implementing the latest advances in SFDI. In addition, the imaging system design should be compatible with fluorescence imaging in order to provide validation of oxygenation imaging against blood perfusion assessment with fluorescence angiography. Validation of the capabilities and performances of this imaging platform is expected in multiple scenarii of preclinical trials, paving the way to its clinical translation. A second objective is the demonstration of the combination of endogenous and exogenous imaging to produce widefield, high quality, quantitative fluorescence imaging using the multimodality of the platform. Fluorescence quantification is expected to enhance tumor margin assessment and resection procedures by providing objective visualization. Validation is expected through preclinical trials.

## IV.2. Limitations of standards of care

The motivation for this work stems from the limitations of the current standards of care. The management of diseases and surgical procedures is often reported to be inconsistent, because of a lack of consensus-

driven clinical data. Besides the lack of performing tools for intraprocedural guidance, the subjectivity of existing solutions impacts the navigation and decision-making through surgical acts.

Blood perfusion is a longstanding issue that still suffers from unmet clinical needs. The ability to assess macro and microcirculation together with oxygen delivery yields tissue viability assessment or organ function monitoring. However, perfusion assessment is mostly based on visual inspection, empirical indices and contrast estimations. A non-exhaustive list of such inputs include:

- Visual inspection

A disturbed blood perfusion in tissue can be detected by eye, judging by the discoloration of tissues. Since oxygenated and deoxygenated hemoglobin feature significant absorption in the visible range resulting in coloring the tissues, it is possible to locate and analyze blood perfusion perturbation in surface tissues. For instance, patches pattern of discoloration of the skin – or skin mottling – has been described in the case of decreased peripheral hypoperfusion [1].

- Clinical metrics

Perfusion indices based on clinical evaluation and biomarker measurements may be used as indicators. A large number of indices have been derived to categorize perfusion disorders [2]. Lactate is the most frequently monitored biomarker for this application [3]. Its concentration reflects cellular hypoxia, that may be linked to ischemia. In particular, local capillary lactates represent the tissue microcirculation state. However, this approach requires blood sampling and available blood gas analysis, producing a one-time one-location measurement.

Capillary refill time is a widely employed metric to rapidly assess capillary blood flow [4]. It represents the time for tissues coloration to return the baseline after application of blanching pressure. Typically ranging from 2 to 5 seconds, it provides a rule of thumbs for perfusion investigation.

$StO_2$ represents the hemoglobin oxygen saturation in tissue and can be used as an indicator of hypoperfusion and hypoxia. Currently, point-measurement devices using NIR spectroscopy can deliver $StO_2$ assessment [3].

- Contrast imaging

Blood flow imaging by taking advantage of red blood cells light scattering. Two similar technologies exist, producing real-time imaging of blood flow. Laser Doppler flowmetry measures the Doppler shift induced by the blood cell moving speed. Although useful for revascularization monitoring applications, it is limited by its small field of view and strongly impacted by the presence of heterogeneities in the tissues [5]. Laser speckle imaging is an alternative implementation with larger field of view but providing contrast measurements only [6].

Differently, NIR fluorescence angiography can be employed to monitor blood perfusion in real-time over large areas. However, the qualitative assessment inherent to fluorescence images introduces subjectivity bias in the decision-making.

NIR fluorescence imaging along with the development of new targeted agents also represented a breakthrough for tumor resection procedures. The ongoing clinical translation of such novel tracers could initiate a paradigm shift in cancer surgery standards of care. However, the same qualitative assessment on fluorescence contrast can lead to uncomplete resections. Moreover, varying tissue optical properties across tissues induce fluorescence distortions, introducing additional bias in the images assessment. Multiple correction algorithms have been proposed, mostly demonstrated to the case of single point probes [7].

## IV.3. Work axis 1: Novel imaging system development

There is currently no existing imaging system capable of performing real-time widefield oxygenation and fluorescence imaging. Thus, the first set of objectives of this work is the design, implementation and testing of such an imaging system. The system architecture will be based on previously described systems for similar clinical applications. Hence, the device should feature one visible channel dedicated to anatomical imaging and two NIR channels for widefield endogenous and exogenous imaging, including assorted multi-camera detection and illumination systems. A cart-based embodiment of the platform would allow a modular implementation, and ergonomic use. Instrumentation control, data processing and output visualization should be managed by a computer integrated to the device.

First *in-vitro* tests and following *in-vivo* preclinical trials will demonstrate the performances of the device, featuring the latest SFDI developments for real-time oxygenation parameters extraction but also fluorescence imaging. The validation by comparison with conventional methods will be a first step in the clinical translation of the device, proving its added value for blood perfusion assessment.

Clinical translation is a very demanding, labor-intensive and time-consuming process. Introduction to this process and guidelines specific to the case of NIR imaging have been previously proposed [8]. Fortunately, several advantages alleviate constraints in the case of this device: the imaging platform is used for observational purposes and not for diagnosis or treatment; no contact with the patient is needed; the use of selected contrast agents has already been approved for the specific same clinical applications.

## IV.4. Work axis 2: Blood perfusion assessment for ischemia monitoring

If the suitability of SFDI for blood perfusion assessment and the feasibility of implementing SFDI-based oxygenation imaging in real-time have been demonstrated, the latest available technologies have not been tested in preclinical trials yet. The ad-hoc design of the developed platform enables the use of state-of-the-art SFDI technology in a clinical environment, yielding widefield, high-quality oxygenation imaging in real-time. Preclinical trials with large animal models are expected to validate the performances of the imaging system by confronting its outcomes to standard perfusion assessment methods. To this purpose, ischemia models have been designed in various organs of the abdomen. $StO_2$ rates extracted from the images are expected to correlate with fluorescence angiography, lactate concentrations, blood gas analysis and histopathological scores, confirming the ischemia detection and quantification by SFDI. Moreover, the real-time capability of the imaging system should exhibit the dynamics of the ischemia.

## IV.5. Work axis 3: Tumor detection and margin assessment for cancer surgery

In the case of fluorescence-assisted tumor resection procedures, margin detection is based on a qualitative analysis of contrast images. A misinterpretation of this contrast could lead to an incomplete resection, or inversely to excessive removal of healthy tissue. The quantification of the presence of tumor tissue can consequently be key to finding a golden mean. While fluorescence quantification models have been derived and applied to single-point probes, there are few reported translations of these methods to widefield imaging, and none feature a clinically-compatible implementation for macroscopic imaging using SFDI [9]. The implementation of such quantitative fluorescence imaging on the developed imaging platform will be assessed through preclinical trials. The fluorescence quantification is expected to produce a more accurate representation of the tumor tracer distribution, thus improving the interpretation of fluorescence images.

## IV.6. Conclusion

Next chapters of this manuscript will detail the contributions related to the different work axes described in the previous sections. The development of a novel imaging platform as described in section 3 is described in Chapter V. Application to blood perfusion assessment in ischemic small bowel and stomach are presented respectively in Chapter VI and VII. A pilot study for the use of quantified fluorescence for tumor detection and margin assessment is detailed in Chapter VIII. Finally, a conclusion chapter summarizes this work and elaborates perspectives for future works.

**References**

[1] Lima A., Takala J., ‘’Clinical significance of monitoring perfusion in non-vital organs’’, Intensive Care Medicine, 40(7), pp. 1052-1054, (2014)

[2] Hasanin A., Mukhtar A., Nassar H., ‘’Perfusion indices revisited’’, Journal of Intensive Care, 5(24), (2017)

[3] Mayer K., Trzeciak S., Puri N.K., ‘’Assessment of the adequacy of oxygen delivery’’, Current Opinion in Critical Care, 22, pp. 437-443, (2016)

[4] Ait-Oufella H., Bakker J., ‘’Understanding clinical signs of poor tissue perfusion during septic shock’’, Intensive Care Medicine, 42(12), pp. 2070-2072, (2016)

[5] Fredriksson I., Larsson M., Strömberg T., ‘’Measurement depth and volume in laser Doppler flowmetry’’, Microvascular Research, 78(1), pp. 4-13, (2009)

[6] Hultman M., Fredriksson I., Larsson M., Alvandpour A., Strömberg T., ‘’A 15.6 frames per second 1-megapixel multiple exposure laser speckle contrast imaging setup’’, Journal of Biophotonics, 11(2), (2018)

[7] Bradley R.S., Thorniley M.S., “A review of attenuation correction techniques for tissue fluorescence”, Journal of the Royal Society Interface, 3(6), pp. 1–13, (2006)

[8] Gioux S., Choi H.S., Frangioni J.V., ‘’Image-Guided Surgery Using Invisible Near-Infrared Light: Fundamentals of Clinical Translation’’, Molecular Imaging, (2010)

[9] Valdes P.A., Juvekar P., Agar N.Y.R., Gioux S. Golby A.J., ‘’Quantitative Wide-Field Imaging Techniques for Fluorescence Guided Neurosurgery’’, Frontiers in Surgery, 6(31), (2019)

# V. Novel multimodal imaging platform for intraoperative blood perfusion assessment

This chapter describes the main contribution of this doctoral work. Currently, there are no available devices capable of real-time widefield oxygenation imaging for intraoperative use in open-surgery. Recent development in the field of NIR imaging for tissue oxygenation monitoring demonstrated the ability to measure hemoglobin concentration within tissues over large areas, providing a reliable objective metric of tissue viability for a variety of surgical procedures. State-of-the-art implementations showed the ability to perform oxygenation imaging in real-time, making this technology well-suited for intraoperative use. Yet, the implementation of these advances in a clinically-compatible device and preclinical validation were required.

A novel multimodal imaging platform for intraoperative blood perfusion assessment is presented in this chapter. Its design, characterization and validation are detailed. This imaging device is capable of high-quality, widefield oxygenation imaging in real-time as part of the surgical workflow for blood perfusion assessment. By design, it is also capable of NIR fluorescence imaging for direct comparison of current imaging standards with state-of-the-art oxygenation imaging. The underlying technology is first detailed. Second, the imaging platform is described, with a focus on each subsystem. *In-vitro* characterization results are showed for optical properties imaging and fluorescence imaging. Finally, the validation of the imaging system for *in-vivo* use in a preclinical trial is detailed.

## V.1. Context and motivation

The capabilities of NIR imaging greatly expanded over the past few years, providing feedback for tissue status assessment during surgery, and particularly blood perfusion assessment. The development of fluorescence imaging for clinical applications accelerated with the growing number of available contrast agents and the development of new imaging technologies [1-3]. However, the lack of quantitative capabilities leads to subjective assessment of fluorescence images, introducing variability in the surgical outcome. Alternatively, the ability of hyperspectral imaging to extract functional parameters for clinical applications has been reported [4-6]. Yet, it suffers from the lack of quantitative extraction of tissue constituents concentrations, and cannot provide real-time feedback intraoperatively.

The development of SFDI enabled the quantitative extraction of hemoglobin concentrations, and in turn the imaging of tissue oxygenation over large fields of view (> 100 $cm^2$) [7]. Recent development in the real-time implementation of SFDI – namely SSOP – described dedicated acquisition and processing workflows, and the use of parallel computing to provide real-time imaging capabilities to the technique [8]. With the

most advanced form of SSOP including deep learning-based processing, high-quality images can be produced while preserving the real-time capabilities of the method [9].

There is currently no available tool capable of quantitative imaging of hemoglobin concentrations for blood perfusion assessment in clinical settings. Based on previously described imaging systems for NIR fluorescence and SFDI-based oxygenation imaging, a novel imaging platform integrating the latest SSOP developments for producing real-time oxygenation imaging is proposed [7,10,11]. In addition, the described platform is capable of performing NIR fluorescence imaging. This imaging modality being considered cutting-edge standard of care for perfusion assessment, the ability to perform both oxygenation and fluorescence imaging with the same device facilitates their comparison.

The system design is first detailed, with a description of each subsystem being part of the platform. Next, *in-vitro* characterization is presented, showing the performances of the devices for optical properties imaging and fluorescence detection. Finally, *in-vivo* validation demonstrates the ability of the imaging platform to dynamically detect ischemia in the small bowel by measuring tissue oxygenation in real-time.

## V.2. Materials and methods

### V.2.1. Oxygenation imaging

Spatial frequency domain imaging is a technique using structured light illumination and detection of diffusely back reflected light to optically characterize a sample [12]. Images are acquired while projecting sinusoidal patterns with several spatial frequencies, repeated for multiple phase shifts. Typically, a total of six patterns are employed: three 120° phase-shifted patterns at a 0 $mm^{-1}$ spatial frequency (or CW patterns) and at a non-zero high frequency. The data demodulation yields the modulation amplitude for both frequencied, also referred to as DC and AC components. A calibration step involving a sample with known optical properties produces diffuse reflectance maps of the sample from the DC and AC extracted components. Finally, an inverse solver enables the decoupling of the absorption and scattering contributions to the recorded reflectance of the sample, yielding quantified mapping of the absorption coefficient $\mu_a$ and reduced scattering coefficient $\mu_s$'.

Alternatively, Single Snapshot of Optical Properties (SSOP) imaging relies on a single high spatial frequency frame, making its acquisition process compatible with real-time imaging [13]. This particular implementation of SFDI differs in its demodulation step, performed by filtering in the Fourier space. Optimized filtering has been designed to reduce the inherent image degradation, and parallel computing has been employed to demonstrate real-time optical properties imaging using SSOP [8]. In order to further

reduce remaining artifacts, a deep learning-based approach has been developed for the demodulation [9]. Moreover, this approach integrates tridimensional profilometry, yielding high-quality profile-corrected optical properties maps in real-time [9,14].

According to this method, two distinct convolutional neural networks (CNN) based on a U-Net architecture were established for data demodulation and profilometry purposes in the imaging workflow. The networks were trained based on high-quality imaged obtained from 7 phase-SFDI acquisition sequences. A total of 200 datasets were acquired: 40 images of tissue-mimicking phantoms with optical properties ranging from $\mu_a$ = 0.005 $mm^{-1}$ to 0.05 $mm^{-1}$ and $\mu_s'$ = 0.005 $mm^{-1}$ to 0.05 $mm^{-1}$; 52 *in*-vivo images of hands from healthy volunteers – Caucasian men and women – placed in various geometrical settings; 108 *ex-vivo* and *in-vivo* images of swine organs across the abdomen (stomach, small bowel, colon, kidney, pancreas, liver and spleen). This way, the imaging platform is equipped to extract optical properties maps with spatial resolution of 1 megapixel in real-time. From the absorption maps acquired at several wavelengths, chromophore concentrations such as oxyhemoglobin and deoxyhemoglobin can be measured by inverting Beer's law. Consequently, the oxygen saturation rate can be mapped.

### V.2.2. System design

This section describes the imaging platform design by presenting each subsystem. An overview of the complete system is given in **Figure V.1**. This medical cart-based platform features a three channel-imaging head, fiber-coupled white light sources and laser sources, and a workstation.

#### V.2.2.1. Cart and arm

The platform is built upon a customized medical cart (Symbio cart, ITD, Neubiberg, Germany). This wheeled base is equipped with an isolation transformer to regulate power supply to the device and counterweights to safely balance the assembly. Two articulated arms bear display screens both for the surgeons and the operator. A third articulated arm (Elite 5220, ICW, Medford, OR, USA) is fixed to the central column to accommodate the imaging head. Its large reach enables a user to operate the system while keeping away from the sterile field. Cables can be guided from the devices through the central column. Inside is placed a 24V AC/DC converter (AKM90PS24, XP Power, Singapore) to provide power supply to the imaging head. The articulated arms conveniently fold for storage. The wide castors and large handle provide good mobility when deploying or rolling out the platform.

### V.2.2.2. Imaging head

The imaging head is depicted in **Figure V.1**. This three channel-optical system features one visible light channel (VIS) and two NIR channels (NIR1, NIR2). These channels are co-registered using a custom optomechanical device equipped with tilting mirrors, producing a field of view of 12 cm x 15 cm. The detection optics enable fine focusing and individual aperture control. An RGB camera (GO-5000C-USB, JAI Ltd., Kanagawa, Japan) and two monochrome cameras (GO-5000M-USB, JAI Ltd., Kanagawa, Japan; Edge 4.2, Excelitas PCO GmbH, Kelheim, Germany) are used for the detection in the VIS, NIR1 and NIR2 channels. Custom filter sets (Chroma Inc., Bellows Falls, VT, USA) provide wavebands selection for optical properties imaging with minimized crosstalk between channels.

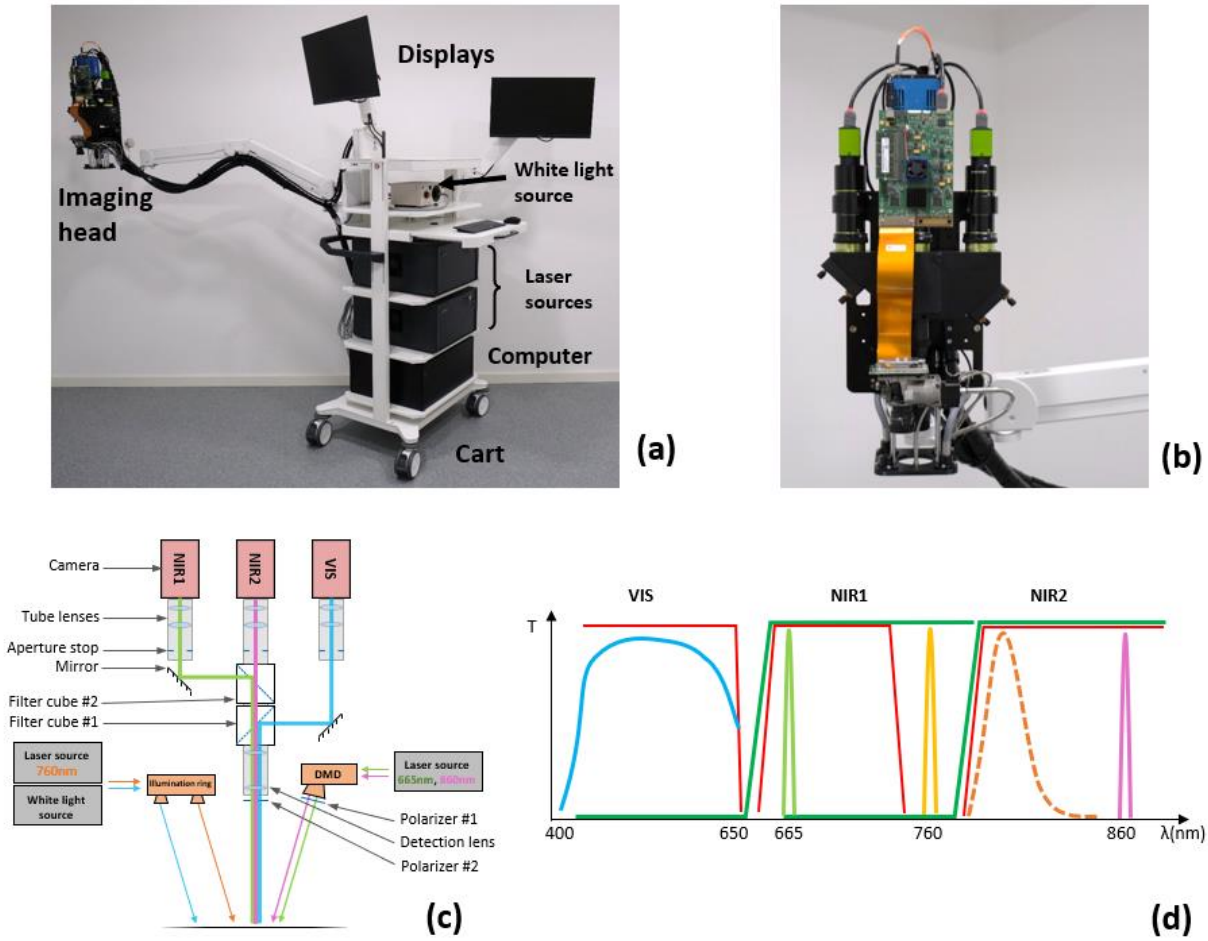


**Figure V.1 – Multimodal imaging platform architecture. The platform is built onto a medical cart equipped with light sources, a computer, mounted displays and a mounted imaging head (a). The imaging head is composed of an optomechanical device offering three imaging channels: VIS, NIR1 and NIR2; and illumination systems for oxygenation imaging, fluorescence imaging and white light illumination of the surgical field (b), (c). The detection optical filtering is adapted to reflectance imaging at 665 nm and 860nm, and fluorescence imaging using 800 nm dyes (d).**

A projector based on a digital micromirror device (V7000 HiSpeed, Vialux GmbH, Chemnitz, Germany) equipped with a custom fiber coupling adapter enables the projection of structured light at a 45 cm working distance for optical properties imaging. The imaging head also integrates an illumination ring to accommodate fibers for bright white light illumination of the surgical field, or laser illumination for fluorescence excitation. Linear polarizers (RCV8N2EC, Moxtek, Orem, UT, USA) are cross-polarized in front on the projection and detection paths to reject specular reflections.

One 5V DC/DC converter (PYB30-Q24-S5-U, CUI Inc., Tualatin, OR, USA) provides power supply to the DMD board. A 24V model (TDMC40-2415, Traco Power, Baar, Switzerland) powers the NIR2 camera. The VIS and NIR1 channel cameras are powered by USB cable.

### V.2.2.3. White light source & illumination

Two LED-based lamps (LO-35, Fiberoptics Technologies Inc., Pomfret, CT, USA) with custom 650 nm short-pass filters and fiber bundles provide a bright illumination of the surgical field. Though the LEDs emit low amounts of infrared light, the additional filter ensures an optimal visible illumination while preserving the NIR channels from background noise. The two fiber bundles split in two outputs each to produce a multi-angle illumination from the imaging head over a large area – over 50 cm diameter at a 45 cm working distance.

### V.2.2.4. Laser source

Custom laser sources were designed to equip the platform. A first source is dedicated to the DMD projector illumination to collect reflectance data for optical properties imaging while an adapted replica of it is dedicated to fluorescence imaging. The two sources are referred to as reflectance source and fluorescence source, respectively to their purpose. **Figure V.2** presents one complete source.

Such a source houses six independent modules that can be loaded with different laser diodes (LDX Optronics, Maryville, TN, USA) to achieve multispectral imaging, or to match the excitation of fluorophores of interest. Identical laser diodes can also be combined to provide higher illumination power. For optimized oxygenation imaging, a combination of four 665 nm (2 W each) and two 860 nm (5 W each) laser diodes equip the reflectance source. In order to excite 800 nm fluorophores – especially ICG – six 760 nm, (6 W each) laser diodes are mounted in the fluorescence source.

Each diode is thermally regulated by a thermoelectric cooler (TEC) (TEC-15.4-3.9-33.4-72-40-CH4,7, Arctic TEC Technologies, Dortmund, Germany) and a thermistor placed on the laser diode chassis (TH10K,

Thorlabs, Newton, NJ, USA). Individual TEC drivers (PTC5K-CH, Wavelength electronics, Bozeman, MT, USA) enable temperature regulation and monitoring of the diodes. Similarly, laser diode drivers (LD10CHA, wavelength electronics, Bozeman, MT, USA) control the laser output power, and monitoring of the integrated photodiode feedback. A custom optomechanical assembly featuring optical filters (Chroma Inc., Bellows Falls, VT, USA) and graded-index lenses (Newport, Irvine, CA, USA) performs the laser output coupling into a dedicated fiber bundle (CeramOptec, Bonn, Germany). In the case of the reflectance source, the modules are coupled into a 6-legged fiber bundle which regroup in a single output for illuminating the DMD. In the fluorescence source, the 6 legs of the bundle contain multiple fibers which are randomized and redistributed into 6 legs that are plugged in the illumination ring. In addition, each module is interfaced with USB analog input/ouput modules (USB-202, Measurement Computing, Norton, MA, USA) to control the modules and record feedback signals from a computer. The interfacing of a single module is depicted in **Figure V.2**.

In order to dissipate the great amounts of heat generated by the laser diode cooling and different drivers, all the heating modules components are mounted on a tunnel heatsink equipped will push-pull fans. This design produces a compact assembly and while limiting noise due to the limited number of fans and their large diameter.

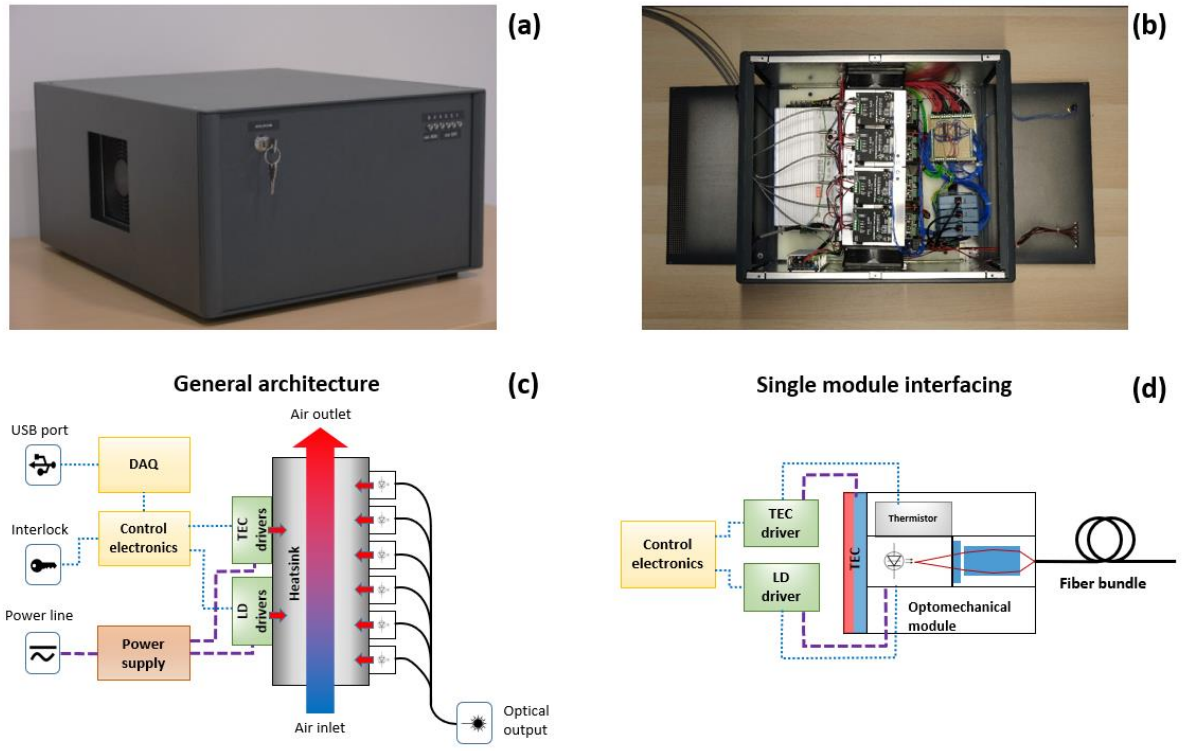


**Figure V.2 – Modular and controllable laser source. The sources are designed to sit on the cart shelves. On its front face an interlock system enables the optical output while status LED exhibit the lasers state (a). The 6 modules are placed around a heat sink providing heat dissipation while optimizing space (b,c). The modules are interfaced with USB modules for remote control of the sources (d).**

#### V.2.2.5. Computer

A high-performance computer has been assembled to achieve the imaging device control, data processing, data storage management and visualization. A CameraLink HS frame grabber (ME5 Marathon AF2, Silicon Software, Mannheim, Germany) and an additional USB3.0 controller ensure the communication with the imaging head. Powerful CPU (Intel Core i5-10600K, Intel, Santa Clara, CA, USA) and GPU (Quadro RTX 4000, NVIDIA, Santa Clara, CA, USA) and 64 GB of high-speed RAM can perform intensive data processing and visualization on multiple displays. Finally, 5 TB of fast SSD storage are installed for data stream management of 1 GB/s.

### V.2.3. System characterization

#### V.2.3.1. Optical characterization

A USAF1951 resolution chart (RES-2, Newport, Irvine, CA, USA) was placed under the imaging head at 45 cm working distance and imaged with each channel: VIS, NIR1 and NIR2.

Optical properties extraction was characterized by imaging an array of 12 tissue-mimicking phantoms of 6x6x2.5 cm. These cured silicone-base samples were fabricated using varying amounts of alcohol-soluble nigrosine and Titanium dioxide ($TiO_2$) to tune the absorption and scattering of the material, respectively, spanning a large range of optical properties to be measured: $\mu_a$ ranging from 0.013 to 0.08 $mm^{-1}$ and $\mu_s$' ranging from 0.75 to 1.8 $mm^{-1}$ at 665nm. These samples were imaged at 665 nm and 860 nm under a 0.2 $mm^{-1}$ spatial frequency illumination, and processed using the deep learning-based implementation of SSOP. The measurements were compared to those obtained with a benchtop imaging system using 7 phase-SFDI.

#### V.2.3.2. Illumination characterization

Peak fluence rates were measured at 45 cm working distance in the center of the field of view using a digital handheld power meter (PM100D, Thorlabs, Newton, NJ, USA) at 665 nm and 860 nm while projecting a continuous wave pattern, and at 760 nm by fiber illumination

#### V.2.3.3. Noise and sensitivity performances

In order to quantify the background noise in the fluorescence images, the contributions from dark noise and both white light and excitation light leakage were measured. Two different background materials were placed at 45 cm from the imaging head: a large tissue-mimicking phantom with $\mu_a$ = 0.012 $mm^{-1}$ and $\mu_s'$ = 1.08 $mm^{-1}$ at 665nm and a sheet of white paper. Images from the NIR2 channel were acquired with varying exposure settings – exposure time, sensor binning – with successively all lights switched off, and white light and excitation laser light switched on.

Finally, the sensitivity of the NIR2 channel for fluorescence detection was assessed by imaging eight different dilutions of ICG diluted in dimethyl sulfoxide (DMSO) at concentrations ranging from 25 nM/L up to 800 nM/L. The vials were placed onto the previously mentioned background materials and imaged with varying exposure settings. Average fluorescence signals were extracted and compared to the noise floor level for sensitivity assessment. Sensitivity was defined as the concentration producing an intensity twice as high as the noise floor level.

### V.2.4. *In-vivo* ischemic small bowel imaging

#### V.2.4.1. Bowel ischemia model

One large swine was involved in this non-survival study, which received full approval from the local Ethical Committee on Animal Experimentation (ICOMETH No. 038.2019.01.121) and by the French Ministry of Superior Education and Research (MESR) under the following reference: APAFIS #20819-2019052411591088 v3. After performing a midline laparotomy, a 20 cm small bowel loop was exposed. A central region was delineated, and corresponding arcade branches were isolated. A clamp was used to create an occlusion on these vessels, causing ischemia on a limited portion of the bowel while the rest of the loop remained perfused. The occlusion was maintained during 14 minutes until release.

#### V.2.4.2. Fluorescence imaging

A dose of ICG was injected intravenously 2 minutes before occlusion release. Color images from the VIS channel and fluorescence images from the NIR2 channel were acquired starting from the injection timepoint and for 2 minutes and 30 seconds. The imaging working distance was maintained at 45 cm. Fluorescence excitation was produced using 760 nm laser light.

#### V.2.4.3. Oxygenation imaging

A sinusoidal pattern with spatial frequency of 0.2 $mm^{-1}$ was projected at both 665 nm and 860 nm wavelengths using the DMD projector. Reflectance images from the NIR1 and NIR2 channels were acquired, as well as color images from the VIS channel for anatomical reference. Images were recorded starting 2 minutes before occlusion to establish the oxygen saturation baseline, and during 12 minutes after occlusion. After performing fluorescence imaging, oxygenation imaging resumed to record for 3 minutes during the end of the reperfusion phase.

## V.3. Results

### V.3.1. System characterization

#### V.3.1.1. Optical characterization

At 45 cm working distance and performing 2x2 binning on the camera sensor, the optical system produces images of a 12x15 cm field-of-view, with a resolution of 1024x1280 pixels. The measured lateral resolution with fully open apertures for channels VIS and NIR2 was 5.04 lp/mm and 5.66 lp/mm for the NIR1 channel.

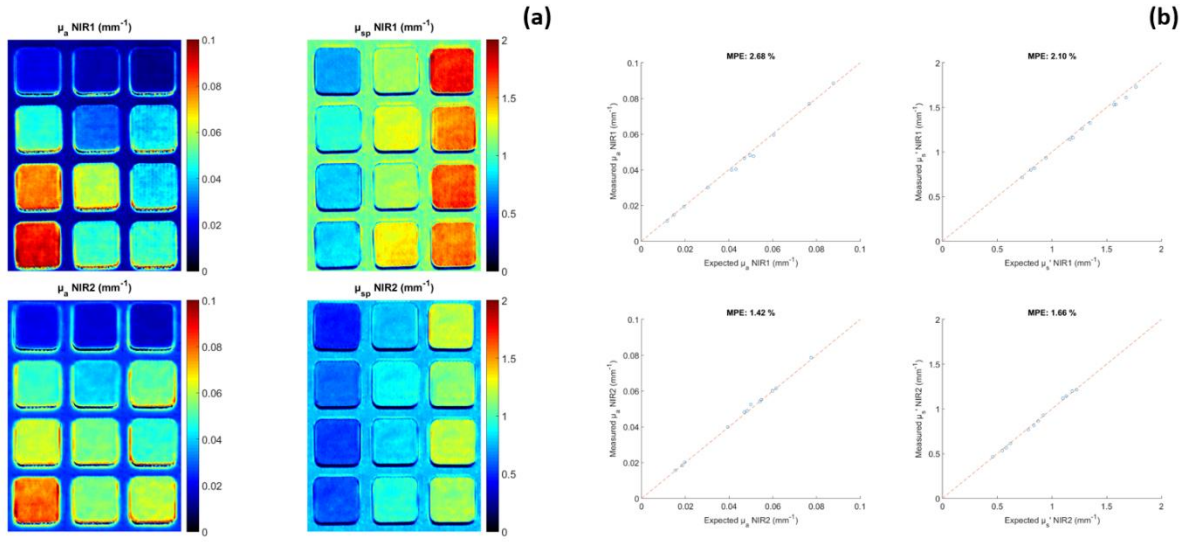


**Figure V.3 – *In-vitro* optical properties imaging characterization. A matrix of 12 phantoms was imaged using a deep learning-based approached. Absorption and reduced scattering maps at 665 nm and 860 nm obtained from respectively the channels NIR1 and NIR2 show good image quality with few artifacts (a). The measured**

**optical properties are in agreement with standard SFDI, showing mean error percentages below 2.7 % for absorption and 1.7 % for reduced scattering.**

A set of 12 tissue-mimicking phantoms was imaged first with a benchtop imaging system using 7 phase-SFDI as reference. The images produced by the clinical platform were processed using deep learning-based SSOP. High image quality and good accuracy with respect to optical properties extraction were achieved. **Figure V.3** presents the extracted optical properties maps and error estimation in comparison to standard SFDI. Errors in $\mu_a$ and $\mu_s'$ measurements were respectively below 2.7 % and 2.7 % for both 665 nm and 860 nm oxygenation imaging wavelengths.

### V.3.1.2. Illumination characterization

A continuous-wave illumination was produced using the DMD at both 665 nm and 860 nm oxygenation imaging wavelengths. At 45 cm working distance, a power meter probe was placed in the center of the field-of-view. Fluence rates of 0.93 mW/cm² at 665 nm and 1.51 mW/cm² at 860 nm were measured. The fluorescence excitation field at 760 nm showed a peak fluence rate of 31.51 mW/cm².

### V.3.1.3. Noise and sensitivity performances

Background noise in the NIR2 channel was measured using successively a tissue-mimicking phantom and a sheet of white paper placed at 45 cm working distance. **Figure V.4** shows the evolution of dark noise and leakage with exposure settings and background materials. Dark noise was first measured with exposure times ranging from 5 ms to 160 ms and sensor binning factors of 1x1, 2x2 and 4x4. Noise levels representing 0.1 %, 0.6 % and 2.4 % of the dynamic range of the NIR2 camera were measured respectively with 1x1, 2x2 and 4x4 binning factors. The same set of images was acquired with fully open aperture, and both with light and 760 nm laser excitation light switched on. Noise levels were on average 17 % and 46 % higher than the dark noise using a phantom background or a paper background, corresponding mostly to excitation light leakage into the NIR2 channel.

A set of 8 ICG dilutions with concentrations ranging from 25 nM/L to 800 nM/L was imaged in the same previously stated conditions. **Figure V.4** shows the images from the VIS and NIR2 channels as well as an overlay. **Figure V.4** also shows the evolution of intensity in the NIR2 images for each dilution at various exposure times with fixed 2x2 sensor binning and using a silicone phantom as background. The intensity increases linearly with the exposure time until reaching saturation. Sensitivity was estimated by measuring the concentration corresponding to an intensity 2 times higher than the noise floor level, yielding a signal-

to-background ratio of 2. At 40 ms exposure time and 2x2 binning factor, the sensitivity was estimated at 18.8 nM/L.

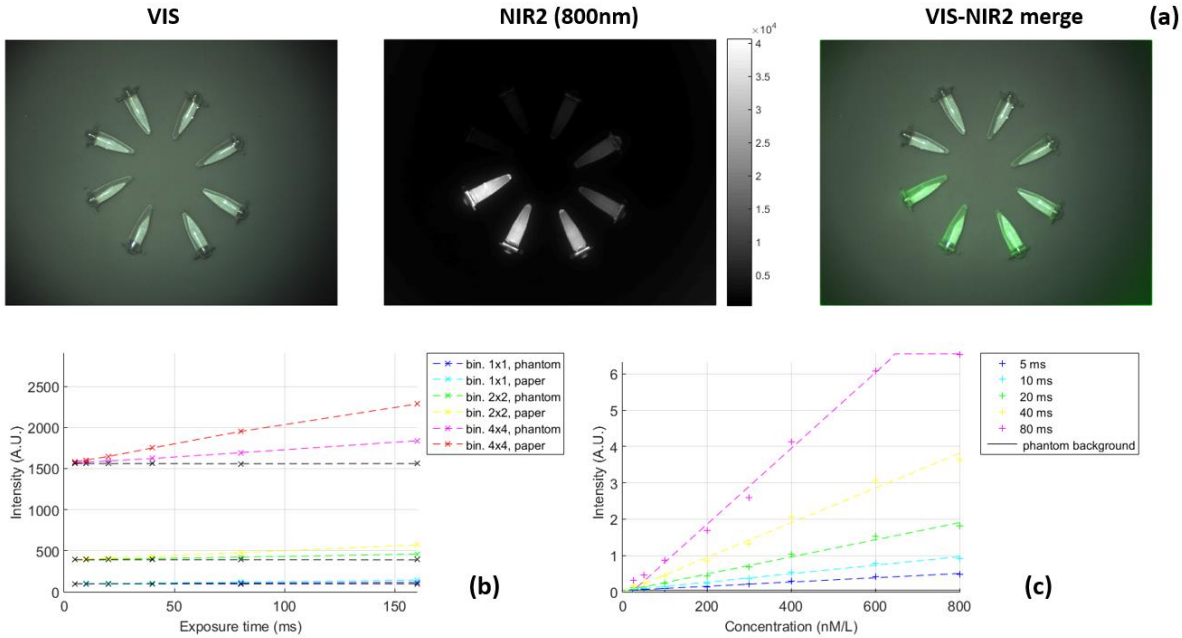


**Figure V.4 – *In-vitro* fluorescence imaging characterization. A set of 8 dilutions of ICG with concentrations ranging from 25 nM/L to 800 nM/L were imaged (a). The contributions to background noise from dark noise and leakage were measured with varying exposure settings and various background materials (b). The fluorescence intensity was extracted from each dilution vial to assess the sensitivity of the imaging system.**

## V.3.2. *In-vivo* fluorescence and oxygenation imaging

**Figure V.5** shows a timeline of the imaging protocol. A comparison of fluorescence and oxygenation imaging in given at three timepoints: during the baseline phase, after 12 minutes of occlusion and 1 minute after reperfusion.

### V.3.1.1. Fluorescence imaging outcome

At 12 minutes into the occlusion phase, a dose of ICG was intravenously injected. Images from the NIR2 and VIS channels were recorded at 12 frames per second with 50 ms exposure time and 2x2 sensor binning while illuminating the surgical field with 760 nm laser light. Fluorescence intensity was monitored in a 120x180 pixels region of interest (ROI) located in the ischemic area and in a 50x50 pixels ROI located in a perfused area. The fluorescence signal reached its peak in the perfused area 35 seconds after injection before decreasing and stabilizing at 58 % of the peak intensity 1 minute later.

After 14 minutes of occlusion, the clamp was released. The fluorescence intensity immediately increases in the ischemic area, as the perfusion resumes. When stabilizing, the intensity reaches 72 % of the intensity in the control area.

### V.3.1.2. Oxygenation imaging outcome

Oxygenation imaging was achieved at 12 frames per second using structured illumination at 0.2 $mm^{-1}$ spatial frequency at 665 nm and 860 nm. **Figure V.5** shows the oxygen saturation trends for the two ROIs over time. During the baseline phase, both ROIs show stable $StO_2$ rates of 77.9 % and 74.6 % respectively in the control and ischemic areas. While the perfused area remains 4% of its baseline value of $StO_2$, oxygenation in the ischemic area decreases until reaching 63.8 % after 12 minutes of occlusion. From 2 minutes and 30 seconds after the occlusion release, the $StO_2$ rate decreases back its baseline state, reaching 75 % after 5 minutes and 30 seconds of reperfusion.

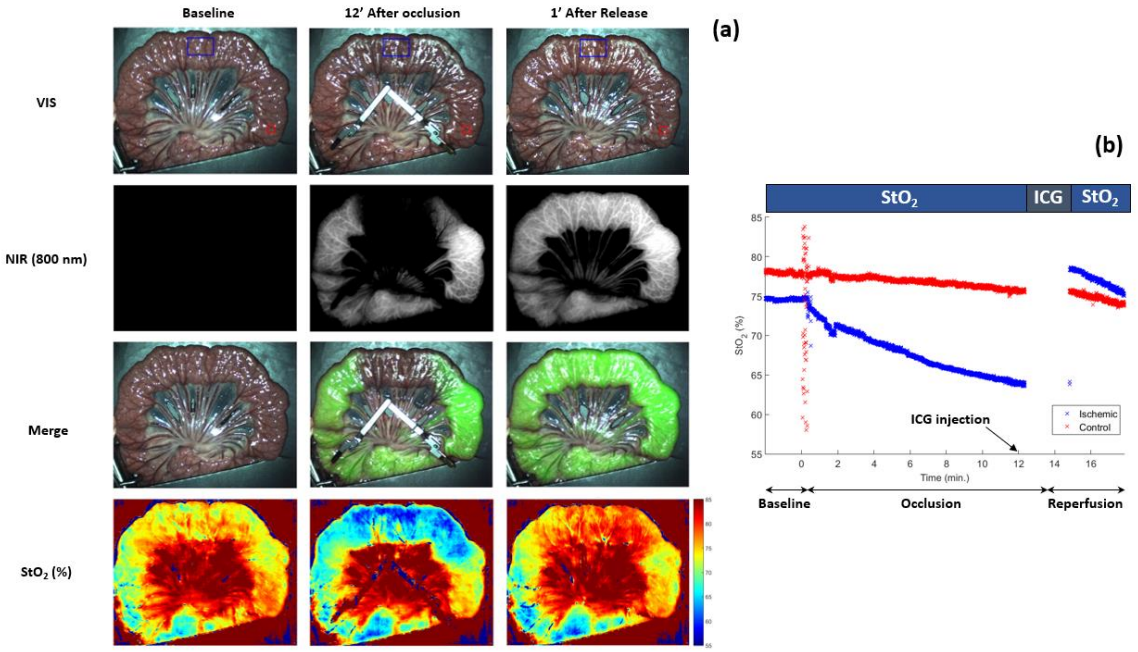


**Figure V.5 – *In-vivo* oxygenation and fluorescence imaging. An occlusion of a portion of a bowel loop was performed for 14 minutes. Oxygenation was monitored prior to clamping and during the 12 first minutes of occlusion. Fluorescence images were recorded from the ICG intravenous injection until 30 seconds after release. Oxygenation imaging resumed for the 3 minutes of the reperfusion phase (a). The absence of fluorescence signal in the ischemic area correlates with the low $StO_2$ rates observed. After reperfusion, this area shows fluorescence signal levels and $StO_2$ rates close to those of the perfused areas (b). Oxygenation rates are steady in the control area whereas ischemia could be detected and quantified in the occluded area.**

## V.4. Discussion

The *in-vitro* characterization of the imaging device demonstrates its performances for optical properties imaging and fluorescence imaging. First, the comparison between tissue-mimicking phantom optical properties obtained from standard SFDI and state-of-the-art deep learning-based SSOP shows good agreement for both absorption and scattering, at 665 nm and 860 nm, as expected from previous published validation of SSOP. Average error below 2.7 % in absorption and 1.7 % in scattering were observed. The considered optical properties were matching the typical range of those of biological tissues, ensuring similar performances for *in-vivo* imaging. Second, the characterization studies demonstrate sensitivity for ICG detection at concentrations as low as 19 nM/L with 40 ms exposure time and 2x2 binning factor, corresponding to ideal exposure parameters to produce real-time fluorescence imaging (25 fps) with high-resolution (1024 x 1280 pixels). Relatively low noise levels were measured, validating the performances of the implemented optical filtering, and ensuring high signal to background ratios.

Next, results from an *in-vivo* preclinical trial on a small bowel model demonstrate the ability of the platform to produce oxygenation rate mapping in real-time, yielding the monitoring of tissue ischemia. More precisely, the oxygenation dynamics could be observed during the ischemic phase, and during the reperfusion phase. These results are in agreement with the outcome of ICG fluorescence, confirming the suitability of $StO_2$ as a metric for blood perfusion monitoring. However, concurrent oxygenation and fluorescence imaging is currently not possible. To this purpose, adjustments in the acquisition workflow are required by either acquiring sequentially reflectance and fluorescence images, or adding an additional NIR channel to the imaging device.

Overall, the design of the imaging platform ensured minimal interference with the surgical workflow by maintaining a long 45 cm working distance, providing bright white light illumination of the surgical field, and by featuring ergonomic handling of the device. However, the presented results were obtained through post-processing. Real-time processing and visualization need to be implemented for use in clinical settings.

## V.5. Conclusion

In conclusion, the design, characterization and validation of a novel multimodal imaging platform for oxygenation and fluorescence imaging in real-time in a clinical environment were presented. The validation of the imaging device was achieved *in-vitro* before demonstrating its performances *in-vivo* in a preclinical study for blood perfusion monitoring in the small bowel.

In Chapter VI and Chapter VII, the capabilities of performing oxygenation imaging for blood perfusion monitoring will be demonstrated, in the cases of ischemia in the small bowel and in the stomach, respectively. These preclinical studies demonstrate the use of oxygen saturation mapping as a reliable indicator to detect and quantify ischemia of tissue, while highlighting the benefits of widefield, real-time imaging. Finally in Chapter VIII, the capabilities of the imaging platform will be extended to quantitative fluorescence imaging. Its impact on tumor surgery will be assessed through a preclinical study.

**References**


[1] Mieog J.S.D., Achterberg F.B., Zlitni A., Hutteman M., Burggraaf J., Swijnenburg R.J., Gioux S., Vahrmeijer A.L., ‘’Fundamentals and developments in fluorescence-guided cancer surgery’’, Nature Reviews Clinical Oncology, 19(1), (2022)

[2] Zhu B., Sevick-Muraca E.M., ‘’A review of performance of near-infrared fluorescence imaging devices used in clinical studies’’, The British Journal of Radiology, 88(1045), (2015)

[3] Dsouza A.V., Lin H., Henderson E.R., Samkoe K.S., Pogue B.W., "Review of fluorescence guided surgery systems: identification of key performance capabilities beyond indocyanine green imaging", Journal of Biomedical Optics, 21(8), 080901, (2016)

[4] Barberio M., Benedicenti S., Pizzicannella M., Felli E., Collins T., Jansen-Winkeln B., Marescaux J., Viola M.G., Diana M., ‘’Intraoperative Guidance Using Hyperspectral Imaging: A Review for Surgeons’’, Diagnostics, 11(11), 2066, (2021)

[5] Mehdorn M., Köhler H., Rabe S.M., Niebisch S., Lyros O., Chalopin C., Gockel I., Jansen-Winkeln B., ‘’Hyperspectral imaging (HSI) in acute mesenteric ischemia to detect intestinal perfusion deficits’’, Journal of Surgical Research, 254, pp. 7-15, (2020)

[6] Weinkauf C., Mazhar A., Vaishnav K., Hamadani A.A., Cuccia D.J., Armstrong D.G., ‘’Near-instant noninvasive optical imaging of tissue perfusion for vascular assessment’’, Journal of Vascular Surgery, 69(2), pp. 555-562, (2019)

[7] Gioux S., Mazhar A., Lee B.T., Lin S.J., Tobias A.M., Cuccia D.J., Stockdale A., Oketokoun R., Ashitate Y., Kelly E., Weinmann M., Durr N.J., Moffitt L.A., Durkin A.J., Tromberg B.J., Frangioni J.V., "First-in-human pilot study of a spatial frequency domain oxygenation imaging system", Journal of Biomedical Optics, 16(8), 086015, (2011)

[8] Aguénounon E., Dadouche F., Uhring W., Gioux S., ‘’Real-time optical properties and oxygenation imaging using custom parallel processing in the spatial frequency domain’’, Biomedical Optics Express, 10(8), pp. 3916-3928, (2019)

[9] Aguénounon E., Smith J.T., Al-Taher M., Diana M., Intes X., Sylvain Gioux S., “Real-time, wide-field and high-quality single snapshot imaging of optical properties with profile correction using deep learning”, Biomedical Optics Express, 11(10), pp. 5701-5716, (2020)

[10] Gioux S., Choi H.S., Frangioni J.V., ‘’Image-Guided Surgery Using Invisible Near-Infrared Light: Fundamentals of Clinical Translation’’, Molecular Imaging, (2010)

[11] Troyan S.L., Kianzad V., Gibbs-Strauss S.L., Gioux S., Matsui A., Oketokoun R., Ngo L., Khamene A., Azar F., Frangioni J.V., ''The FLARE™ intraoperative near-infrared fluorescence imaging system: a first-in-human clinical trial in breast cancer sentinel lymph node mapping'', Annals of Surgical Oncology, 16(10), pp. 2943-2952, (2009)

[12] Cuccia D.J., Bevilacqua F., Durkin A.J., Ayers F.R., Tromberg B.J., "Quantitation and mapping of tissue optical properties using modulated imaging", Journal of Biomedical Optics, 14(2), 024012, (2009)

[13] Vervandier J., Gioux S., "Single snapshot imaging of optical properties", Biomedical Optics Express, 4, pp. 2938-2944, (2013)

[14] Gioux S., Mazhar A., Cuccia D.J., Durkin A.J., Tromberg B.J., Frangioni J.V., ‘’Three-dimensional surface profile intensity correction for spatially modulated imaging’’, Journal of Biomedical Optics, 14(3), 034045, (2009)

# VI. Quantification of bowel ischemia using real-time SSOP imaging

In the previous chapter, a novel imaging system for oxygenation imaging in real-time was presented and characterized. This chapter aims at the validation of this device by validating the measurement of $StO_2$ rates for the detection and quantification of ischemia in the small bowel. A preclinical study was performed for the assessment of blood perfusion in both pure ischemia and ischemia followed by reperfusion settings. The extracted oxygenation rates were shown to be correlated to the capillary lactates concentrations measured by blood sampling. Further confirmed was obtained by histological analysis of the bowel tissues.

The need for blood perfusion assessment during bowel surgery is first detailed, along with currently available tools. Oxygenation imaging and the use of the previously detailed imaging system are briefly presented before introducing the surgical workflow for pure ischemia, and ischemia followed by reperfusion protocols. The correlation between the extracted $StO_2$ rates and sampled capillary lactates concentration is established. Ischemia is then confirmed by histology analysis. Finally, the strengths of oxygenation imaging as a tool for real-time ischemia detection and quantification are discussed.

## VI.1. Context and motivation

Anastomotic leak (AL) is a major complication in digestive surgery accountable for considerable morbidity and mortality [1,2]. The AL incidence is particularly high after esophageal (20-35%) and colorectal resections (4-19%), and in cases which require extraperitoneal anastomosis [3,4]. The pathophysiology of AL is multifactorial and includes patient non-modifiable factors such as comorbidities, nutritional score, and oncological status including neoadjuvant treatment. On the other hand, there are surgical modifiable factors which influence the incidence of AL such as the level of transection ensuring optimal perfusion. Adequate perfusion is a key component of the anastomotic healing process. However, an intraoperative evaluation of perfusion is mostly based subjective clinical criteria, namely serosal discoloration, blood flow from the marginal artery, and pulsatile bleeding at the cut edge of the bowel [5]. As a result, intraoperative technologies which enhance the surgeon's ability to quantify and identify transection and anastomotic sites are strongly required.

Over the past few years, near-infrared fluorescence imaging (FI) based on indocyanine green has been extensively studied as a tool to provide an enhanced evaluation of bowel perfusion in real time [6]. Promising results have been demonstrated in several prospective clinical trials in which ICG-FI improves

surgical outcomes by decreasing the incidence of AL [7,8]. However, the diffusion of the fluorophore from perfused to non-perfused areas and the lack of quantification of fluorescence intensity may lead to an overestimation of marginal zones. Additionally, the estimation of perfusion using fluorescence angiography (FA) mandates the use of an exogenous agent, which is one of the main burdens of exogenous fluorescence [5].

Alternatively to exogenous fluorescence imaging, non-invasive label-free real-time optical imaging technologies have been developed. They are promising tools since they allow for an adequate surgical workflow without the constraints of administering external chemical compounds to the human body. Consequently, the clinical translation of such endogenous optical imaging-based devices can be accelerated and disseminated. In order to obtain physiological local information, most devices used are based on NIR spectroscopy, such as hyperspectral and multispectral imaging technologies [9]. A spectroscopic approach allows for non-contact reading of $StO_2$ with high spatial resolution and with a large field of view (>15x15 $cm^2$), thereby improving intraoperative decision-making by adding quantitative information. Single Snapshot of Optical Properties has recently been developed. It is a contrast-free real-time non-invasive optical imaging technique, which allows to evaluate physiological tissue properties. SSOP is based on the well-known diffuse optimal imaging method named spatial frequency domain imaging which uses light propagation models to quantify optical properties, discriminating light scattering from tissue microstructures from light absorption by tissue molecular constituents [10]. Therefore, SSOP is able to determine tissue oxygenation by extracting the fraction of oxygenated over total hemoglobin in real-time. It has proven to be an efficient method since it allows the reduction of the number of image acquisitions down to a single frame, enabling real-time imaging. This constitutes a great advantage in the surgical setting, hence preventing from workflow disruption [11]. Its previously evaluated performance during *in vivo* non-experimental models has proven to achieve a high accuracy (i.e., less than a 10% error) [12]. The aim of this experimental study was to preclinically evaluate the accuracy of SSOP in quantifying bowel perfusion using robust and validated biomarkers such as capillary lactates.

## VI.2. Materials and methods

### VI.2.1. Real-time oxygenation imaging

*SSOP Imaging*

Single Snapshot imaging of Optical Properties is based on the projection of spatially modulated patterns of light on the sample and on the acquisition with a camera of the diffused back reflected light. SSOP was developed as a real-time adaptation of the more time-consuming phase-shift SFDI which requires at least

six frames for the extraction of the optical properties of tissues. Indeed, in a standard SFDI workflow, two different spatial frequency profiles (e.g., 0 $mm^{-1}$ and 0.2 $mm^{-1}$) with three-phase shifts for each of them are projected on the sample surface, allowing for the demodulation of the signal into its DC and AC components [13]. Differently, SSOP requires only a single high frequency pattern to be projected on the tissue, thanks to a Fourier's domain filtering approach for the demodulation step, thus reducing from six to one the number of frames needed for the acquisition and enabling for a real-time capability of the imaging system [14]. Following the demodulation, both SFDI and SSOP share the same workflow starting from a calibration step involving the measurement of a calibration phantom with known optical properties. The measurements of this tissue mimicking phantom allows us to to compute the diffuse reflectance maps for the sample, i.e., RDC (0 $mm^{-1}$) and RAC (0.2 $mm^{-1}$). Finally, a Monte Carlo-based look-up table algorithm, allows to retrieve the optical properties of the sample (i.e., absorption and reduced scattering coefficients) for each pixel of the image [15]. The natural consequences of the single frame approach are a degradation in image quality and the presence of edge artefacts. Nevertheless, significant improvements have been achieved in recent years by first optimizing the filtering technique and by adopting deep neural network approaches for the demodulation [16]. Additionally, the latest developments on SSOP also account for a tridimensional profile correction of the sample in order to reduce the quantification error of SSOP associated with a variation of light intensity across non-flat sample surfaces [12].

*Deep Learning Method for SSOP*

For this study, the latest SSOP deep learning-based approach replaced the standard Fourier's domain filtering technique to improve the overall image quality, as described by Aguénounon et al. [12]. Briefly, two dedicated CNNs based on a U-Net architecture were used for the extraction of the modulation amplitude of the signal for each spatial frequency, and for the profilometry analysis of the surface profile of the sample. Both networks were trained using high quality images obtained with SFDI acquisition sequences (with 7 phase shifts instead of 3 to enhance quantification accuracy and image quality) and optimized for efficient and low-cost computation performances, enabling a real-time capability and achieving high visual quality optical property quantification for up to 1 MP images. The training dataset consisted of a total of 200 high quality images divided into $N = 40$ images of tissue-mimicking silicone phantoms with different optical properties ranging from $\mu_a$ = 0.005 to 0.05 $mm^{-1}$ for absorption and from $\mu_s'$ = 0.5 to *3* $mm^{-1}$ for reduced scattering; $N = 52$ images of hands from different Caucasian men and women in various configurations; N = 108 images from ex vivo and in vivo swine organs in several orientations (stomach, small bowel, colon, kidney, pancreas, liver, and spleen).

## VI.2.2. Clinically-compatible imaging system

The imaging system is based on a digital-micro-mirror device (DMD, Vialux GmbH, Chemnitz, Sachsen, Germany) to project structured light in the form of sinusoidal patterns at 45 ± 5 cm working distance. The projection system is fiber-coupled to a dedicated, custom-made, class 3R high-power laser source composed of laser diodes (LDX Optronics, Maryville, TN, USA) and used here to project patterns at 665 nm and 860 nm for oxygen saturation measurements [17]. A white high power LED lamp (LO-35, Fiberoptics Technology, CT, USA) is also used to illuminate the surgical field to provide anatomical visualization specifically filtered to avoid impeding oxygen saturation measurements. The imaging head is built with three CMOS cameras (JAI GO-5000M-USB, JAI Ltd., Kanagawa, Japan; Edge 4.2, Excelitas PCO GmbH, Kelheim, Germany; JAI GO-5000C-USB, JAI Ltd., Kanagawa, Japan,) sharing the same field of view of 15x15 $cm^2$ for the collection of the NIR1 (665 nm), NIR2 (860 nm) and the RGB channels with a resolution of 1024x1280 pixels. In addition, low-pass and high-pass filters are used in the optical path to isolate the different wavelengths (Chroma,VT, USA). A pair of linear polarizers (PPL05C, Moxtek, Orem, UT, USA) in crossed configuration are also employed at the projection and imaging sides to reject the contribution from specular reflections at the surface of the sample. A silicone-based optical phantom (21 cm x 21 cm x 2 cm) with known optical properties ($\mu_a = 0.01\ mm^{-1}$ and $\mu_s' = 1.1\ mm^{-1}$ at 665 nm, and $\mu_a = 0.01\ mm^{-1}$ and $\mu_s' = 1.1\ mm^{-1}$ at 860 nm) is used for the calibration of the imaging system. The imaging workflow consists of the simultaneous projection of a high frequency sinusoidal pattern (i.e. 0.3 $mm^{-1}$) at the two wavelengths (665 nm and 860 nm) followed by the three channels acquisition of the images for the extraction of the oxygen saturation level of the tissue. An illustration of the imaging system is shown in **Figure VI.1**.

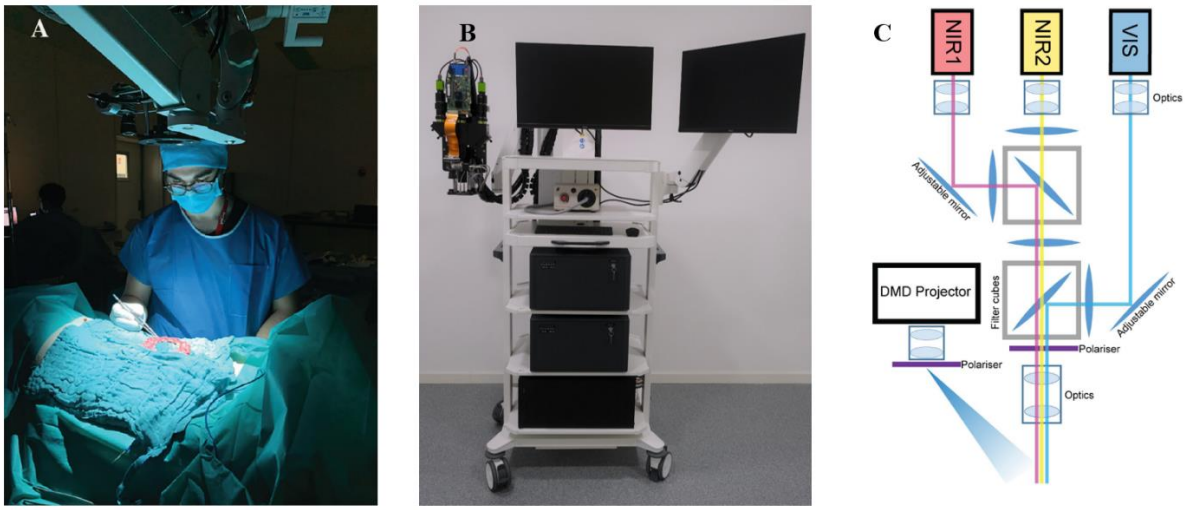


**Figure VI.1 – Imaging system illustration. A: the imaging system provides bright filtered white light for illuminating the surgical field. The large working distance – typically 45cm – ensure minimal interference with the surgical workflow. B: The imaging platform, equipped with a mounted imaging head, mounted displays, white light LED-based lamp, custom laser sources and a working station for device control, data processing and data storage.**

## VI.2.3. Animal model and bowel ischemia model

*Animal models*

A total of six adult swines (*Sus scrofa domesticus*, Large white) were involved in this non-survival study. The present experimental study is part of the QuantSURG (Quantitative Surgical Guidance for Colorectal Surgery) project, which received full approval from the local Ethical Committee on Animal Experimentation (ICOMETH No. 038.2019.01.121) and by the French Ministry of Superior Education and Research (MESR) under the following reference: APAFIS #20819-2019052411591088 v3. All animals used in the experimental laboratory were managed according to French laws for animal use and care and according to the directives of the European Community Council (2010/63/EU) and ARRIVE guidelines [18]. The animals were fasted for 24 hours with free access to water before surgery. Animals were premedicated, 10 minutes before surgery with an intramuscular injection of ketamine (20 mg/kg) and azaperone (2 mg/kg) (Stresnil; Janssen-Cilag, Belgium). Intravenous propofol (3 mg/kg) combined with rocuronium (0.8 mg/kg) were used for induction. Anesthesia was maintained with 2% isoflurane. At the end of the procedures, pigs were sacrificed with an intravenous injection of a lethal dose of potassium chloride.

*Pure ischemia model*

A central venous line was placed by means of internal jugular vein venodissection. A midline laparotomy was performed using electrocautery. A self-retaining retractor was then placed and a 20cm small bowel loop was exposed in order to create bowel ischemia by diving arcade branches. Five regions of interest were marked with an interrupted suture in the antimesenteric border (ROI 1: central ischemic; ROI 2: left marginal; ROI 3: left vascularized (2.5 cm from ROI 2); and symmetrically ROI 4: right marginal; ROI 5: right vascularized (2.5 cm from ROI 4)). The small bowel was imaged following the SSOP imaging workflow at 665 nm and 860 nm before and after the ischemia at different time points (T0, T15, T30, T45, T60 min). The SSOP image acquisitions were performed in the dark (i.e., with the light turned off in the operating room), in order to reduce the risk of bias from background noise in the raw data. Nevertheless, the system can be also operated in standard ambient light conditions via an adapted calibration routine.

*Ischemia / reperfusion model*

To assess the accuracy of the imaging system in detecting oxygenation changes a short ischemia/reperfusion model was designed. Same surgical principles were preserved for laparotomy. Six 20 cm small bowel loops were exposed in order to create short bowel ischemia by diving the peritoneal layer of the mesentery with sufficient length to apply a bulldog clamp. Similarly, to the pure ischemic model five regions of interest were marked with an interrupted suture in the antimesenteric border (ROI 1: central ischemic; ROI 2: left marginal; ROI 3: left vascularized (2.5 cm from ROI 2); and symmetrically ROI 4: right

marginal; ROI 5: right vascularized (2.5 cm from ROI 4) in each loop. Small bowel loops were imaged following the same workflow previously employed, during clamping and after declamping at the reperfusion phase (T0, and T10 and T14 min respectively).

### VI.2.4. Capillary lactates for ischemia monitoring

*Capillary lactates*

For the pure ischemia model, local capillary lactates concentrations (mmol/L) were measured at each time points by means of a portable analyzer (EDGE ®lactate analyser, ApexBio, Taipei, Taiwan). Lactate being a product of the glycolysis process, its accumulation reflects a lowered mitochondrial activity in the presence of reduced $O_2$ concentration. This method has been described earlier in studies on the metabolic effect of bowel resection [19,20]. Systemic lactates were also measured in venous blood retrieved from the central line and using the EPOC® Blood Analysis System (Siemens Healthcare, Germany), a portable blood analyzer.

*Histological analysis*

For the pure ischemic model, full thickness biopsies were retrieved at the end of the procedure, specimens were fixed in a 4% formalin solution for at least 24 hours. Four µm thick sections were cut from paraffin-embedded tissues and stained with hematoxylin and eosin. Biopsies were taken from each ROI after 60 minutes of ischemia and one from a distal part before the creation of the ischemic loop, which served as a control. A microscopic assessment was made (Leica 2000 LED, Leica Biosystems GmbH, Wetzlar, Germany) using Park/Chiu's scoring system of intestinal ischemic damage [21, 22].

*Statistical analysis*

All statistical analyses were performed using the GraphPad Prism software for macOS (GraphPad Software, Inc. USA), version 9.1.1. Data are shown as mean and standard deviation (SD) unless otherwise indicated. Local capillary lactates were normalized by the systemic lactates concentrations to reduce better reflect the local variations of lactates within the bowel tissue. In order to assess the correlation between normalized lactates and SSOP-$StO_2$, a Pearson's rank correlation coefficient was calculated. A Student's t test was used to compare continuous variables after confirmation of a parametric distribution using the Kolmogorov-Smirnov normality test. A p value $< 0.05$ was considered statistically significant.

## VI.3. Results

### VI.3.1. *In-vivo* oxygenation imaging outcome

*Pure ischemia model*

The mean value of SSOP-$StO_2$ in ROI 1 was 30.08 % ± 6.96 and was significantly lower when compared to marginal ROIs (ROI2 + ROI 4: 45.67 % ± 10.02, $p < 0.0001$), and to vascularized ROIs (ROI 3 + ROI 5: 48.08 % ± 7.08, $p < 0.0001$). Although the SSOP-$StO_2$ was higher in vascularized ROIs, this difference was not statistically significant ($p = 0.13$). **Figure VI.2** shows the imaging outcome for one of the subjects.

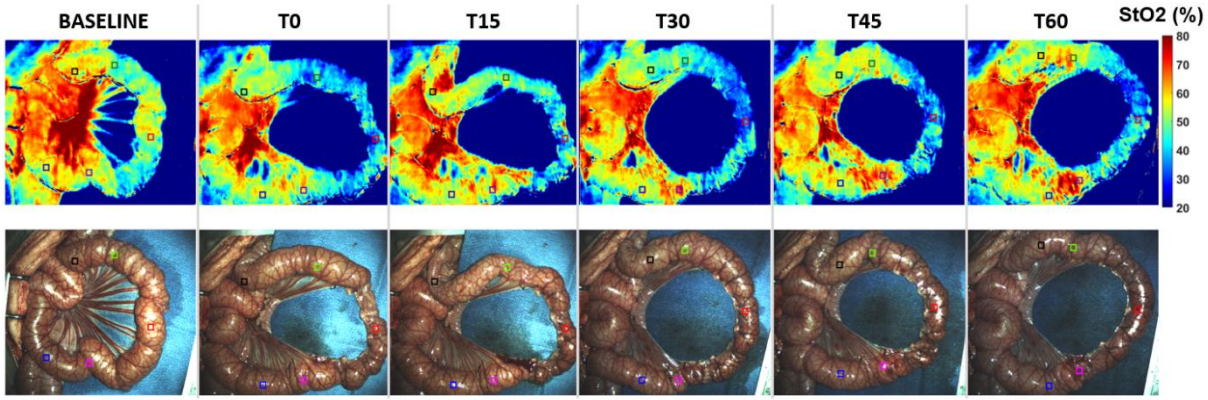


**Figure VI.2 – Pure ischemia model oxygenation imaging outcome. Top row: Oxygenation maps are shown at each lactates measurement time points. Bottom row: color images are shown for anatomical reference. The 5 ROIs are represented by color squares in the images. Oxygenation maps show steady high oxygenation rates in the perfused areas and consistently decreasing rates in the ischemic area. A transition zone is shown between the perfused and ischemic areas.**

*Ischemia / reperfusion model*

In the short ischemia / reperfusion model we found that ROI 1 has a mean 57.54 ± 5.35, 37.6 ± 4.12 and 62.40 ± 7.28 $StO_2$ at T0, T10 and T15 respectively. The difference in term of $StO_2$ value from occlusion to reperfusion was statistically significant ($p < 0.0002$) (**Figure VI.4**) Marginal ROIs (ROI 2 + ROI 4) had a mean 57.22 ± 5.61, 56.89 ± 5.49 and 60.93 ± 6.91 $StO_2$ at T0, T10 and T15. While for the vascularized ROIs (ROI 3 + ROI 5) 62.53 ± 5.43, 59.71 ± 6.37 and 64.40 ± 6.80 $StO_2$ at T0, T10 and T15 was found. In marginal ROIs (ROI 2 + ROI 4) the differences in terms of $StO_2$ from occlusion to reperfusion was not statistically significant different ($p=0.15$), similarly to vascularized ones ($p=0.12$). **Figure VI.3** shows the oxygenation imaging outcome for one bowel loop.

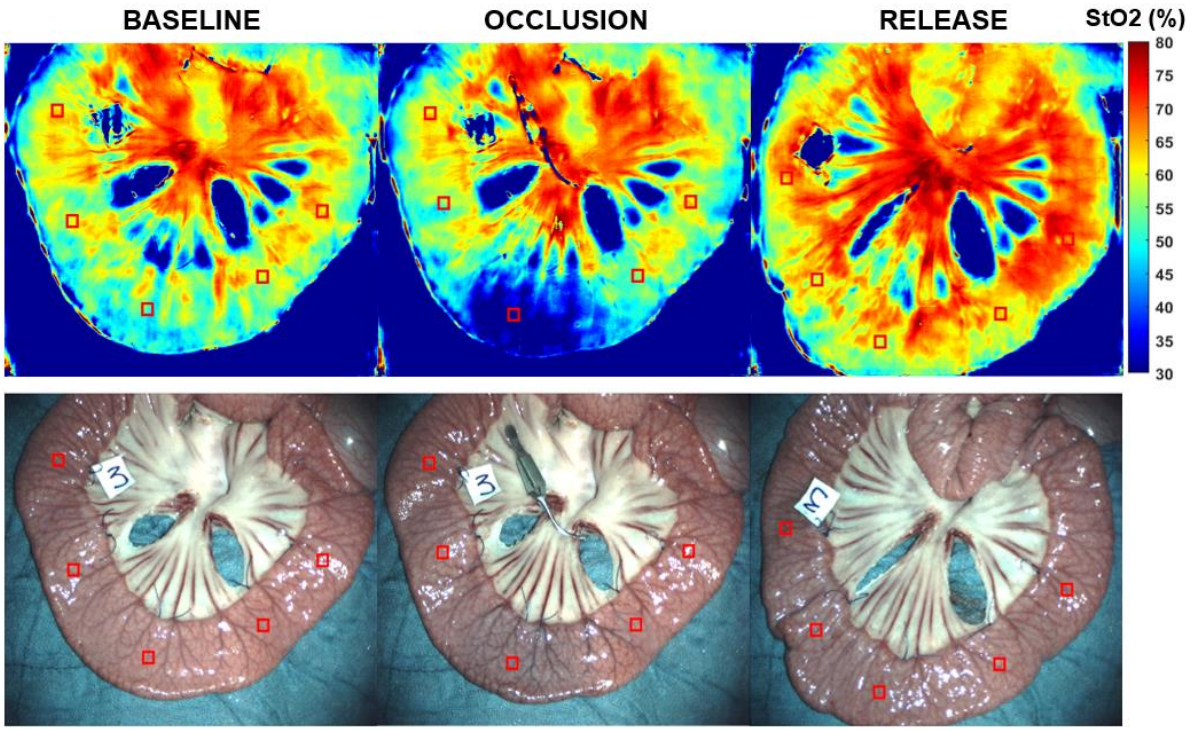


**Figure VI.3 – Ischemia / reperfusion model oxygenation imaging outcome. Top row: Oxygenation maps are shown at different time points: before occlusion (baseline), after 10 minutes of occlusion (occlusion) and 4 minutes after occlusion release (release). Bottom row: color images are shown for anatomical reference. Similar behavior is exhibited compared to the pure ischemia model until the release of the occlusion. After releasing the occlusion, reperfusion occurs and the formerly ischemic area shows $StO_2$ rates similar to those during of the baseline, and those of the perfused areas.**

## VI.3.2. Capillary lactates and oxygenation correlation

The oxygenation rates and capillary lactates measurements and correlation are compiled in **Figure VI.5**. In the pure ischemia model, the mean value of normalized lactates in ROI 1 was 4.80mmol/L ± 2.59 and was significantly higher when compared to marginal ROIs (ROI 2 + ROI 4: 1.03 mmol/L ± 0.47 $p < 0.0001$), and to vascularized ROIs (ROI 3 + ROI 5: 0.75 ± 0.25 mmol/L, $p < 0.0001$). The difference between marginal and vascularized ROIs also showed a statistically significant difference ($p < 0.0001$). The cumulative Pearson's correlation analysis between normalized lactates and SSOP-$StO_2$ was -0.589, $p<0.0001$.

As for the histopathological confirmation, the mean Park/Chiu's score at ROI 1 was 4.50 ± 0.84 and was significantly higher than marginal zones (ROI 2 + ROI 4: 1.58 ± 1.10) $p < 0.0001$ and vascularized (ROI 3 + ROI 5: 0.667 ± 0.650), $p < 0.0001$. At T65, the Park/Chiu's score correlation between SSOP-$StO_2$ was $r= -0.6251$, $p=0.0002$ and between normalized lactates was $r=0.710$, $p < 0.0001$.

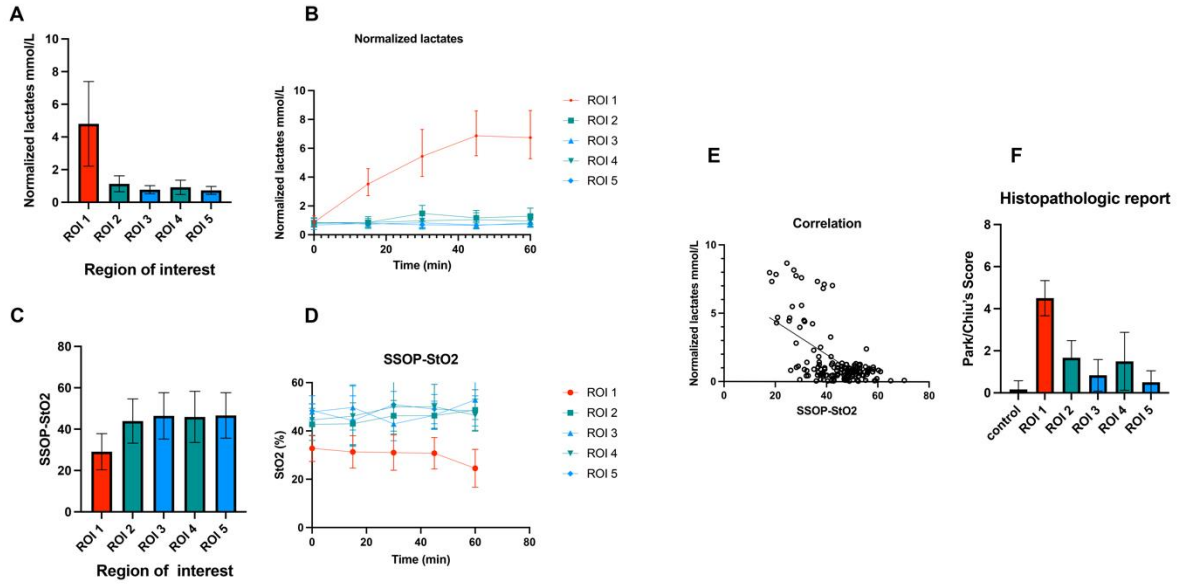


**Figure VI.4 – $StO_2$ correlation with normalized lactates in the pure ischemia model. A: Normalized lactates (mmol/L) during 1 hour of ischemia: the mean value of normalized lactates in ROI 1 was 4.80 ± 2.59 and was significantly higher when compared to marginal ROIs (ROI2 + ROI 4: 1.03 ± 0.47, p < 0.0001), and to vascularized ROIs (ROI 3 + ROI 5: 0.75±0.25, p < 0.0001). The difference between marginal and vascularized ROIs also showed a statistically significant difference p < 0.0001. B: Kinetics of normalized lactates (mmol/L). C: SSOP-$StO_2$ values during 1 hour of ischemia: the mean value of SSOP-$StO_2$ in ROI 1 was 30.1 ± 6.96 and was significantly lower when compared to marginal ROIs (ROI 2 + ROI 4: 45.67 ± 10.02 p < 0.0001), and to vascularized ROIs (ROI 3+ ROI 5: 48.08±7.08, p=<0.0001). Although SSOP-StO2 was higher in vascularized ROIs, it did not show any statistically significant difference (p=0.1298). D: Kinetics of $StO_2$ cartography in each ROI. E: Pearson's correlation analysis between normalized lactates and SSOP-$StO_2$ in correspondence to all ROIs. F: Histopathological report: the mean Park/Chiu's score at ROI 1 was 4.50 ± 0.84 and was significantly higher than marginal zones (ROI 2 and ROI 4: 1.58 ± 1.097, p < 0.0001) and vascularized (ROI 3 and ROI 5: 0.67 ± 0.65, p < 0.0001).**

## VI.4. Discussion

In the presented experimental pure bowel ischemia model, the imaging platform could provide accurate quantification of tissue $StO_2$, which is a useful indicator of tissue viability. Additionally, the extracted $StO_2$ values were correlated with a validated marker of tissue perfusion such as strip-based capillary lactates [20]. Local bowel capillary lactates were normalized via systemic lactates to reduce the variability between animals. The high number of paired normalized capillary lactates and $StO_2$ datasets (175) at different time points allowed to compute a statistically significant negative correlation between those two parameters.

Additionally, $StO_2$ images from the imaging platform were also correlated with the histopathological ischemic score. The Park/Chiu's score used in this experiment was based on all intestinal layers. Although is well-known that the intestinal mucosa and submucosa are the first ones affected by impaired perfusion since they receive most of the mesenteric blood flow (70%), the muscularis and serosal layers can also be

damaged during ischemic periods [23]. Ischemic ROIs mostly presented with denuded villi and dilated capillaries. However, the evaluation of the $StO_2$ images was performed in the serosal side and consequently, histopathological repercussions in external layers are definitely elements of interest. Nevertheless, one must stress that this was a short-term ischemia model (1 hour), and transmural necrosis is mostly developed after longer ischemic periods (6 hours) [23]. In fact, the higher Park/Chiu's score of 6, which represents crypt layer injury was found in one case only. To verify the accuracy of the imaging system a short ischemia / reperfusion model was employed in which the device was able to detect the decrease of $StO_2$ as soon as the clamping occurred. As for the reperfusion, once the bulldog clamp was released the imager was able to detect an $StO_2$ improvement in the ischemic area.

Intraoperative perfusion assessment constitutes a critical issue during digestive surgery. In NIR-FA, ICG has been so far the most commonly used fluorophore to evaluate local microperfusion [25]. ICG-FA has been rapidly expanded by the increasing availability of optical imaging systems [26-28]. However, ICG-FA has limitations, most ICG-FA optical systems are based on relative fluorescence intensity without considering diffusion, since perfusion is a dynamic process in which the fluorophore tents to distribute into ischemic areas overtime, the static evaluation can lead to an overestimation on non-perfused areas. Secondly, the fluorescence intensity is inversely correlated to the source-to-target distance, this fact makes those structures closer to the source brighter than areas faraway. To prevent from distance bias, distance standardization between the NIR-endoscope and the surgical field and/or the use of a reference calibration tool must be performed during image acquisition [29].

In order to overcome ICG-FA drawbacks, quantification methods which are independent of distance have been developed to obtain a perfusion cartogram based on the dynamic uptake of the fluorophore over time such as fluorescence-based enhanced reality (FLER) or Q-ICG [25,30,31]. Although the use of quantitative methods offers significant improvement as a reproductible and robust solution, at present they have not been extensively adopted. Despite exogenous fluorescence is a well-established intraoperative technology to assess gastrointestinal perfusion, there is still no standardized approach regarding its use as reported in the IHU-IRCAD-EAES EURO-FIGS registry recently [32]. Certainly, the highest level of evidence holds promising result regarding the impact of ICG-FA in decreasing AL, nevertheless the quality of non-randomized retrospective clinical studies included in the latest meta-analyses must be considered, as well as non-quantitative methods used to estimate perfusion [33-36].

As compared to FA, endogenous imaging methods including SSOP can provide a greater amount of quantitatively significant data by characterizing several tissue components including StO2 which reflects intracellular metabolic changes induced by ischemia. HSI is an eminent well-known example of endogenous imaging technology, as previously discussed data extraction by means of HSI is based on NIR spectroscopy. The accuracy of HSI to evaluate perfusion has been studied during esophagectomy, in 22 patients HSI was able to discriminate between gastric conduits with and without laparoscopic ischemic preconditioning ($StO_2$

66% vs 78%, p = 0.03) [37]. Additionally, perfusion assessment in colorectal surgery has been compared between HSI and FA showing comparable results in detecting the optimal demarcation line [38].

Although HSI is a promising technology, it does not allow for a video rate acquisition and the large datasets require post-processing algorithms to discriminate features according to spectral curves. To overcome this limitation, a novel method named HYPerspectral Enhanced Reality (HYPER) was proposed. HYPER has shown in a preclinical trial superior results in detecting tissue oxygenation as compared to quantitative fluorescence angiography [9]. However, HYPER requires images superimposition using augmented reality onto real-time videos to achieve real-time intraoperative guidance making its use currently limited [3]. At present, SSOP is a more adapted surgical navigation system method since it allows for a video rate non-invasive, wide-filed (> 100 $cm^2$), quantitative multispectral characterization of metabolic properties through a single frame acquisition [39]. As previously stressed, SSOP is based on SFDI which is a noncontact multispectral optical imaging method that allows for accurate measurement of tissue optical properties over large fields of view [14,40]. The importance of SFDI lies on the independent measurement of light absorption and scattering.

In the first in-human pilot trial which evaluate three patients, SFDI proved to be accurate in assessing oxygenation of microsurgical deep inferior epigastric perforator flaps during reconstructive breast surgery [41]. Nevertheless, SFDI is time consuming since it requires the acquisition of several images (i.e., at least 6) being inconvenient for the surgical workflow. To address these constraints SSOP was developed as enhanced fast optical intraoperative navigation tool. However, with the conventional process with images reduction SSOP initially suffered from degraded visual quality as compared to the 7-phase SFDI. Artificial intelligence has been used to overcome these issues, using a GPU-accelerated deep learning algorithm. SSOP GPU-accelerated DL evaluation of *in vivo* human hands and *ex vivo* animal organs showed superiority in terms of image resolution and degradation as compared to classical SSOP-filtering approach. Errors as low as 7.5 ± 2.7 % were presented with this DL processing methodology [12].

## VI.5. Conclusion

Herein, the imaging platform uses SSOP GPU-accelerated- DL using Convolutional Neural Networks (CCNs) and allows for a non-contrast physiological real-time assessment in an *in vivo* one-hour ischemic model. Additionally, the use of artificial intelligence helped to maintain high image quality comparable to the 7-phase SDFI. The promising results presented in this article of SSOP-$StO_2$ can be potentially expanded into other fields for surgical guidance.

This study relies on a robust methodology. The limited number of animals represents a limitation since six pigs were only studied, which could account for the inter-animal variation in terms of capillary lactates and

$StO_2$ values. Another downside of the present study lies in its non-survival design, which does not make it possible to evaluate the impact of SSOP on anastomotic healing. Consequently, future studies should include a survival anastomotic model to fully assess the potential of SSOP-based oxygenation imaging for improving the outcome of anastomotic procedures.

In conclusion, the design of the imaging device made its integration into an open-surgery workflow effortless. Oxygenation mapping was performed safely, and the operating conditions were comfortable. Based on standardized metabolic biomarkers, SSOP-$StO_2$ allows for a contrast-free accurate assessment of small bowel perfusion identifying physiological tissue properties.

Anastomotic leakage is a common complication related to surgery throughout the abdominal cavity. This includes esophagectomy procedures, which are considered in the next chapter.

**References**


[1] Dindo D, Demartines N, Clavien PA., ''Classification of surgical complications: A new proposal with evaluation in a cohort of 6336 patients and results of a survey'', Ann Surg., 240, pp. 205–213, (2004)

[2] Frasson M, Flor-Lorente B, Rodríguez JLR, Granero-Castro P, Hervás D, Alvarez Rico MA, et al, ''Risk factors for anastomotic leak after colon resection for cancer: Multivariate analysis and nomogram from a multicentric, prospective, national study with 3193 patient', Ann Surg., 262, pp. 321–330, (2015)

[3] Barberio M, Longo F, Fiorillo C, Seeliger B, Mascagni P, Agnus V, et al, ''HYPerspectral Enhanced Reality (HYPER): a physiology-based surgical guidance tool'', Surg. Endosc., 34, pp. 1736–1744, (2020)

[4] McDermott FD, Heeney A, Kelly ME, Steele RJ, Carlson GL, Winter DC, ''Systematic review of preoperative, intraoperative and postoperative risk factors for colorectal anastomotic leaks'', Br. J. Surg., 102, pp. 462–479, (2015)

[5] Pampiglione T, Chand M., ''Enhancing colorectal anastomotic safety with indocyanine green fluorescence angiography: An update'', Surg. Oncol., 101545, (2021)

[6] Mascagni P, Longo F, Barberio M, Seeliger B, Agnus V, Saccomandi P, et al, ''New intraoperative imaging technologies: Innovating the surgeon's eye toward surgical precision'', J. Surg. Oncol., 118, pp. 265–282, (2018)

[7] Jafari MD, Wexner SD, Martz JE, McLemore EC, Margolin DA, Sherwinter DA, et al, ''Perfusion assessment in laparoscopic left-sided/anterior resection (PILLAR II): A multi-institutional study'', J. Am. Coll. Surg., 220, pp. 82-92, (2015)

[8] Ris F, Liot E, Buchs NC, Kraus R, Ismael G, Belfontali V, et al, ''Multicentre phase II trial of near-infrared imaging in elective colorectal surgery'', Br. J. Surg., 105, pp. 1359–1367, (2018)

[9] Barberio M, Felli E, Seyller E, Longo F, Chand M, Gockel I, et al, ''Quantitative fluorescence angiography versus hyperspectral imaging to assess bowel ischemia: A comparative study in enhanced reality'', Surg., 168, pp. 178–184, (2020)

[10] Gioux S, Mazhar A, Cuccia DJ., ''Spatial frequency domain imaging in 2019: principles, applications, and perspectives'', J. Biomed. Opt., 20(24), 2019

[11] Schmidt M, Aguénounon E, Nahas A, Torregrossa M, Tromberg BJ, Uhring W, et al, ''Real-time, wide-field, and quantitative oxygenation imaging using spatiotemporal modulation of light'', J. Biomed. Opt., 24(1), 2019

[12] Aguénounon E, Smith JT, Al-Taher M, Diana M, Intes X, Gioux S., ''Real-time, wide-field and high-quality single snapshot imaging of optical properties with profile correction using deep learning'', Biomed. Opt. Express'', 11(5701), (2020)

[13] Cuccia DJ, Bevilacqua F, Durkin AJ, Ayers FR, Tromberg BJ, ''Quantitation and mapping of tissue optical properties using modulated imaging'', J. Biomed. Opt., 14, 024012, (2009)

[14] van de Giessen M, Angelo JP, Gioux S., ''Real-time, profile-corrected single snapshot imaging of optical properties'', Biomed. Opt. Express, 6(4051), (2015)

[15] Angelo J, Vargas CR, Lee BT, Bigio IJ, Gioux S, ''Ultrafast optical property map generation using lookup tables'', J. Biomed. Opt., 21,110501, (2016)

[16] Aguénounon E, Dadouche F, Uhring W, Gioux S, ''Single snapshot of optical properties image quality improvement using anisotropic two-dimensional windows filtering'', J. Biomed. Opt., 24(1), (2019)

[17] Mazhar A, Dell S, Cuccia DJ, Gioux S, Durkin AJ, Frangioni J V., et al, ''Wavelength optimization for rapid chromophore mapping using spatial frequency domain imaging'', J. Biomed. Opt., 15, 061716, (2010)

[18] Kilkenny C, Browne WJ, Cuthill IC, Emerson M, Altman DG, ''Improving bioscience research reporting: The arrive guidelines for reporting animal research'', PLoS Biol., 8, pp. 6–11, (2010)

[19] Quero G, Lapergola A, Barberio M, Seeliger B, Saccomandi P, Guerriero L, et al, ''Discrimination between arterial and venous bowel ischemia by computer-assisted analysis of the fluorescent signal'', Surg. Endosc., 33, pp. 1988–1997, (2019)

[20] Diana M, Noll E, Diemunsch P, Moussallieh FM, Namer IJ, Charles AL, et al, ''Metabolism-Guided Bowel Resection: Potential Role and Accuracy of Instant Capillary Lactates to Identify the Optimal Resection Site'', Surg. Innov., 22, pp. 453–461, (2015)

[21] Quaedackers JSLT, Beuk RJ, Bennet L, Charlton A, Oude Egbrink MGA, Gunn AJ, et al., ''An evaluation of methods for grading histologic injury following ischemia/reperfusion of the small bowel'', Transplant. Proc., 32, pp. 1307–1310, (2000)

[22] Chiu C-J., ''Intestinal Mucosal Lesion in Low-Flow States'', Arch. Surg., 101(478), (1970)

[23] Seeliger B, Agnus V, Mascagni P, Barberio M, Longo F, Lapergola A, et al, ''Simultaneous computer-assisted assessment of mucosal and serosal perfusion in a model of segmental colonic ischemia'', Surg. Endosc., 34, pp. 4818–4827, (2020)

[24] Strand-Amundsen RJ, Reims HM, Reinholt FP, Ruud TE, Yang R, Høgetveit JO, et al, ''Ischemia/reperfusion injury in porcine intestine - Viability assessment'', World J. Gastroenterol., 24, pp. 2009–2023, (2018)

[25] Diana M, Agnus V, Halvax P, Liu YY, Dallemagne B, Schlagowski AI, et al, ''Intraoperative fluorescence-based enhanced reality laparoscopic real-time imaging to assess bowel perfusion at the anastomotic site in an experimental model'', Br. J. Surg., 102, pp. 169–176, (2015)

[26] Hirche C, Engel H, Kolios L, Cognie J, Hünerbein M, Lehnhardt M, et al, ''An experimental study to evaluate the fluobeam 800 imaging system for fluorescence-guided lymphatic imaging and sentinel node biopsy'', Surg. Innov., 20, pp. 516–523, (2013)

[27] Yamashita SI, Tokuishi K, Anami K, Miyawaki M, Moroga T, Kamei M, et al, ''Video-assisted thoracoscopic indocyanine green fluorescence imaging system shows sentinel lymph nodes in non-small-cell lung cancer'', J. Thorac. Cardiovasc. Surg., 141, pp. 141–144, (2011)

[28] Meershoek P, KleinJan GH, van Willigen DM, Bauwens KP, Spa SJ, van Beurden F, et al, ''Multi-wavelength fluorescence imaging with a da Vinci Firefly—a technical look behind the scenes'', J. Robot. Surg., 137, (2020)

[29] D'Urso A, Agnus V, Barberio M, Seeliger B, Marchegiani F, Charles AL, et al, ((Computer-assisted quantification and visualization of bowel perfusion using fluorescence-based enhanced reality in left-sided colonic resections'', Surg. Endosc., (2020)

[30] Nerup N, Andersen HS, Ambrus R, Strandby RB, Svendsen MBS, Madsen MH, et al, ''Quantification of fluorescence angiography in a porcine model'', Langenbeck's Arch. Surg., 402, pp. 655–662, (2017)

[31] Gosvig K, Jensen SS, Qvist N, Nerup N, Agnus V, Diana M, et al, ''Quantification of ICG fluorescence for the evaluation of intestinal perfusion: comparison between two software-based algorithms for quantification'', Surg. Endosc., (2020)

[32] Spota A, Al-Taher M, Felli E, Morales Conde S, Dal Dosso I, Moretto G, et al, ''Fluorescence-based bowel anastomosis perfusion evaluation: results from the IHU-IRCAD-EAES EURO-FIGS registry'', Surg. Endosc., (2021)

[33] Blanco-Colino R, Espin-Basany E, ''Intraoperative use of ICG fluorescence imaging to reduce the risk of anastomotic leakage in colorectal surgery: a systematic review and meta-analysis'', Tech. Coloproctol., 22, pp. 15–23, (2018)

[34] Chan DKH, Lee SKF, Ang JJ, ''Indocyanine green fluorescence angiography decreases the risk of colorectal anastomotic leakage: Systematic review and meta-analysis'', Surgery, 168, pp. 1128–1137, (2020)

[35] De Nardi P, Elmore U, Maggi G, Maggiore R, Boni L, Cassinotti E, et al, ''Intraoperative angiography with indocyanine green to assess anastomosis perfusion in patients undergoing laparoscopic colorectal resection: results of a multicenter randomized controlled trial'', Surg. Endosc., 34, pp. 53–60, (2020)

[36] Alekseev M, Rybakov E, Shelygin Y, Chernyshov S, Zarodnyuk I, ‘’A study investigating the perfusion of colorectal anastomoses using fluorescence angiography: results of the FLAG randomized’’, trial. Color Dis., 22, pp. 1147–1153, (2020)

[37] Köhler H, Jansen-Winkeln B, Maktabi M, Barberio M, Takoh J, Holfert N, et al, ‘’Evaluation of hyperspectral imaging (HSI) for the measurement of ischemic conditioning effects of the gastric conduit during esophagectomy’’, Surg. Endosc., 33, pp. 3775–3782, (2019)

[38] Jansen-Winkeln B, Germann I, Köhler H, Mehdorn M, Maktabi M, Sucher R, et al, ‘’Comparison of hyperspectral imaging and fluorescence angiography for the determination of the transection margin in colorectal resections—a comparative study’’, Int. J. Colorectal Dis., International Journal of Colorectal Disease, 36, pp. 283–291, (2021)

[39] Vervandier J, Gioux S., ‘’Single snapshot imaging of optical properties’’, Biomed. Opt. Express, 3(4), 2938, (2013)

[40] Dögnitz N, Wagnières G, ‘’Determination of tissue optical properties by steady-state spatial frequency-domain reflectometry’’, Lasers Med. Sci., 13, pp. 55–65, (1998)

[41] Nguyen JT, Lin SJ, Tobias AM, Gioux S, Mazhar A, Cuccia DJ, et al, ‘’A novel pilot study using spatial frequency domain imaging to assess oxygenation of perforator flaps during reconstructive breast surgery’’, Ann. Plast. Surg, 71, pp. 308–315, (2013)

# VII. SSOP imaging for perfusion assessment during gastric conduit creation for esophagectomy

This chapter presents a second study aiming at the validation of SSOP-based oxygenation imaging for blood perfusion assessment. While the previous chapter focused on the small bowel with pure ischemia and ischemia with reperfusion settings, the following study is centered on the stomach ischemia monitoring. Consistently, the $StO_2$ rates measured with SSOP were correlated with lactates measurements to validate the ability of oxygenation imaging to quantify ischemia. A reinforced histological analysis including comprehensive blood gas analysis confirmed the conclusions drawn from the extracted correlations. This second study strengthens the position of oxygenation imaging as an ideal candidate for perfusion assessment.

The clinical need and current standard of care and state-of-the art imaging modalities are first detailed in the context of esophagectomy procedures. The imaging system and protocol used for the study are briefly described as well as the surgical procedure and ischemia assessment workflow, including blood sampling and histological sampling and their respective analysis. The $StO_2$ rates are compared to the extracted lactates and histology scores to validate the performances of oxygenation imaging. Finally, the advantages of SSOP-based oxygenation imaging are discussed.

The material for this chapter was extracted from a previously published contribution: *''Single snapshot imaging of optical properties (SSOP) for perfusion assessment during gastric conduit creation for esophagectomy: An experimental study on pigs''* in Cancers , Volume 13 , Number 23, (2021). [1]

## VII.1. Context and motivation

On a worldwide scale, esophageal cancer is ranked eighth in terms of occurrence among all cancers, making it the sixth most common cause of cancer-related mortality [2]. Multimodal treatment includes surgery, radiotherapy, and chemotherapy. Surgery remains the best curative modality for patients with resectable esophageal cancer [3], although the 5-year survival rate ranges from 5 to 47% [4]. Two-stage Ivor Lewis esophagectomy was described for the first time in 1946 [5], becoming the most frequently performed surgical treatment for esophageal cancers located in the medial, distal, or esophagogastric junction of the esophagus [6]. Following this technique, esophagogastric continuity is restored through the anastomosis between the gastric conduit (GC) obtained from the tubulization of the stomach and the remaining esophagus. One of the most serious complications of this type of surgery is anastomotic leakage, occurring

in up to 53% of all cases [7,8]. It is associated with a mortality rate of up to 35% [9] and with adverse effects on short-term and long-term outcomes [10-12], resulting in an increased recurrence of tumors [13]. Although the etiology of AL is multifactorial [14,15], an insufficient perfusion of the anastomotic site is considered to be a significant and independent predicting factor to determine anastomotic failure [16,17]. Currently, the adequate perfusion of GC is clinically assessed by surgeons using indicators such as serosal color or pulsatile flow of vessels. However, these parameters are subjective and inaccurate to rule out a marginally perfused anastomosis [18]. During the last two decades, several intraoperative optical imaging techniques have been developed and tested to monitor the perfusion of the gastric conduit [19], including laser Doppler flowmetry, near-infrared spectroscopy, laser speckle contrast imaging, infrared thermographic imaging, optical coherence tomography, and ICG fluorescence imaging. However, those methods lack reproducibility and/or provide operator-dependent results and/or lengthen the surgical workflow [20,21]. New technologies based on optical properties including multispectral and hyperspectral imaging are progressively implemented in image-guided surgery. This increased interest can be partly explained by the enhanced ability of those endogenous imaging methods to quantify tissue optical properties in terms of physiology and morphology, allowing for improved and reproducible information during interventions, which can influence the surgical decision-making process [21]. Our group has recently assessed gastric tubulization via hyperspectral imaging (HSI) in a survival study on hybrid ischemic preconditioning of the stomach [22]. Additionally, the feasibility and potential interest of HSI during gastrointestinal surgeries, including esophageal resections, has been recently evaluated in preliminary clinical studies [23–25]. HSI is a contrast-free technology which can provide a chemical quantification of tissue compounds, allowing to quantify tissue oxygen saturation rates, among others. Although HSI showed encouraging and consistent results, its main downside remains the lack of video rate, which greatly limits its usability as a real-time surgical navigation tool. Spatial Frequency Domain Imaging is an optical technique that can provide a 3D corrected profile and quantitative information of optical properties (i.e., absorption and reduced scattering coefficients) of biological tissues over a large field of view [26,27]. The potential of SFDI to provide information related to tissue oxygenation has been demonstrated in the past at both preclinical and clinical levels [28–32]. However, the standard embodiment of SFDI requires several frames to be acquired and it does not provide images in real-time. For this reason, Single Snapshot imaging of Optical Properties was developed to enable a video rate imaging capability in the SFDI, by limiting the number of required frames to only one [33–36]. The natural drawbacks of this single snapshot technique include a loss of image resolution and the presence of edge artifacts. Nevertheless, with the implementation of the latest convolution neural network architectures [36] and the use of state-of-the-art GPU computing, it was possible to achieve significant improvements in the overall image quality and profile correction, while maintaining real-time capabilities [36]. In the present study, our aim is to perform a preliminary validation of SSOP camera to intraoperative quantify serosal $StO_2$% in an experimental gastric conduit (GC) model.

## VII.2. Materials and methods

### VII.2.1. Real-time oxygenation imaging

SFDI is based on the projection of spatially modulated patterns of light on the sample (typically using a DMD system) and on the acquisition with a camera of the diffused backscattered light arising from it. In its simplest configuration, SFDI requires at least six frames: two different spatial frequency patterns (e.g., fx = 0 mm−1 , fx = 0.2 mm−1 ) and three-phase shifts for each of them. The phase-shifted sequence is then used to demodulate the signal, hence obtaining the modulation amplitude maps of the given sample at each spatial frequency [26]. Using a calibration step involving the measurement of a calibration phantom with known optical properties, it is then possible to compute the diffuse reflectance maps, i.e., $R_{DC}$ (fx = 0 mm−1 ) and $R_{AC}$ (fx = 0.2 mm−1 ). Finally, solving the inverse problem using a light propagation model, here a Monte Carlo-based LUT [38] algorithm, allows to retrieve the optical properties of the sample (i.e., absorption and reduced scattering coefficients) for each pixel of the image. Due to the need for at least six frames, SFDI cannot perform in real-time. Instead, SSOP allows to sensibly reduce acquisition time and to reach video rate performances, thanks to a single high spatial frequency frame required to extract the optical properties of the sample. The main difference in the workflow in comparison with SFDI consists of using a Fourier transform-based filtering technique for the demodulation step [34]. After the extraction of the modulation amplitude maps, the processing workflow is the same as for SFDI. It is worth noticing that degradation in image quality and the presence of edge artifacts are the main consequences of the use of a single frame. However, significant improvements have been achieved in recent years by first optimizing the filtering technique [39] and by adopting deep neural network approaches for the demodulation [36]. Additionally, the latest developments on SSOP also account for a tridimensional profile correction of the sample in order to reduce the quantification error of SFDI associated with a variation of light intensity across non-flat sample surfaces [36].

In this study, the latest deep learning optimized SSOP workflow was adopted, as described by Aguénounon et al. [36]. In a nutshell, the standard Fourier domain filtering demodulation was replaced by two dedicated CNNs based on a U-Net architecture as follows: the former was dedicated to the extraction of the modulation amplitude of the signal for each spatial frequency, and the latter was used for the profilometry analysis. Both networks were trained using high quality images obtained with SFDI acquisition sequences (with 7 phase shifts instead of 3 to enhance quantification accuracy and image quality) and optimized for efficient and low-cost computation performances, by reducing the number of parameters and layers involved at a minimum, and subsequently allowing for a real-time high visual quality optical property

quantification for up to 1 MP images. The training dataset consisted of a total of 200 high quality images divided into n = 40 images of tissue-mimicking silicone phantoms with different optical properties ranging from μa = 0.005 to 0.05 mm−1 for absorption and from μ's = 0.5 to 3 mm−1 for reduced scattering; n = 52 images of hands from different Caucasian men and women in various configurations; n = 108 images from ex vivo and in vivo swine organs in several orientations (stomach, small bowel, colon, kidney, pancreas, liver, and spleen).

### VII.2.2. Clinically-compatible imaging system

The imaging system (**Figure VII.1**) included a white light plasma lamp (Thorlabs Inc., Newton, NJ, USA) for the illumination of the surgical field, together with a fiber-coupled custom-made high-power two wavelengths laser source working at 665 and 860 nm. The projection of sinusoidal patterns on the sample was performed with a Digital Micromirror Device-based projector (Vialux GmbH, Chemnitz, Sachsen, Germany). The field-of-view (FOV) of the system was slightly greater than 15 × 15 cm at a working distance of 45 cm as shown in **Figure VII.1**.

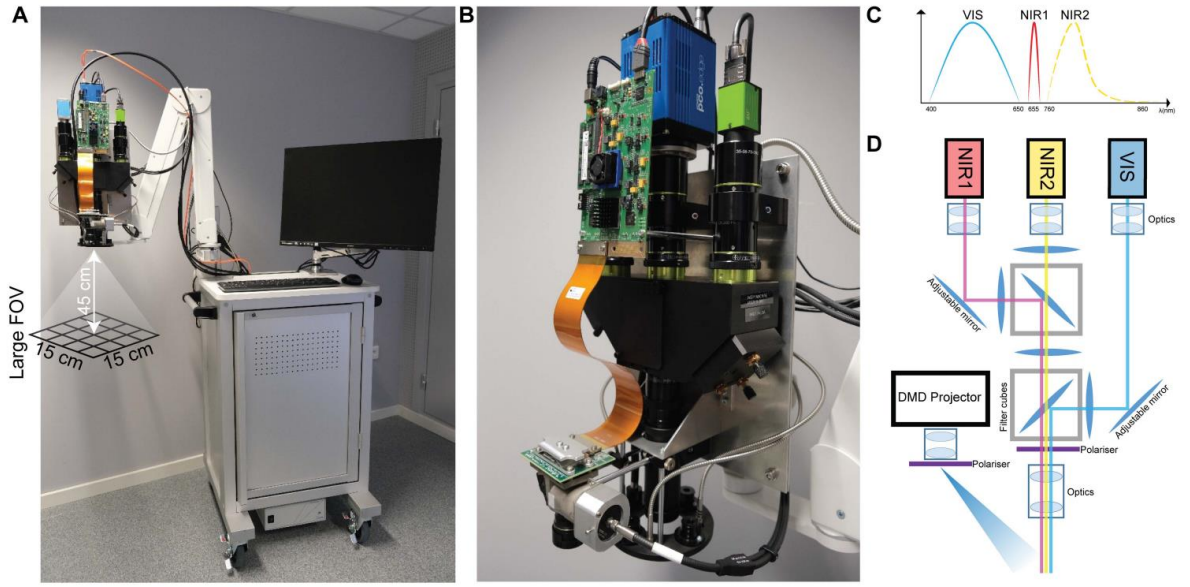


**Figure VII.1 – Clinically-compatible imaging for SSOP-based oxygenation imaging. (A) Preclinical cart for fluorescence, SFDI, and SSOP imaging in the operating room. The imaging head is mounted onto an articulated arm for an easy positioning over the surgical table at the desired working distance. The main body of the cart contains the laser sources, the white light lamp, and the PC workstation. (B) Imaging head based on a trident architecture to enclose three separate channels for RGB, NIR1, and NIR2 imaging. A DMD-based projection system is also mounted onto the head for the generation of structured illumination over the FOV. The light source is delivered to the projector via a fiber-based coupling system. An illumination ring is used to homogeneously deliver white light illumination of the surgical field and fluorescence excitation wavelength. (C) Schematics of the imaging bands for the trident, namely: the RGB camera (JAI GO-5000C-USB, JAI Ltd., Kanagawa, Japan) covers the VIS bandwidth (400–650 nm); the NIR1 camera (pco.pixelfly USB, Excelitas PCO GmbH, Kelheim, Germany) covers the first near-infrared bandwidth (centered around 665 nm); and the NIR2**

**camera (pco.edge 5.5, PCO AG, Excelitas PCO GmbH, Kelheim, Germany) covers the second near-infrared bandwidth (700–900 nm). (D) Schematics of the optical path in the trident for the co-registration of the three imaging channels, together with the configuration of the DMD-based projector. A pair of filtering cubes are used to isolate the NIR1 and NIR2 channels, and a set of mirrors are used to align the FOV of the three cameras.**

The imaging head was based on a 3-channel architecture: 2 near-infrared monochrome cameras (PCO.edge 5.5 and PCO.pixelfly USB, Excelitas PCO GmbH, Kelheim, Germany) were used for the acquisition of the SSOP frames with 1024 × 1280 pixel resolution at 665 and 860 nm, and an RGB camera (JAI GO-5000C-USB, JAI Ltd., Kanagawa, Japan) was also added to record the surgical field (**Figure VII.1**). The co-registration of the scene by the cameras was obtained thanks to a customized optomechanical system in which optical filters were included to separate the 3 channels at the collection side. In addition, a pair of linear polarizers (PPL05C, Moxtek, Orem, UT, USA) were used in crossed configurations at the projection and camera sides to reject the specular reflections originating from the sample surface. The working distance of the imaging system was 45 ± 5 cm, hence offering a comfortable operating condition for the physicians during acquisition. Oxygenation computation was achieved applying Lambert–Beer's law for chromophore absorption inside the biological tissue [40].

### VII.2.3. Animal model and stomach ischemia model

*Animal model*

The present study, which was part of the QuantSURG COLORECTAL project (Imagerie optique quantitative pour le guidage du geste chirurgical dans le cancer colorectal), was approved by the local Ethical Committee on Animal Experimentation (ICOMETH 38.2019.01.121) on 3 September 2019, as well as by the French Ministry of Superior Education and Research (MESR) (APAFIS#20819-2019052411591088v3). All animals used in the experiment were managed according to French laws for animal use and care, and according to the directives of the European Community Council (2010/63/EU) and ARRIVE guidelines [37]. Six adult pigs (Sus scrofa ssp. domesticus, mean weight: 36.5 ± 3.3 kg) were housed and acclimatized for 48 h in an enriched environment, respecting circadian cycles of light–darkness, with constant humidity and temperature conditions. They were fasted 24 h before surgery, with ad libitum access to water, and finally sedated (zolazepam + tiletamine 10 mg/kg IM) 30 min before the procedure in order to decrease stress. Anesthesia was performed intravenously (18-gauge IV catheter in-ear vein) with Propofol 3 mg/kg and maintained with rocuronium 0.8 mg/kg along with inhaled isoflurane 2% via the automatic standard respiratory system. Vital parameters were monitored through a mechanical ventilator machine. Heartbeat was monitored with a pulse oximeter (Mindray PM-60). At the end of the protocol, pigs were euthanized with a lethal dose of Pentobarbital Sodium (40 mg/kg) (Exagon, Axience SAS, Pantin, France).

*Experimental workflow*

Through a median laparotomy, the stomach was prepared leaving only the right gastroepiploic and pyloric vessels for its vascular supply. Gastric vessels were ligated using surgical clips (LIGACLIP Multi-Patient-Use Single Clip Appliers, Ethicon, Endosurgery Inc., Cincinnati, OH, USA). Successively, an approximately 4 cm wide GC was created, starting from the greater curvature, and using a surgical stapler (ENDO GIA™ linear stapler equipped with 45 mm black reloads, Medtronic, Minneapolis, MN, USA) (**Figure VII.2**).

First of all, laparotomy was performed and the GC was prepared. After tubulization, the resected region of the stomach was maintained near the GC, still connected to the esophagus. Four ROIs were manually selected as follows: ROI-A (antrum), ROI-C (greater curvature/corpus), ROI-F (fundic region/future anastomotic site), and ROI-R (the resected upper part of the stomach). The post-procedural observational phase was held for 60 min, at 15 min time points (T0, T15, T30, T45, and T60). Following this timeline, for each ROI, the SSOP system was used to detect $StO_2$% values and local capillary lactates (LCL) were measured as biological "ground truth", together with systemic blood gas analysis (BGA). At the end of the 60 min observation period, histopathological evaluation and scoring were performed in the same four ROIs. Each animal served as its own control. The study aimed to predict gastric conduit viability through the analysis of SSOP images in order: (i) to recognize perfused from non-perfused stomach, using ROI-R as ischemic control, (ii) to predict the level of gastric perfusion during the postoperative phase, and (iii) to predict biological data. The hypercube extracted from SSOP images was used to train two CNNs. Finally, the generated artificial intelligence (AI) score for the postoperative phase was generated and the quantitative analysis of SSOP images was correlated with biological and histopathological data (**Figure VII.2**).

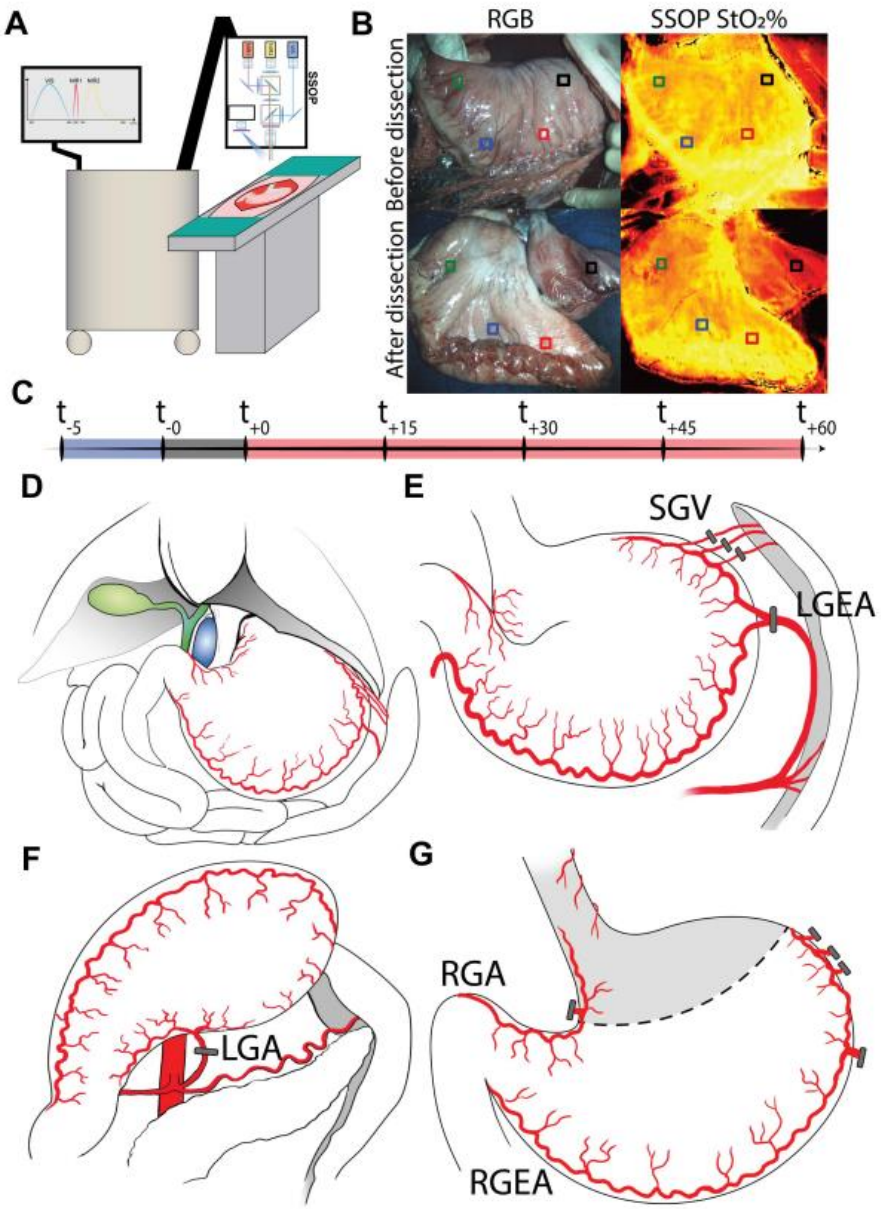


**Figure VII.2 – SSOP imaging experimental workflow. (A) First of all, the SSOP machine was prepared for data acquisition. (B) Regions of interest (ROIs) were marked with surgical stitches before any dissection in order to obtain $StO_2$% values and correspondent LCLs in the same ROIs along the entire timeline. Preselection of ROIs for antrum (ROI-A), corpus (ROI-C), fundus (ROI-F), and the future removed region (ROI-R) was essential to prevent any possible selection bias related to postoperative selection. (C) The acquisition of data started 5 min before the preparation of the gastric conduit (t–5 ), with the baseline evaluation of the healthy stomach. After gastric conduit (GC) formation, the acquisition proceeded in 15 min time points, for a total of 60 min, which was the clinical estimated time between GC preparation and the packing of the esophagogastric anastomosis. During this period, the upper separated part of the stomach (ROI-R) was supposed to become increasingly ischemic after resection. (D) Normal porcine abdominal anatomy. Gastric vascularization is the same in humans, even if the stomach of the pig is two to three times larger and more bag-shaped. The vena cava (blue) and the biliary tree (green) are highlighted. (E) Ligation of the left gastroepiploic artery (LGEA) and short gastric vessels (SGV). (F) Ligation of the left gastric artery (LGA). (G) After transection, the perfusion of the gastric conduit was maintained via the right gastroepiploic arcade (RGEA); the antrum/duodenum was also perfused by the right gastric artery (RGA). ROI-R, even if partially perfused by distal esophageal vessels, received only a minimum amount of blood, enough to consider it ischemic, but not totally devascularized.**

## VII.2.4. Tissue viability assessment: blood sampling and histology analysis

*Blood gas analysis*

LCLs were obtained through a full-thickness puncture of the gastric wall, in correspondence with the preselected ROIs. A blood drop was obtained and a portable strip-based lactate analyzer (EDGE, Apex Bio, Taipei, Taiwan) was used to quantify LCL levels, with a margin error of 0.35 mmol/L. The correlation analysis of data was performed between $StO_2$% parameters detected via the SSOP system and LCLs concentration. Systemic blood was sampled through a central catheter placed in the right external jugular vein (6 French IV catheter) and evaluated through a handheld wireless blood tester (Epoc® Blood Analysis System, Siemens Healthcare GmbH, Erlangen, Germany). These systemic BGA were used to monitor the surgical intervention to rule out any bias in the post-procedural observation of the GC. BGA measured pO2, pCO2, pH, base excess, bicarbonate, hemoglobin, hematocrit, glucose, creatinine, urea, BUN, electrolyte, and lactates.

*Histology analysis*

A first gastric full-thickness biopsy was taken before the surgical procedure as healthy control. This control biopsy (CB) was removed from the posterior side of the future removed region of the stomach while the other four biopsies were collected in the selected ROIs 60 min after the GC formation. Sections of 5 µm were taken from formalin-fixed paraffin-embedded blocks and were dewaxed and rehydrated before staining at room temperature. A treatment with a hematoxylin Harris formula (Leica Biosystems, Nussloch GmbH, Heidelberg, Germany) for 10 min and then a wash with acid alcohol for 2 s and tap water for 2 min were performed. Eosin staining with Eosin 0.5% (Leica Biosystems) for 3 min was performed before washing with tap water for 30 s. Finally, the sections were dehydrated with ethanol 100% and placed in xylene until their mounting with coverslips. A semi-quantitative blinded analysis was performed by an expert pathologist using the following score and variables: necrosis, neutrophils infiltration, and congestion, with a score from 0 to 3 (none, mild, moderate, and severe, respectively).

*Sample size calculation*

Sample size calculation was performed using the correlation between optical and biological data. The calculation derived from previous publications on bowel ischemia, which showed a ρ correlation coefficient of −0.7 [24,25]. The required sample size in terms of paired values was 4, considering $\alpha = 0.05$ with power $(1 - \alpha) = 0.9$. In the present study, 120 paired values of $StO_2$% and lactates values were obtained in a total of 6 pigs.

*Statistical analysis*

Statistics were performed using GraphPad 8.3 (GraphPad Software, San Diego, CA, USA). A Pearson's rho was analyzed to perform the correlation between optical and biological data. All data were expressed as means ± standard error (SEM). One-way and Cancers 2021, 13, 6079 8 of 15 two-way ANOVA with Dunnett's

multiple comparisons were performed for parametric tests to calculate differences in continuous paired variables. A two-tailed p-value < 0.05 was considered statistically significant. Principal component analysis (PCA) was used to cluster the population of data from 4 ROIs. $StO_2$% and LCL variables were used for the analysis. The PCA method was based on pre-standardization of the data with the largest eigenvalues. Finally, data were labeled as from the experimental design (ROI-A, ROI-C, ROI-F, and ROI-R).

## VII.3. Results

### VII.3.1. *In-vivo* oxygenation imaging outcome

*$StO_2$ quantification*

SSOP images of $StO_2$% are shown in **Figure VII.3**. ROI-A had no differences in terms of $StO_2$% for each time point. Instead, ROI-C showed statistically significant lower T0 values than T45 (1.00 ± 0.03 vs. 1.08 ± 0.01, p = 0.0334) and T60 (1.00 ± 0.03 vs. 1.13 ± 0.01, p = 0.0010). Regarding ROI-F, $StO_2$% at T0 remained significantly lower when compared to T15, T30, T45, and T60 values (p = 0.0012, p = 0.0080, p = 0.0181, p = 0.0049, respectively). Regarding ROI-R, $StO_2$% was statistically higher at T0 when compared to T15, T30, T45, and T60 (p < 0.0001) (**Figure VII.3**). $StO_2$% curves of all pigs are available in **Figure A1.3**. The comparison between different ROIs showed no differences for T0. ROI-R had statistically significant lower $StO_2$% values when compared to all other ROIs at T15, T30, T45, and T60 (p < 0.0001). However, ROI-C and ROI-F showed higher values than ROI-A at T15 (ROI-C vs. ROI-A, p = 0.0007; ROI-F vs. ROI-A, p < 0.0001), T30 (p < 0.0001), T45 (p < 0.0001), and T60 (p < 0.0001) (**Figure VII.3, Table A1.4**).

### VI.3.2. Capillary lactates and oxygenation correlation

*Local capillary lactates quantification*

Mean LCL values were not significantly different between the four ROIs at T0, upon the formation of the GC, as expected. ROI-A had similar LCLs for each time point, while ROI-C and ROI-F showed significant differences in terms of T0 vs. T15 (1.00 ± 0.28 mmol/L vs. 1.54 ± 0.18 mmol/L, p = 0.0307) and T0 vs. T60 (1.00 ± 0.24 mmol/L vs. 1.53 ± 0.22 mmol/L, p = 0.0451) respectively. Regarding ROI-R, LCL levels obtained at T15, T30, T45, and T60 were statistically significantly higher than T0 (p < 0.0001) (**Figure VII.3**).

The comparison performed between different ROIs showed that mean lactate levels collected at ROI-A were significantly lower than those sampled at ROI-R at T15 (0.95 ± 0.24 mmol/L vs. 5.31 ± 0.89 mmol/L, p =

0.0091), T30 (1.06 ± 0.15 mmol/L vs. 6.44 ± 0.56 mmol/L, p = 0.0003), T45 (1.25 ± 0.17 mmol/L vs. 6.91 ± 0.69 mmol/L, p = 0.0007), and T60 (1.02 ± 0.20 mmol/L vs. 9.11 ± 0.76 mmol/L, p = 0.0002) (**Figure VII.3**). The same statistical relationship was shown by ROI-C and ROI-F when compared to ROI-R. Instead, lactate levels were not significantly different between ROI-A vs. ROI-C, ROI-A vs. ROI-F, and ROI-C vs. ROI-F (**Figure VII.3**). LCLs were standardized for ROI-A lactate values at T0. Statistical analysis is reported in **Table A1.3**.

*Correlation between $StO_2$ and LCLs*

LCL values were normalized for LCL measurements of ROI-A at T0. Principal component analysis of $StO_2$% and LCL values after resection showed ROI-R as a separated cluster from the other ROIs. ROI-A and ROI-F appeared as separate groups while ROI-C was overlapped between ROI-A and ROI-F (**Figure VII.3**). Similarly, data were normalized for ROI-A at T60 to investigate the power of the camera in discriminating between ROIs. As a result, measurements evaluated at ROI-A showed statistically significant differences when compared to ROI-C (p = 0.0013), ROI-F (p = 0.0028), and ROI-R (p < 0.0001). A significant difference was found for ROI-C vs. ROI-R (p < 0.0001) and ROI-F vs. ROI-R (p < 0.0001) while no difference was found regarding ROI-C vs. ROI-F (**Figure VII.3**). A simple logistic regression analysis was used to find the cut-off value to discriminate ROI-A from ROI-C and ROI-C from ROI-F. The threshold value to discriminate between ROI-C and ROI-F was 72.21%, with an AUC of 0.7274 (95% CI 0.5847 to 0.8702, p = 0.0069) (**Figure VII.3**) while the threshold value to distinguish between ROI-A and ROI-C was found to be 65.21%, with an AUC of 0.9688 (95% CI 0.9275 to 1.0000, p < 0.0001) (**Figure VII.3**). $StO_2$% and LCLs were found to be negatively correlated (R = −0.8439, 95% CI −0.9367 to −0.6407, p < 0.0001) (**Figure VII.3**).

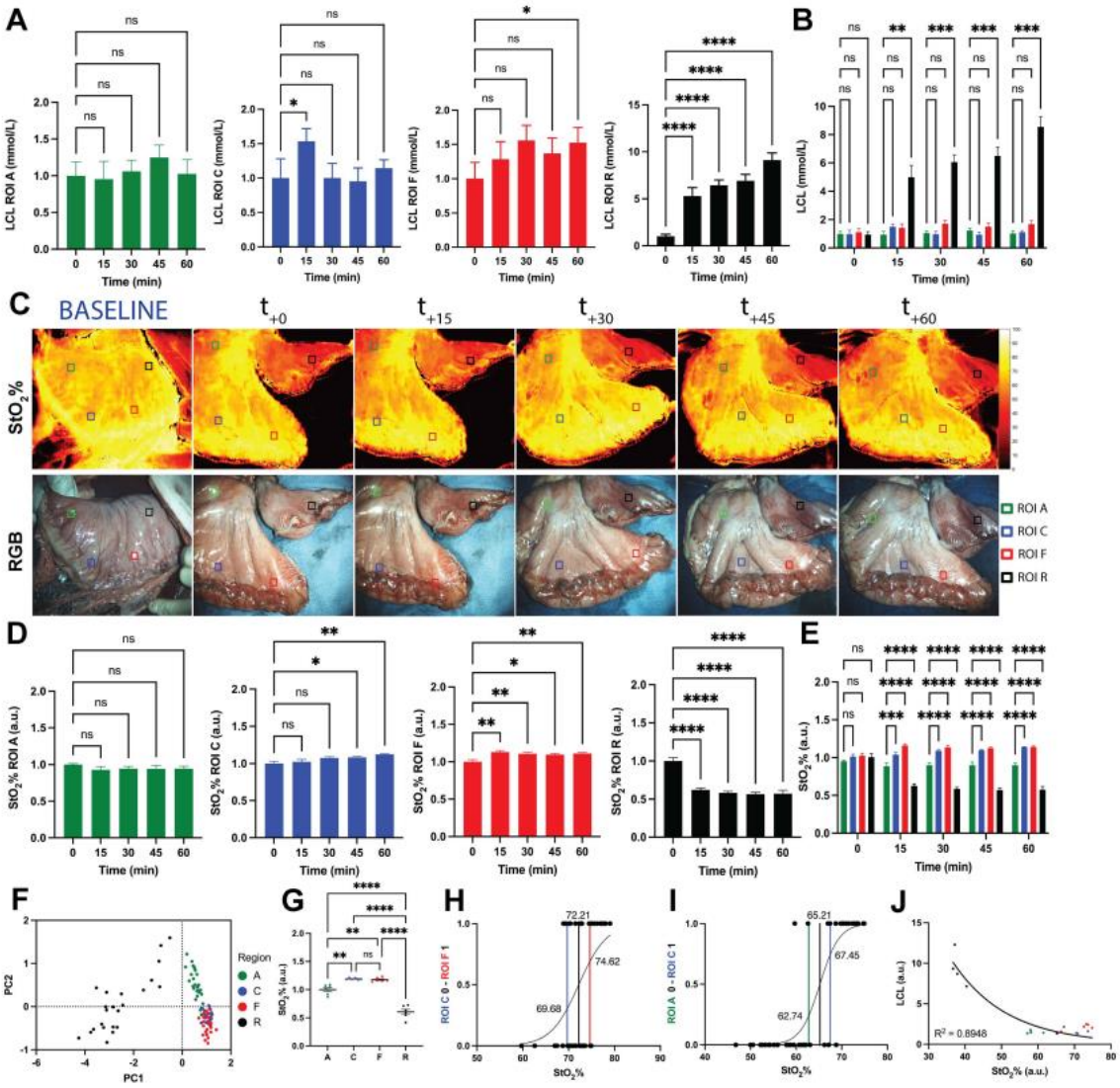


**Figure VII.3 – LCLs and $StO_2$% quantification and analysis. Different colors indicate different ROIs: green (ROI-A), blue (ROI C), fundus (ROI-F), and black (ROI-R). (A) Evolution of LCLs for single ROIs. Only the removed region showed statistically significantly higher values of LCLs for each time point from T15 to T60 when compared to T0; the corpus showed this relationship for T0 vs. T15 and the fundus for T0 vs. T60. Data were normalized for T0 of ROI-A. (B) LCL comparison between ROIs. After gastric conduit formation, the removed region showed statistically significantly higher values of LCLs when compared to the other gastric regions. Data were normalized for T0 of ROI-A. (C) SSOP images showing $StO_2$% of the gastric conduit and the removed region from baseline to T60, and correspondent true color (RGB) images. (D) Oxygenation trends for each region of interest during the full ischemic period with a non-constant sampling rate. Between T0 (when the GC is complete) and T15, the sampling rate is around 10 s to monitor the dynamics of tissue perfusion, whereas for t = −5 min (baseline) and T30, T45, and T60, a single point was sampled. Data were normalized for T0 of ROI-A. (E) Evolution of $StO_2$% for single ROIs. $StO_2$% increased along time in the corpus (T45 and T60) and fundus (T15, T30, T45, and T60). Instead, as expected, $StO_2$% values at T15, T30, T45, and T60 were lower than T0. Data were normalized for T0 of ROI-A. (F) Principal component analysis of the ROIs. The variables selected are LCL and $StO_2$% and the label used is the ROI (A, C, F, R). ROI-R represents a separate cluster from the other ROIs. Principal Component (PC)1 and PC2 contribute to 94.83% of the variance. (G) $StO_2$% comparison between ROIs. After GC formation, the removed region showed lower $StO_2$% values than other gastric districts. Instead, $StO_2$% of the antrum appeared lower when compared to the corpus and fundus. Data were normalized for T0 of ROI-A. (H) Simple logistic regression analysis between ROI-A and ROI-F. (I) Simple logistic regression analysis between ROI-A and ROI-C. (J) Pearson's correlations between LCL and $StO_2$%. Higher LCL measurements correlated with lower $StO_2$% values. Data were extracted at T60 and normalized for the respective ROI-A. All**

**data are expressed as mean and ± SEM. For every statistical analysis, a two-tailed p-value < 0.05 was considered significant. One-way ANOVA was used, ns p > 0.05, * p ≤ 0.05, ** p ≤ 0.01, *** p ≤ 0.001, **** p ≤ 0.0001. N = 6.**

### VII.3.3. Histologic analysis

*Blood gas analysis*

The systemic blood gas analysis supported the consistency of the experimental workflow and the healthy condition of pigs, showing only minimal changes over time when compared to T0. The full dataset and comparison are available in **Table A1.1**.

*Histologic analysis*

Histological analysis of the biopsies of the selected ROIs showed a progressive alteration of the cell morphology of the gastric wall layers. This aspect was more evident in the mucosa, characterized by superficial erosions and strong congestion, edema, and inflammatory components such as neutrophils and eosinophils, especially in ROI-R (removed region). Muscularis mucosae presented light and homogeneous alterations due to inflammation. Edema and congestion were present in the submucosae, while in ROI-R the muscularis externa presented a higher inflammatory infiltration which involved the serosa too. Nevertheless, the serosa showed no important alteration between ROIs (**Figure VII.4**). Control biopsies are available in **Figure A1.1**. Overall, histological alterations have grown gradually from ROI-A (antrum), ROI-C (corpus), and ROI-F (fundus) up to ROI-R. Statistical analysis was reported in **Table A1.2**. After 60 min of ischemia, the serosa showed non-statistically significant alterations in all ROIs (**Figure VII.4**). The muscularis externa presented a significantly higher damage in ROI-C and ROI-R when compared to ROI-A ($p = 0.0004$, $p = 0.0373$, respectively). The submucosa showed a statistically significantly higher histological alteration, mostly due to inflammation in ROI-F and ROI-R ($p = 0.0013$, $p = 0.0073$, respectively), while the mucosa showed an increased and significant damage in ROI-C and ROI-R ($p = 0.0211$, $p = 0.0004$, respectively). The average of the full-thickness biopsy damage presented a statistically significant increase going from ROI-A to ROI-C ($p = 0.0010$), ROI-F ($p = 0.0187$), and ROI-R ($p = 0.0003$), accordingly with the histopathological observation. Additional analysis on neutrophils infiltration is reported in **Figure A1.2**.

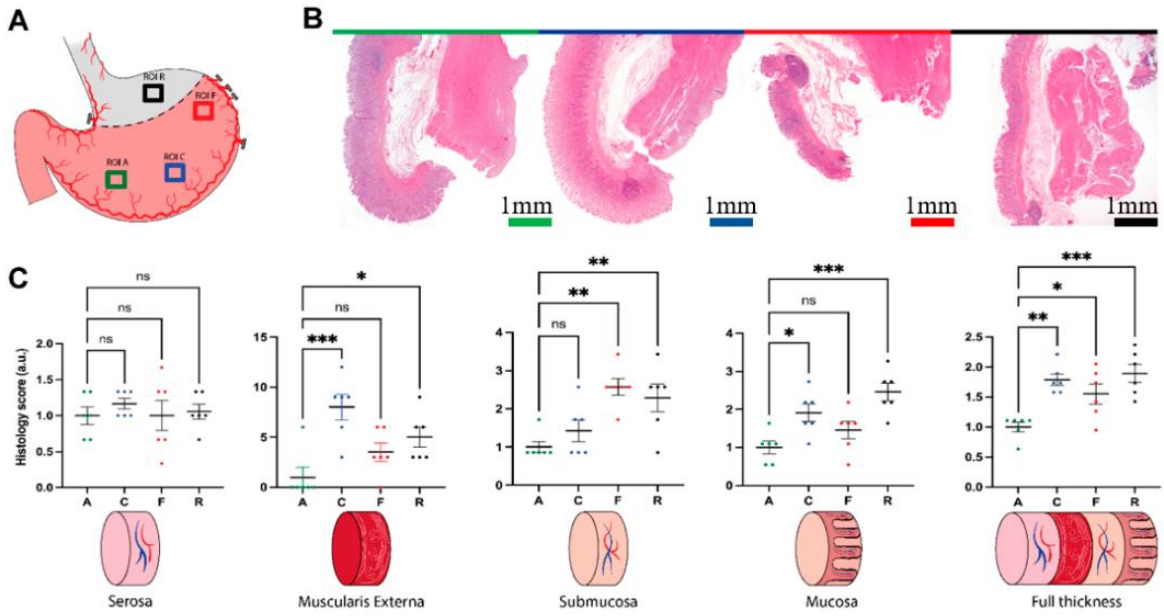


**Figure VII.4 – Histopathological assessment. (A) ROIs localization map. (B) Hematoxylin and eosin staining of biopsies of all ROIs 60 min after tubulization, green (antrum, ROI-A), blue (corpus, ROI-C), red (fundus–future anastomotic site, ROI-F), black (resected region, ROI-R). Magnification 0.125×. Scale bar 1 mm. Pictures were sampled using microscope Zeiss AXIO scope A1. (C) Statistical analysis of the histology score, per single layer, and full-thickness. Data were expressed as mean and ±SEM and normalized with the antrum dataset. One-way ANOVA was used, ns $p > 0.05$, * $p \leq 0.05$, ** $p \leq 0.01$, *** $p \leq 0.001$ N = 6.**

## VII.4. Discussion

In the current experimental study, the SSOP imaging system was used to evaluate $StO_2$% values corresponding to selected ROIs, using the resected upper part of the stomach (ROI-R) as ischemic control. ROI-R showed lower $StO_2$% values when compared to other ROIs. Interestingly, the corpus and fundus maintained $StO_2$% values higher than the antrum, probably due to the inflammatory process activated during the manipulation of the stomach. Gastric manipulation, the sequential ligation of vessels and the division of the stomach, are factors which can affect the physiology of healthy gastric tissue. Akiyama et al. [41] already described that the formation of the gastric conduit induces severe changes in microcirculation, particularly in the anastomotic region of the gastric fundus. As a result of this manipulation, immune cells promote the acute inflammatory response by increasing the permeability of vessels and allowing the secretion of various cytokines and chemokines. Neutrophils are the first ones to be involved, by secreting vasoactive and pro-inflammatory mediators, including histamine, platelet-activating factors (PAFs), bradykinin, and thrombin. These mediators increase vascular permeability, promoting fluid accumulation (edema) and leukocyte extravasation (**Figure A1.2**). Polymorphonuclear neutrophils produce reactive oxygen species (ROS), responsible for endothelial dysfunction by oxidation of crucial cellular signaling proteins such as tyrosine phosphatases [42]. The presence of ROS together with the increased permeability

of vessels could account for higher $StO_2$% values detected by the present experimental model, reflecting the growing trend of inflammation along time and from the antrum to the fundus. As described above, inflammation is part of the regular process of healing. However, persistent inflammation led to excessive quantities of pro-inflammatory macrophages, whereas the number of macrophages with anti-inflammatory phenotypes became lower. As a result, the establishment of a highly inflammatory environment with an overabundance of inflammatory mediators promotes the degradation of the extracellular matrix, preventing anastomotic healing [43]. The $StO_2$% values provided by means of SSOP negatively correlated with LCL values, confirming the biological validity of the method. Instead, no correlation was found between $StO_2$% and the histopathologic analysis. The limited period of ischemia (60 min), together with the residual perfusion of ROI-R from esophageal vessels, were probably accountable for non-significant histological changes in the gastric tissue. Nevertheless, this time frame is consistent since it is similar to the time between GC formation and the packing of the esophagogastric anastomosis in the Ivor Lewis procedure performed in humans. The use of HSI and a system called HYPER (HYperspectral-based Enhanced Reality) was previously described to assess $StO_2$% and intraoperatively localize preselected ROIs during esophagectomy [44], small bowel ischemia [25], and hepatectomy [45]. HYPER allowed to compare HSI to LCLs and mucosal scan with confocal laser endomicroscopy (CLE) on the same ROI [44] with high accuracy. However, the time currently necessary for HSI acquisition is around 10 s and still not yet fully "real-time". Instead, fluorescence angiography with ICG allows for the real-time visualization of tissue vascularization, showing promising results for the evaluation of perfusion in numerous surgical procedures, hence leading to modifications in the surgical strategy and consequently to a decrease in the rates of AL [46,47]. However, the ICG interpretation is subjective while the quantitative evaluation of ICG is a widely unexplored field. In addition, serious adverse events after intravenous application of ICG are described, such as anaphylactic shock, up to sudden deaths in very rarely reported cases [48]. Several other methods for perfusion assessment are reported in the literature. However, they lack in terms of quantitative parameters, provide arbitrary perfusion units, and are influenced with vascular heterogeneity [19]. As a result, non-invasiveness, the absence of adverse events, quantification properties, and the video rate acquisition of the SSOP technology are advantages worthy of being highlighted. The real-time imaging capabilities of SSOP have already been demonstrated [40]. However, the configuration used for the present experiment did not allow to reach minimum requirements required for high frame rate acquisitions. It was due to the high integration times required on the imaging side (>100 ms). Further development of the laser sources has already been started to achieve better performance on the illumination side, hence allowing shorter exposure times during acquisitions in the next experimental steps. Additionally, the potential SSOP system's ability to detect and quantify inflammation could make this new technology a useful tool to screen suffering tissues that are more likely to develop delayed anastomotic healing, moving beyond the concept of perfusion alone. The main limitations of this study lie in the animal model, the very limited sample size, and the acute nature of the experiment. In addition, the absence of gold standard values of tissue oxygenation and

inflammation makes it difficult to compare SSOP with other methods. Finally, SSOP has not yet been adapted to endoscopic systems, resulting in a lack of potential usefulness for an increasingly widespread minimally invasive surgery (MIS). Actually, a prototype based on a laparoscopic surgical instrument is being developed to bring SSOP to MIS, and it is soon going to be ready for validation via pre-clinical trials on other swine models.

## VII.5. Conclusion

The present study has demonstrated for the first time the safety and reliability of SSOP technology in determining the real-time adequate perfusion of GC when compared to a certain ischemic gastric tissue, providing a quantitative evaluation through $StO_2$% values, without exogenous fluorophores. SSOP is a suitable intraoperative tool which could potentially predict AL in the clinical setting. This preliminary validation provided a robust dataset useful to compare single snapshot images with the video rate as the next experimental step. Further studies are needed to validate the system and to develop a minimally invasive setup, to finally proceed to clinical application.

Chapters V, VI and VII demonstrated the use of the presented imaging platform for tissue blood perfusion assessment in the context of reconstructive surgery, by enabling widefield oxygenation and fluorescence imaging in real-time. In the next chapter, the use of the imaging device for tumor resection is studied, by combining fluorescence imaging of targeted agents and endogenous tissue optical characterization to achieve quantitative fluorescence imaging.

**References**


[1] Cinelli L., Felli E., Baratelli L., Ségaud S., Baiocchini A., Okamoto N., Rodriguez-Luna M., Elmore U., Rosati R., Partelli S., Marescaux J., Gioux S., Diana M., ''Single snapshot imaging of optical properties (SSOP) for perfusion assessment during gastric conduit creation for esophagectomy: An experimental study on pigs'', Cancers, 13(23), (2021)

[2] Sung, H., Ferlay, J., Siegel, R.L., Laversanne, M., Soerjomataram, I., Jemal, A., Bray, F., ''Global cancer statistics 2020: GLOBOCAN estimates of incidence and mortality worldwide for 36 cancers in 185 countries'', CA Cancer J. Clin., 71, pp. 209–249, (2021)

[3] van Hagen, P., Hulshof, M.C., van Lanschot, J.J., Steyerberg, E.W., van Berge Henegouwen, M.I., Wijnhoven, B.P., Richel, D.J., Nieuwenhuijzen, G.A., Hospers, G.A., Bonenkamp, J.J., et al., ''Preoperative chemoradiotherapy for esophageal or junctional cancer'', N. Engl. J. Med. 366, pp. 2074–2084. (2012)

[4] Cancer.Net. Esophageal Cancer. Cancer.Net. 2019. Available online: https://www.cancer.net/cancer-types/esophageal-cancer/

[5] Lewis, I., ''The surgical treatment of carcinoma of the oesophagus, with special reference to a new operation for growths of the middle third'', Br. J. Surg., 34, pp.18–31, (1946)

[6] Huang, L., Onaitis, M., ''Minimally invasive and robotic Ivor Lewis esophagectomy'', J. Thorac. Dis., 6 (Suppl. S3), pp. 314–321, (2014)

[7] Liesenfeld, L.F., Sauer, P., Diener, M.K., Hinz, U., Schmidt, T., Müller-Stich, B.P., Hackert, T., Büchler, M.W., Schaible, A., '' Prognostic value of inflammatory markers for detecting anastomotic leakage after esophageal resection'', BMC Surg., 20(324), (2020)

[8] Schaible, A., Brenner, T., Hinz, U., Schmidt, T., Weigand, M., Sauer, P., Büchler, M.W., Ulrich, A., ''Significant decrease of mortality due to anastomotic leaks following esophageal resection: Management makes the difference'', Langenbeck's Arch. Surg., 402, pp. 1167–1173, (2017)

[9] Low, D.E., ''Diagnosis and management of anastomotic leaks after esophagectomy'', J. Gastrointest. Surg. Off. J. Soc. Surg. Aliment. Tract, 15, pp. 1319–1322. (2011)

[10] Jessen, M., Nerstrøm, M., Wilbek, T.E., Roepstorff, S., Rasmussen, M.S., Krarup, P.M., ''Risk factors for clinical anastomotic leakage after right hemicolectomy'', Int. J. Colorectal Dis, 31, pp. 1619–1624, (2016)

[11] Kofoed, S.C., Calatayud, D., Jensen, L.S., Jensen, M.V., Svendsen, L.B., '' Intrathoracic anastomotic leakage after gastroesophageal cancer resection is associated with reduced long-term survival'', World J. Surg., 38, pp. 114–119, (2014)

[12] Chadi, S.A., Fingerhut, A., Berho, M., DeMeester, S.R., Fleshman, J.W., Hyman, N.H., Margolin, D.A., Martz, J.E., McLemore, E.C., Molena, D., et al., ''Emerging Trends in the Etiology, Prevention, and Treatment of Gastrointestinal Anastomotic Leakage'', J. Gastrointest. Surg. Off. J. Soc. Surg. Aliment. Tract, 20, pp. 2035–2051, (2016)

[13] Booka, E., Takeuchi, H., Suda, K., Fukuda, K., Nakamura, R., Wada, N., Kawakubo, H., Kitagawa, Y., ''Meta-analysis of the impactof postoperative complications on survival after oesophagectomy for cancer'', BJS Open, 2, pp. 276–284. (2018)

[14] Trencheva, K., Morrissey, K.P., Wells, M., Mancuso, C.A., Lee, S.W., Sonoda, T., Michelassi, F., Charlson, M.E., Milsom, J.W., ''Identifying important predictors for anastomotic leak after colon and rectal resection: Prospective study on 616 patients'', Ann. Surg., 257, pp. 108–113, (2013)

[15] Chioreso, C., Del Vecchio, N., Schweizer, M.L., Schlichting, J., Gribovskaja-Rupp, I., Charlton, M.E., ''Association Between Hospitaland Surgeon Volume and Rectal Cancer Surgery Outcomes in Patients with Rectal Cancer Treated Since 2000: SystematicLiterature Review and Meta-analysis'', Dis. Colon Rectum, 61, pp. 1320–1332, (2018)

[16] Mitchell, J.D., ''Anastomotic leak after esophagectomy'', Thorac. Surg. Clin., 16, pp. 1–9, (2006)

[17] Ryan, C.E., Paniccia, A., Meguid, R.A., McCarter, M.D., ''Transthoracic Anastomotic Leak After Esophagectomy: Current Trends'', Ann. Surg. Oncol., 24, pp. 281–290, (2017)

[18] Karliczek, A., Harlaar, N.J., Zeebregts, C.J., Wiggers, T., Baas, P.C., van Dam, G.M., ''Surgeons lack predictive accuracy foranastomotic leakage in gastrointestinal surgery'', Int. J. Colorectal Dis., 24, pp. 569–576, (2009)

[19] Jansen, S.M., de Bruin, D.M., van Berge Henegouwen, M.I., Strackee, S.D., Veelo, D.P., van Leeuwen, T.G., Gisbertz, S.S., ''Optical techniques for perfusion monitoring of the gastric tube after esophagectomy: A review of technologies and thresholds'', Dis. Esophagus Off. J. Int. Soc. Dis. Esophagus, 31, (2018)

[20] Urbanavi˘cius, L., Pattyn, P., de Putte, D.V., Venskutonis, D., ''How to assess intestinal viability during surgery: A review of techniques'', World J. Gastrointest. Surg., 3, pp. 59–69, (2011)

[21] Clancy, N.T., Jones, G., Maier-Hein, L., Elson, D.S., Stoyanov, D., ''Surgical spectral imaging'', Med. Image Anal., 63, 101699, (2020)

[22] Barberio, M., Felli, E., Pop, R., Pizzicannella, M., Geny, B., Lindner, V., Baiocchini, A., Jansen-Winkeln, B., Moulla, Y., Agnus, V., et al., ''A Novel Technique to Improve Anastomotic Perfusion Prior to Esophageal Surgery: Hybrid Ischemic Preconditioning of the Stomach. Preclinical Efficacy Proof in a Porcine Survival Model'', Cancers, 12, 2977, (2020)

[23] Jansen-Winkeln, B., Germann, I., Köhler, H., Mehdorn, M., Maktabi, M., Sucher, R., Barberio, M., Chalopin, C., Diana, M., Moulla, Y., et al., Comparison of hyperspectral imaging and fluorescence angiography for the determination of the transection margin in colorectal resections-a comparative study'', Int. J. Colorectal Dis., 36, pp. 283–291, (2021)

[24] Barberio, M., Felli, E., Seyller, E., Longo, F., Chand, M., Gockel, I., Geny, B., Swanström, L., Marescaux, J., Agnus, V., et al., ''Quantitative fluorescence angiography versus hyperspectral imaging to assess bowel ischemia: A comparative study in enhanced reality'', Surgery, 168, pp. 178–184, (2020)

[25] Barberio, M., Longo, F., Fiorillo, C., Seeliger, B., Mascagni, P., Agnus, V., Lindner, V., Geny, B., Charles, A.L., Gockel, I., et al, ''HYPerspectral Enhanced Reality (HYPER): A physiology-based surgical guidance tool'', Surg. Endosc., 34, pp. 1736–1744, (2020)

[26] Cuccia, D.J., Bevilacqua, F., Durkin, A.J., Ayers, F.R., Tromberg, B.J., ''Quantitation and mapping of tissue optical properties using modulated imaging'', J. Biomed. Opt., 14, 024012, (2009)

[27] Gioux, S., Mazhar, A., Cuccia, D.J., ''Spatial frequency domain imaging in 2019: Principles, applications, and perspectives'', J. Biomed. Opt., 24, 071613, (2019)

[28] Ponticorvo, A., Burmeister, D.M., Yang, B., Choi, B., Christy, R.J., Durkin, A.J., ''Quantitative assessment of graded burn wounds in a porcine model using spatial frequency domain imaging (SFDI) and laser speckle imaging (LSI) '', Biomed. Opt. Express, 5, pp. 3467–3481, (2014)

[29] Pharaon, M.R., Scholz, T., Bogdanoff, S., Cuccia, D., Durkin, A.J., Hoyt, D.B., Evans, G.R.D., ''Early detection of complete vascular occlusion in a pedicle flap model using quantitative [corrected] spectral imaging'', Plast. Reconstr. Surg., 126, pp. 1924–1935, (2010)

[30] Gioux, S., Mazhar, A., Lee, B.T., Lin, S.J., Tobias, A.M., Cuccia, D.J., Stockdale, A., Oketokoun, R., Ashitate, Y., Kelly, E., et al., ''First-in-human pilot study of a spatial frequency domain oxygenation imaging system'', J. Biomed. Opt., 16, 086015, (2011)

[31] Yafi, A., Muakkassa, F.K., Pasupneti, T., Fulton, J., Cuccia, D.J., Mazhar, A., Blasiole, K.N., Mostow, E.N., ''Quantitative skin assessment using spatial frequency domain imaging (SFDI) in patients with or at high risk for pressure ulcers'', Lasers Surg. Med., 49, pp. 827–834, (2017)

[32] Rohrbach, D.J., Muffoletto, D., Huihui, J., Saager, R., Keymel, K., Paquette, A., Morgan, J., Zeitouni, N., Sunar, U., ''Preoperative mapping of nonmelanoma skin cancer using spatial frequency domain and ultrasound imaging'', Acad. Radiol., 21, 263–270, (2014)

[33] Vervandier, J., Gioux, S., ''Single snapshot imaging of optical properties'', Biomed. Opt. Express, 4, pp. 2938–2944, (2013)

[34] van de Giessen, M., Angelo, J.P., Gioux, S., ''Real-time, profile-corrected single snapshot imaging of optical properties'', Biomed. Opt. Express, 6, pp. 4051–4062, (2015)

[35] Schmidt, M., Aguénounon, E., Nahas, A., Torregrossa, M., Tromberg, B.J., Uhring, W., Gioux, S., ''Real-time, wide-field, and quantitative oxygenation imaging using spatiotemporal modulation of light'', J. Biomed. Opt. 2019, 24, pp. 1–7, (2019)

[36] Aguénounon, E., Smith, J.T., Al-Taher, M., Diana, M., Intes, X., Gioux, S, ''Real-time, wide-field and high-quality single snapshot imaging of optical properties with profile correction using deep learning'', Biomed. Opt. Express, 11, pp. 5701–5716, (2020)

[37] Kilkenny, C., Browne, W., Cuthill, I.C., Emerson, M., Altman, D.G., NC3Rs Reporting Guidelines Working Group, ''Animal research: Reporting in vivo experiments: The ARRIVE guidelines'', Br. J. Pharmacol, 160, pp. 1577–1579, (2010)

[38] Angelo, J., Vargas, C.R., Lee, B.T., Bigio, I.J., Gioux, S., ''Ultrafast optical property map generation using lookup tables'', J. Biomed.Opt, 21, 110501, (2016)

[39] Aguénounon, E., Dadouche, F., Uhring, W., Gioux, S., ''Single snapshot of optical properties image quality improvement using anisotropic two-dimensional windows filtering'', J. Biomed. Opt., 24, 071611, (2019)

[40] Mazhar, A., Dell, S., Cuccia, D.J., Gioux, S., Durkin, A.J., Frangioni, J.V., Tromberg, B.J., ''Wavelength optimization for rapid chromophore mapping using spatial frequency domain imaging'', J. Biomed. Opt., 15, 061716, (2010)

[41] Akiyama, H., Hiyama, M., Hashimoto, C., ''Resection and reconstruction for carcinoma of the thoracic oesophagus'', Br. J. Surg., 63, pp. 206–209, (1976)

[42] Mittal, M., Siddiqui, M.R., Tran, K., Reddy, S.P., Malik, A.B., ''Reactive oxygen species in inflammation and tissue injury'', Antioxid. Redox Signal., 20, 1126–1167, (2014)

[43] Raziyeva, K., Kim, Y., Zharkinbekov, Z., Kassymbek, K., Jimi, S., Saparov, A., ''Immunology of Acute and Chronic Wound Healing'', Biomolecules, 11(700), (2021)

[44] Barberio, M., Felli, E., Pizzicannella, M., Agnus, V., Al-Taher, M., Seyller, E., Moulla, Y., Jansen-Winkeln, B., Gockel, I., Marescaux, J., et al., ''Quantitative serosal and mucosal optical imaging perfusion assessment in gastric conduits for esophageal surgery: An experimental study in enhanced reality'', Surg. Endosc., 35, pp. 5827–5835, (2020)

[45] Urade, T., Felli, E., Barberio, M., Al-Taher, M., Felli, E., Goffin, L., Agnus, V., Ettorre, G.M., Marescaux, J., Mutter, D., et al., ''Hyperspectral enhanced reality (HYPER) for anatomical liver resection'', Surg. Endosc., 35, pp. 1844–1850, (2021)

[46] Kawada, K., Hasegawa, S., Wada, T., Takahashi, R., Hisamori, S., Hida, K., Sakai, Y., ''Evaluation of intestinal perfusion by ICG fluorescence imaging in laparoscopic colorectal surgery with DST anastomosis'', Surg. Endosc., 31, pp. 1061–1069, (2017)

[47] Blanco-Colino, R., Espin-Basany, E., ''Intraoperative use of ICG fluorescence imaging to reduce the risk of anastomotic leakage in colorectal surgery: A systematic review and meta-analysis'', Tech. Coloproctol., 22, pp. 15–23, (2018)

[48] Hope-Ross, M., Yannuzzi, L.A., Gragoudas, E.S., Guyer, D.R., Slakter, J.S., Sorenson, J.A., Krupsky, S., Orlock, D.A., Puliafito, C.A., ''Adverse reactions due to indocyanine green'', Ophthalmology, 101, pp. 529–533, (1994)

# VIII. Quantified fluorescence imaging for tumor detection and margin assessment

Chapter V demonstrated the multimodal capabilities of the developed imaging platform, performing both optical properties imaging and fluorescence imaging for blood perfusion assessment. In Chapter VI and Chapter VII, the integration of the imaging device into the surgical workflow during preclinical trials was demonstrated. This chapter presents a unique application of the imaging platform, in which the combination of both modalities enables quantitative fluorescence imaging.

The emerging use of fluorescence imaging for tumor detection purposes is first discussed, followed by the inherent limitations of the use of conventional fluorescence imaging. Quantification of fluorescence is detailed along with its implementation using the developed imaging platform. First, *in-vitro* results demonstrated the importance of fluorescence quantification to enable accurate fluorescence assessment using fluorescent tissue-mimicking phantoms. Next, preclinical trials with colorectal and pancreatic cancer models and an assortment of fluorescent tracers demonstrated the limitations of conventional – i.e. non-quantitative – fluorescence imaging, and the need for a quantitative approach to fluorescence imaging.

## VIII.1. Context and motivation

Near-infrared (NIR) fluorescence imaging is gaining clinical acceptance for a growing number of surgical procedures due to its ability to enable perfusion analysis and detection of vital structures [1,2]. NIR light offers advantageous penetration depth in biological tissues up to a centimeter, making possible in-depth investigation of tissues. Another advantage of the NIR wavelength range is the low autofluorescence levels of tissues, maximizing the signal-to-background ratio in NIR fluorescence images. Several contrast agents have been deployed and clinically approved for NIR fluorescence imaging, of which ICG is one of the most frequently used. Recently, there has been an emergence of molecular targeted NIR fluorescence imaging applications, where a stable conjugation of a NIR fluorophore to a targeting molecule results in specific accumulation of the tracer in the tissue of interest such as tumor tissues [3].

However, the current approaches to fluorescence imaging are by definition qualitative and subjective, thus leading to variably different and inaccurate assessments of fluorescent agents accumulating in tissue. The two main reasons for it are related to instrumentation and tissue specific. When tissue is illuminated with excitation light, light travels from the source to the tissue. Part of the excitation photons are lost priori to reaching – and exciting – the fluorophore due to scattering and absorption. Once the fluorophore is excited,

it emits photons which are likewise partly lost due to scattering and absorption before exiting the tissue and traveling a distance to reach the detector. Thus, the intrinsic tissue optical properties play a significant role in the light entering and exiting the tissue. Thus, when imaging two tissues with exactly the same amount of fluorophore but different scattering and absorption properties, different raw fluorescence images will be displayed consequently to the different amounts of generated and detected fluorescence photons. In addition to the intrinsic tissue optical properties that impact the detected fluorescence, other external factors can be considered, including but not limited to illumination light source power, quality of optical components such as filters, and detection efficiency of the camera [4].

Consequently, all current *in-vivo* fluorescence imaging systems that are commercialized today perform qualitative, subjective assessments of tissue fluorescence, thus fluorophore accumulation in tissue. Markedly inaccurate estimates of the actual levels of fluorophores can ultimately lead to incomplete tumor resection, as in the case of tumor surgery [5-8]. For example, Valdes et al studied patients undergoing brain tumor surgery in which patients underwent fluorescence-guided surgery using the fluorescent agent protoporphyrin IX (Pp IX) and a state-of-the-art fluorescence imaging microscope performing herein called qualitative fluorescence imaging [9]. Images were first acquired, followed by *in-vivo* tissue measurements using a handheld quantitative spectroscopy probe that performed quantitative fluorescence measurements, followed by histological evaluation. A radical improvement by almost 20% of the detection of tumor tissue was reported using the quantitative approach, by detecting tumor tissues that would have been otherwise gone undetected (i.e., false negatives). Thus, a quantitative fluorescence imaging approach can improve the accuracy of fluorescence assessments *in-vivo*, leading to improved tumor tissue detection and ultimately, clinical outcomes.

## VIII.2. Materials and methods

### VIII.2.1. Quantitative fluorescence imaging

Normalization approaches have been established to compensate for part of these bias sources [10,11]. An commonly used empiric method, which is considered in this study is the normalization of the detected raw fluorescence $F_{x,m}$ by the reflectance at the excitation wavelength $R_x$. The normalized fluorescence maps denoted *F/R* are thus obtained by ratio of $F_{x,m}$ over $R_x$ **(VIII.E1)**.

$$F/R = \frac{F_{x,m}}{R_x} \qquad (VIII.E1)$$

While this method enables partial compensation for the loss of excitation light from the tissue, it is an incomplete method that does not fully account for the complex interplay of absorption and scattering at

both the excitation and emission wavelengths. Thus, a correction of the distorting effects of optical properties on the detected fluorescence is needed to enable quantitative estimates of the true amount of fluorophores. To this purpose, a previously validated algorithm that takes into account both scattering and absorption at the excitation and emission wavelengths is considered for this study [12]. From measurements of the diffuse reflectance of the tissue at the excitation $R_{d,x}$ and emission $R_{d,m}$ wavelengths and the absorption coefficient at the excitation wavelength $\mu_{a,x}$, the raw fluorescence $F_{x,m}$ can be corrected to extract a quantitative estimate of the tissue fluorescence $f_{x,m}$ **(VIII.E2)**.

$$f_{x,m} = F_{x,m} \cdot \frac{\mu_{a,x}}{\left(1 - R_{d,x}\right) . R_m} \qquad (VIII.E2)$$

This approach has been first validated for contact, spectroscopy point probe-based systems, but has recently been adapted in a widefield and real-time form, namely quantitative fluorescence Single Snapshot imaging of Optical Properties (qF-SSOP) [13].

SSOP is a method based on Spatial Frequency Domain Imaging, which consists in using spatially modulated light where the projection of sinusoidal light patterns at different frequencies and with several phase shifts is used to measure the diffuse reflectance of the sample, as well as optical properties over a large field of view [14]. SFDI is particularly is particularly suitable for use in the presented correction algorithm as it outputs each of the optical properties components required for the fluorescence correction **(E2)**. A 7 phase-implementation of SFDI has been selected for this study as the resulting images present little to no artifacts compared to SSOP. Further phase-shifting profilometry included in the SFDI workflow enables the correction of optical properties maps to compensate for the profile of the sample under study [15].

Using the previously validated multimodal imaging system for fluorescence imaging and optical properties imaging, quantitative fluorescence imaging could be performed by extracting optical properties at wavelengths close to the excitation and emission peaks to enable the correction of the raw fluorescence images. This clinically-compatible imaging platform is equipped with custom laser sources for tissue simultaneous characterization and fluorescence excitation. A mounted imaging head integrating 3 optical channels provides illumination through a digital micromirror-based projection system and detection by two NIR cameras that produce reflectance images for SFDI and fluorescence images, and one color camera that produce images for anatomical reference. Figure VIII.1 shows a picture of the imaging system and a schematic of the imaging workflow.

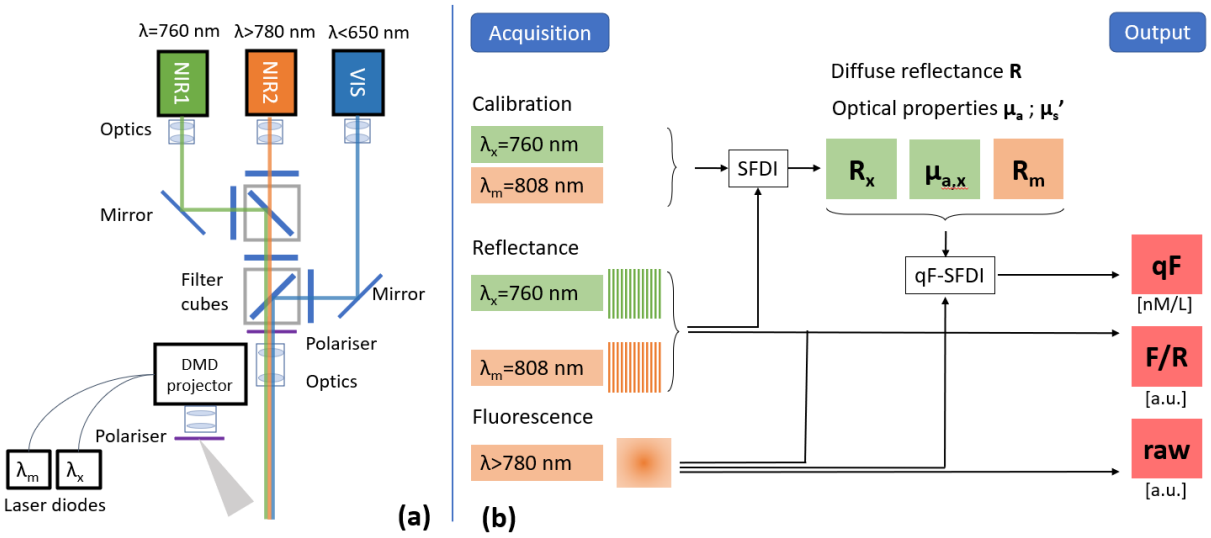


**Figure VIII.1 – Quantitative fluorescence imaging setup and workflow. (a) A custom setup for dual SFDI and fluorescence imaging was developed. One channel in the visible range (<650nm) provides an anatomical view of the surgical field. Two NIR channels (760nm and <780nm) are used to collect reflectance and fluorescence images. (b) The reflectance data collected at $\lambda_x$ = 760nm and $\lambda_m$ = 808nm is processed to derive diffuse reflectance and optical properties of the sample. This information is combined with the raw fluorescence signal yields the quantitative fluorescence (qF) images i.e. the tracer concentration maps. The reflectance data at $\lambda_x$ can also be used to normalize the raw fluorescence signal using a commonly employed empirical algorithm (F/R).**

### VIII.2.2. Tissue-mimicking fluorescent phantoms

An array of 12 tissue-mimicking fluorescent phantoms was manufactured. An uncured silicone matrix was supplemented with varying concentrations of scattering and absorbing materials – respectively $TiO_2$ and nigrosine. Fixed amounts of ZW800-1 fluorophore were added to each sample to reach a concentration of 100 nM/L.

One additional phantom was manufacturer and imaged with varying fluorophore concentration, ranging from 10 nM/L to 500 nM/L. The dilution series produced a calibration curve linking optical properties-corrected fluorescence levels to the fluorophore concentration. The inversion of this curve yielded a prediction curve to enable the extraction of concentration from corrected fluorescence maps.

The optical properties of these phantoms were measured using SFDI at 0 $mm^{-1}$ and 0.15 $mm^{-1}$ spatial frequencies with 7 phase shifts of 90°, at 760 nm and 808 nm. The fluorescence excitation was performed at 760nm using a CW illumination from the DMD projector, and 808 nm illumination switched off.

### VIII.2.3. Pancreatic and colorectal tumor models

*Cancer cell lines*

In this study, two different human tumor cell lines were employed to produce colorectal cancer tumors and pancreatic cancer tumors in small animal models. The HT29-luc2 cell line (HT29 cells transfected by luciferase-2) was selected for the colorectal model and the BxPC3-luc2 (Perkin Elmer, Waltham, MA, USA) was selected for the pancreatic model. Both cell lines were put in culture in RPMI 1640 (Gibco Invitrogen, Carlsbad, CA, USA) for 1 week until sufficient amounts of cells were obtained (> 3 million cells). Cells were free of mycoplasma species as verified by polymerase chain reaction (PCR) tests.

*Animal models*

Six-week-old athymic female nude mice (CD1-Fox1nu, Charles River Laboratories) were used to produce both orthotopic colon and pancreatic cancer models [16,17]. For the colon tumor models, subcutaneous tumors were first implanted after injection of a suspension of half a million HT29-luc2 cells in the lower back of one mouse. Approximately two weeks later, once reaching a size of about 5 mm diameter, these tumors were harvested, cut into small fragments (of approximately 3x3x1 mm in size), and then implanted in the wall of the cecum in 6 different mice after midline laparotomy. For the pancreatic models, an incision was performed in the left flank of 6 mice to expose the pancreas, followed by an injection of a suspension of cells – half a million in 50µL PBS solution – into the body of the pancreas. For the orthotopic tumor implantation procedures, the mice received painkilling medication by subcutaneous injection – 0.1 mg/kg buprenorphine every 8 hours as needed during and after surgery.

The tumor growth was regularly monitored through bioluminescence using a dedicated imaging system (IVIS Spectrum, Perkin Elmer, MA, USA) until reaching a sufficient size for the experiment – i.e., at least 5 mm diameter – approximately 4 weeks later.

### VIII.2.4. Fluorescent tumor tracers

Two different fluorescent tracers were used, one for each tumor cell lines. Both tracers consist in a combination of an 800 nm-dye and a tumor targeting agent. For the colorectal model, the EpCAM-f800 tracer was employed. This tracer is composed of an antibody fragment (EpCAM-f) that binds to the overexpressed EpCAM fragments found in epithelial cancers, conjugated to an 800 nm fluorophore (IRDye800CW) with peak excitation and emission wavelengths at 773 nm and 792 nm, respectively [18,19].

For the pancreatic tumor models, the cRGD-ZW800-1 tracer, currently undergoing clinical translation, was employed. This tracer consists of a cyclic pentapeptide (cRGD) that binds to the overexpressed integrins found in tumor cells, conjugated to a zwitterionic 800 nm fluorophore (ZW800-1) with peak excitation and emission wavelengths at 770 nm and 788 nm, respectively [20].

### VIII.2.5. Imaging protocol

Once the tumors were sufficiently large (above 5 mm in width), mice in each group were injected with their corresponding tracers, before sacrificing and imaging. Mice from the colorectal group were injected in the tail vein with 2 nM of the EpCAM-F800 tracer 48 hours prior to sacrifice. Mice in the pancreatic group, were injected in the tail vein with 10 nM of the cRGD-ZW800-1 tracer 8 hours prior to sacrifice. Immediately after sacrifice, the mice were imaged with the abdomen exposed, revealing primary tumors and possible metastasis. Reflectance images from SFDI sequences with spatial frequencies 0 $mm^{1}$ and 0.15 $mm^{-1}$ and 7 phase shifts of 90° were acquired at 760 nm and 808 nm, fluorescence images under CW excitation at 760 nm were collected, and color images for anatomical reference were collected.

Following these acquisitions, a set of organs was harvested and placed on a sheet of black paper before repeating the imaging sequence for assessment of the biodistribution of the tracers. Harvested organs include: heart, lungs, livers, stomach, pancreas, spleen, kidneys, small intestines, large intestines, muscle, skin and any metastasis found. The primary tumors were left in their implantation site for this step.

Finally, the primary tumors were resected. All tumors were fixed in formalin and embedded in paraffin for further histological analysis. After sectioning, 800 nm fluorescence microscopic fluorescence imaging was performed (Odyssey, LI-COR Biosciences, Lincoln, NE, USA). Hematoxylin-eosin (HE) staining was also performed and images acquired under white light illumination using a digital pathology slide scanner (IntelliSite Ultra Fast Scanner, Philips, Eindhoven, The Netherlands).

The macroscopic fluorescence images – raw fluorescence, F/R normalized fluorescence and quantitative fluorescence maps – were analyzed to determine the respective performances of theses imaging modalities in terms of signal to background ratio and tumor to background ratio. Next, based on the color images of the mice abdomen, ROIs were selected in areas judged to be at the tumor location, in a healthy area of the organ of implantation surrounding the tumor and in a healthy skin area located around the throat of neck respectively for colorectal and pancreatic models. Tumor ROIs were defined to follow the visible contours of the tumor in order to encompass most of it. ROIs in the tumor surrounding were defined to be as close as the tumor as possible, while only considering healthy tissue of the organ of implantation of the tumor. The size of the selected ROIs at the tumor locations and their surroundings were dependent on each case. The healthy skin area ROIs were consistently taken as a 4 mm x 4 mm square.

Signal to background ratio was defined as the peak value in the tumor ROI divided by the mean value in the skin ROI, as a general metric for tumor imaging contrast irrespective of organ specific tissue properties. Similarly, tumor-to-background ratio was defined as the peak value in the tumor ROI divided by the mean

value in its surrounding ROI, as a metric within organ of tumor contrast dependent on specific tissue properties.

### VIII.2.6. Biodistribution analysis

ROIs were selected based on the color images of the harvested organs inside each organ. Values were extracted and compared for each imaging output, producing estimates of the tracers biodistribution based on the different imaging modalities.

## VIII.3. Results

### VIII.3.1. *In-vitro* validation

The range of optical properties covered by the array of the tissue-mimicking phantoms was measured ranging from $\mu_a$ = 0.04 $mm^{-1}$ to 0.10 $mm^{-1}$ and $\mu_s'$ = 0.86 $mm^{-1}$ to 1.71 $mm^{-1}$ at 760 nm. **Table VIII.1** details the optical properties of each phantom at 760 nm. Although the fluorophore concentration has been kept fixed across the phantoms, a gradient in the raw fluorescence signal was detected, as shown in **Figure VIII.2**. First, a decrease in the raw fluorescence signal was observed with decreasing scattering or increasing absorption. Second, an increase in raw fluorescence signal was observed with increasing scattering and decreasing absorption. These findings demonstrate the significant distorting effects due to changes in optical properties on the detected fluorescence. The mean percentage error (MPE) relative to the known true fluorescence concentration was used as a metric of fluorescence signal variability. Using phantom #4, the raw fluorescence images without any correction for tissue optical properties demonstrated a significant variability with a MPE of 24.2 %. The quantitative fluorescence images demonstrated a correction for the distorting effects of optical properties of the detected fluorescence with a MPE of 15.6 %. The quantitative fluorescence results show fluorophore concentrations estimates closer to the true concentration, despite the changes in optical properties. First, these results demonstrate in a controlled phantom study the significant impact that the distorting effects of tissue optical properties have on the detected fluorescence, leading to highly inaccurate estimates of the fluorophores present. Second, these results demonstrate the ability of this approach to correct for the distorting effects of optical properties across the phantoms. Third, the quantitative images provide the user with absolute tracer concentration in nM/L units as opposed to raw or normalized fluorescence images which provide relative intensity in arbitrary units.

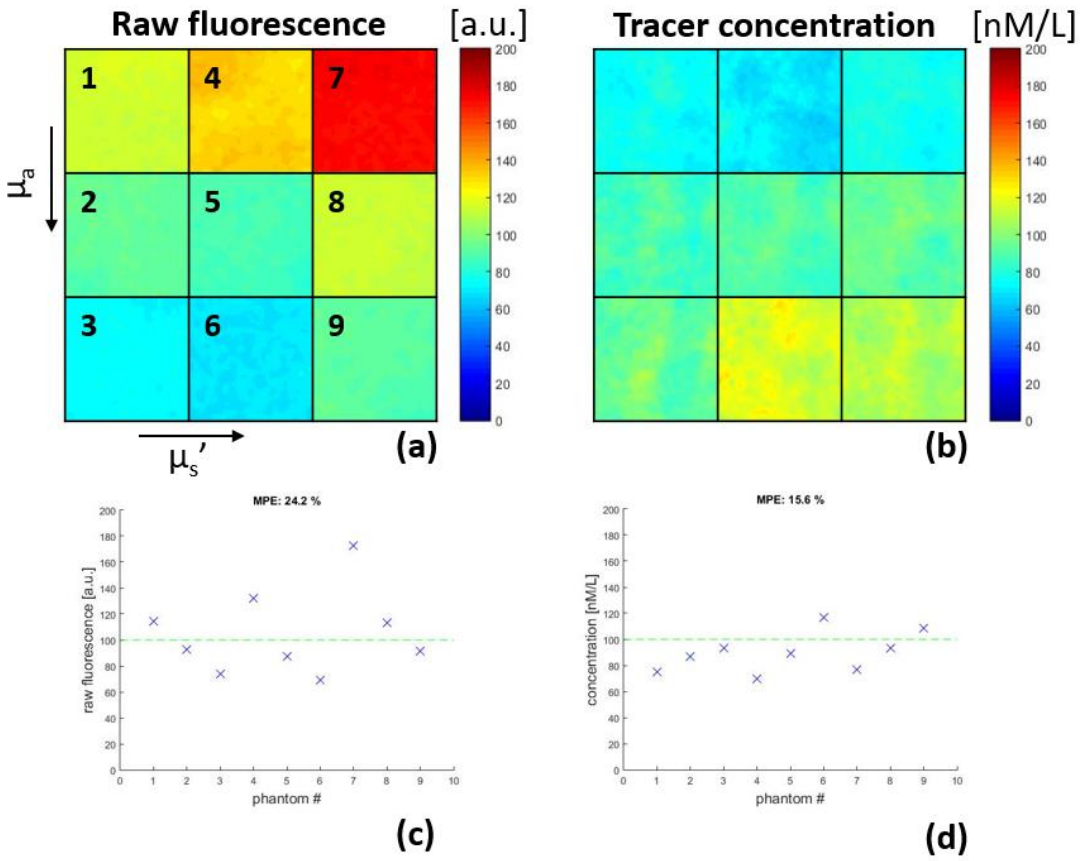


**Figure VIII.2 – *in-vitro* imaging of tissue mimicking phantoms with equal tracer concentration of 100nM/L but varying optical properties. (a) Distortion of the raw fluorescence signal is demonstrated with increasing absorption – top to bottom – and increasing scattering – left to right. (b) The estimated fluorescence is homogenous across the samples using quantitative imaging. The measured mean raw fluorescence (c) and tracer concentration (d) are compared to the reference true concentration, demonstrating a decrease of the MPE using quantitative imaging.**

| **Phantom #** | *1* | *2* | *3* | *4* | *5* | *6* | *7* | *8* | *9* |
|---|---|---|---|---|---|---|---|---|---|
| $\mu_a$ **(mm$^{-1}$) at 760nm** | *0.04* | *0.07* | *0.09* | *0.05* | *0.07* | *0.10* | *0.04* | *0.06* | *0.07* |
| $\mu_s'$ **(mm$^{-1}$) at 760nm** | *1.67* | *1.71* | *1.67* | *1.17* | *1.07* | *1.06* | *0.94* | *0.89* | *0.86* |

**Table VIII.1 – Optical properties of fluorescent tissue-mimicking phantoms.**

## VIII.3.2. Typical cases study: fluorescence maps comparison

Next, following the imaging protocol presented above, acquisitions were performed to produce raw fluorescence, F/R normalized fluorescence and quantitative fluorescence images of the mice abdomen. Here, illustrative cases are shown for both colorectal and pancreatic groups (Figure VIII.3). The three different imaging outputs were used to compare the estimated distribution of tracers by each method. By comparing the images, the impact of tissue optical properties on the fluorescence estimates could be determined. As expected from prior experience with these tracers, the raw fluorescence images showed high fluorescence intensities in tumors. Further, high fluorescence intensities were also observed in organs such as the kidneys, and liver for the colorectal models and kidneys and spleen for the pancreatic models. These results are expected as tracers are processed in these organs.

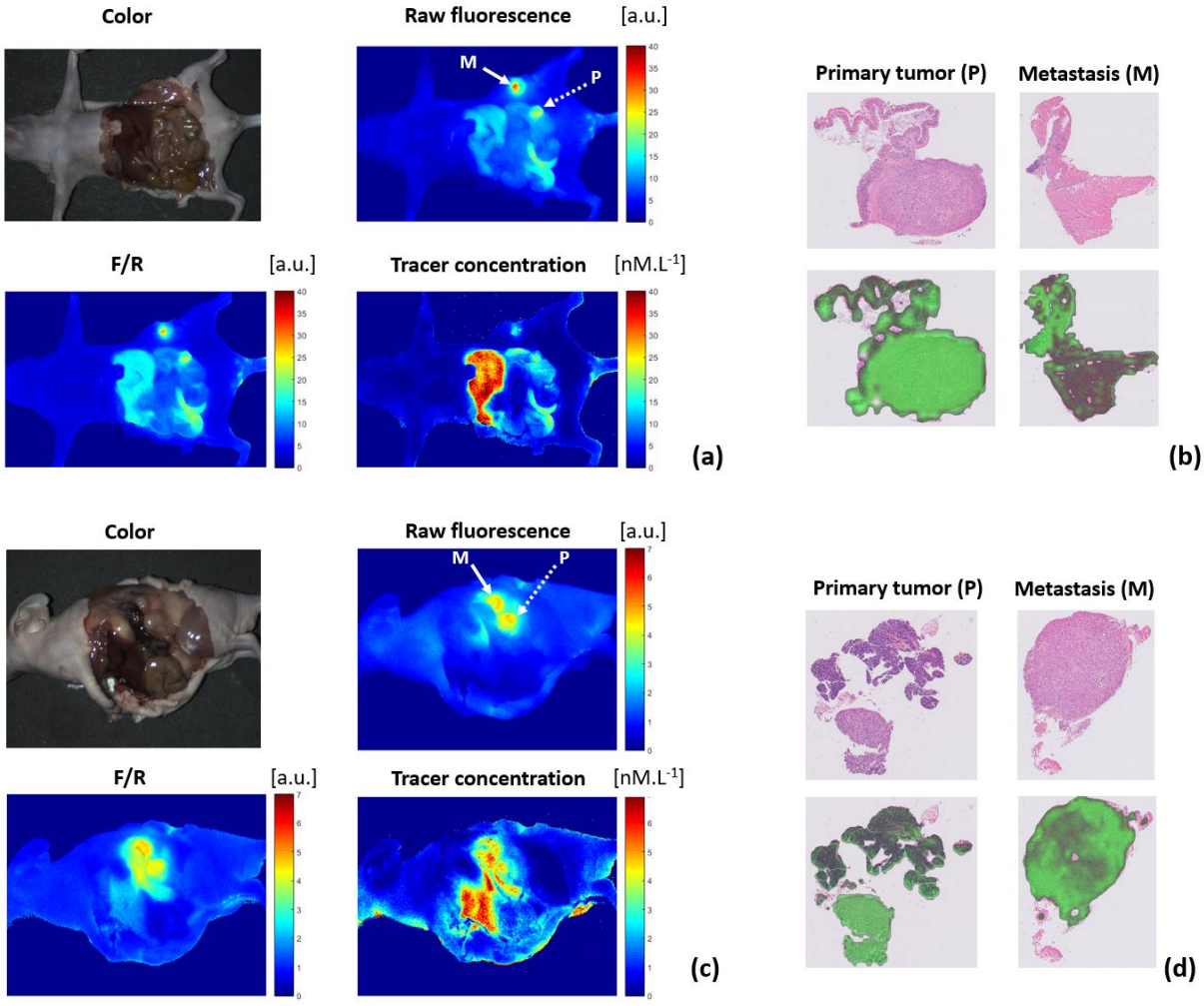


**Figure VIII.3 – *Ex-vivo* fluorescence images comparison. (a) Typical colorectal case study. Raw fluorescence (top right), normalized fluorescence (bottom left) and quantified fluorescence (bottom right) images are shown for comparison. The anatomical view merged with the raw fluorescence (top left) is shown for reference. The tracer concentration maps exhibits reduced background and a markedly different distribution of tracer compared to the raw fluorescence. (b) Histology images of one primary tumor and one metastasis. Their location in the body is marked on the raw fluorescence image respectively with a 'P' and a 'M' mark. (c) Typical**

**pancreatic case study. The tracer concentration map also show background reduction and higher tracer estimates in the high absorbing organs. (d) Histology images of one primary tumor and one metastasis.**

When examining the F/R normalized fluorescence, fluorescence levels were relatively higher in organs with high tissue absorption such as the spleen and liver. These results showed how the tracer levels can be underestimated by using the raw fluorescence images in these high absorbing areas.

Quantitative fluorescence images demonstrated more marked differences of tracer estimates across organs when compared to the raw fluorescence. First, organs with high tissue absorption (liver, spleen) showed higher tracer concentration than those found in tumors. These results were different than the estimates from the raw fluorescence, which showed higher fluorescence intensities in tumors than in high absorbing organs. Second, organs with high tissue scattering (e.g., skin or bowel) showed lower tracer concentrations. Third, quantitative images also demonstrated a lower background signal from healthy tissues, enabling a clearer delineation of tumors in most cases. Finally, the quantitative tracer concentration images were able to show more anatomical details than the raw fluorescence maps. The following sections provide a quantitative analysis of these findings, demonstrating the differences between raw, F/R and quantitative fluorescence images.

### VIII.3.3. Biodistribution analysis

The average biodistribution was assessed in both colorectal and pancreatic models based on the different imaging outputs as detailed in the charts in Figure VIII.4. The extracted mean values were scaled to match the quantified fluorescence levels in the primary tumors. A multiplicative factor was applied to the raw fluorescence and F/R normalized fluorescence datasets to set the arbitrary units scales to be comparable to the tracer concentration scale. This way, the apparent fluorescence intensity is equal for all imaging outputs, enabling the relative comparison of the qualitative modalities with the quantitative fluorescence. In accordance with the observations based on the abdomen images, the F/R normalization offered a compensation for the absorption of light by the tissues, showing increased signals in the liver, spleen and kidneys for instance.

For the colorectal group, quantitative fluorescence levels show an underestimation of 907 % ($p < 0.0003$) and 606 % ($p < 0.0005$) of the presence of fluorophore from raw fluorescence for the kidneys and the liver, respectively. For the pancreatic group, tracer estimates were underestimated of 234 % ($p < 0.0012$) and 159 % ($p < 0.0006$) by the raw fluorescence in the spleen and kidneys, respectively. These results demonstrate significant underestimation and consequent misinterpretation of the biodistribution in high absorbing organs when based on raw fluorescence estimates.

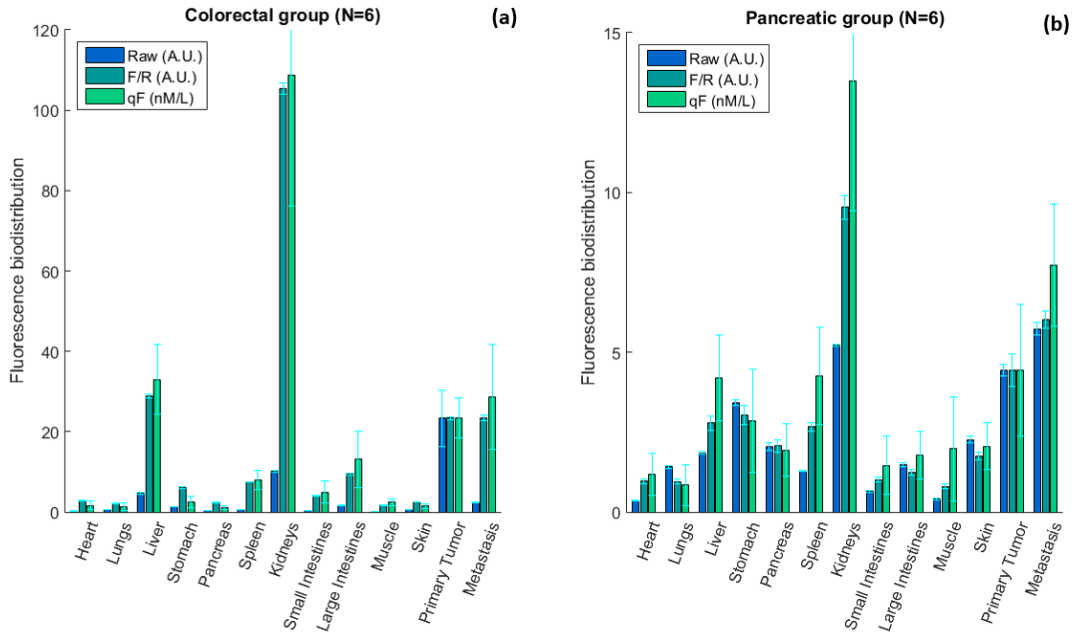


**Figure VIII.4 – Biodistribution estimation comparison. The average biodistribution extracted from the raw fluorescence images (Raw), the F/R normalized fluorescence images (F/R) and quantified fluorescence images (qF) are compared for both colorectal (N=6) and pancreatic (N=6) groups. Error bars show the corresponding standard deviations. A redistribution is suggested by the normalized and quantified fluorescence with regards to the outcome of raw fluorescence imaging.**

### VIII.3.4. Tumor detection performances: SBR and TBR analysis

Average SBR and TBR performances were assessed based on the abdomen images for primary tumors and metastasis separately, as the implantation sites were located in different tissue types. Comparison charts for both metrics are shown in Figure VIII.5. The F/R normalization showed modest improvements in the SBR compared to those of the raw fluorescence of 16% ($p < 0.006$) and 9% (N=2, not statistically significant) for the colorectal primary tumors and metastasis, respectively, and 20% ($p < 0.0005$) and 21% ($p < 0.0006$) for the pancreatic primary tumors and metastasis, respectively. However, quantitative fluorescence produced an increase in SBR of 492% ($p < 0.0011$) and 189 % (N=2, not statistically significant) for the colorectal primary tumors and metastasis, respectively, and of 60 % ($p < 0.012$) and 52 % ($p < 0.027$) for the pancreatic tumors, respectively.

The TBR demonstrated similar trends as the SBR estimates, but to a lesser extent. F/R normalization produced TBR gains of 10 % ($p > 0.10$), 5 % ($p > 0.8$) for the colorectal primary tumors and metastasis, respectively, and 10 % ($p > 0.14$) and 13 % ($p < 0.43$) respectively for the pancreatic tumors, respectively. Correspondingly, the quantification led to TBR improvements of 15 % ($p > 0.18$), 88 % ($p > 0.16$), for the colorectal primary tumors and metastasis, respectively, and 33 % ($p < 0.048$) and 57 % ($p < 0.012$) for the pancreatic tumors, respectively.

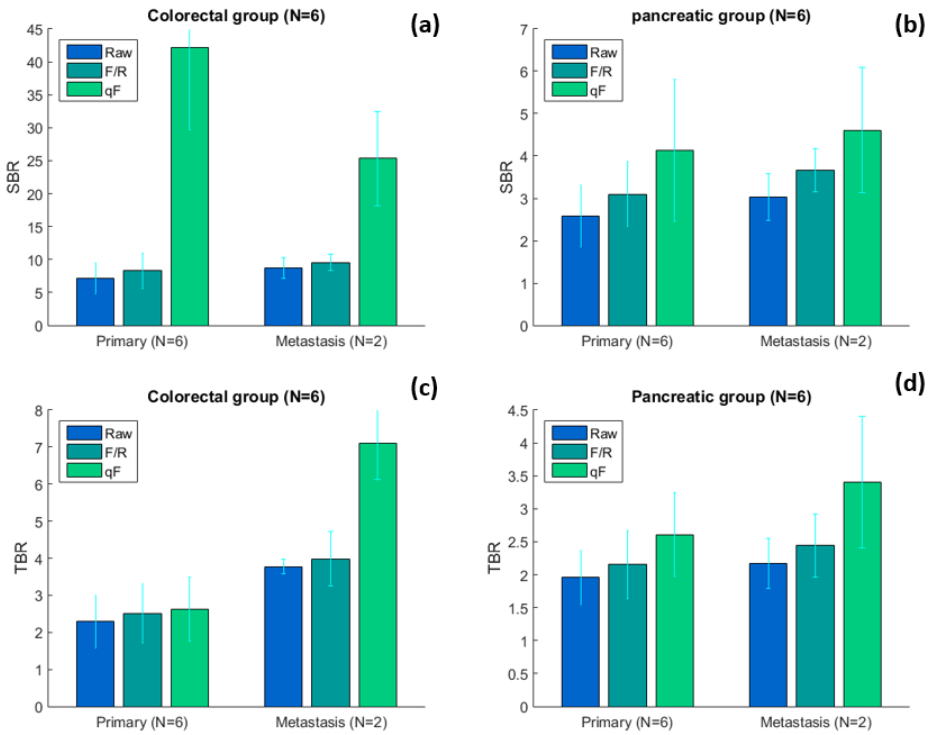


**Figure VIII.5 – SBR and TBR analysis. Average SBR and TBR values are compared separately for primary tumors and metastasis for both groups, based on the *ex-vivo* abdomen images. Error bars show the corresponding standard deviations. A significant SBR improvement is produced by the F/R normalization and the correction of optical properties as part of the quantification.**

These results demonstrated significant increase in SBR using F/R normalized fluorescence and quantitative fluorescence imaging, in accordance with the background reduction previously observed. Lower SBR were observed in the pancreatic group, corresponding to higher background fluorescence inherent to the tracer employed. Raw fluorescence levels from healthy skin areas were measured to be on average 3.6 times higher in the pancreatic group compared to the colorectal group.

## VIII.4. Discussion

These results demonstrate in phantom an animal studies the impact of tissue optical properties on the detected fluorescence by using a multimodal imaging platform that enables co-registered imaging of endogenous optical properties and exogenous fluorescence imaging. Phantom studies demonstrate that significant distortions on the detected fluorescence observed with raw fluorescence measurements, the partial correction with the F/R approach, and the significant correction for these effects using quantitative fluorescence.

Next, *ex-vivo* animal studies clearly demonstrated a markedly different biodistribution when estimating tracer levels using the conventional, raw fluorescence approach compared to a quantitative approach. In the quantified fluorescence maps, not only high absorption was compensated for, highlighting higher concentrations in organs that showed low raw fluorescence, i.e., that were estimated to have low tracers levels according to raw fluorescence images. Further, residual background in healthy tissues was also reduced, which explained how in later studies quantitative fluorescence showed significantly improved SBRs and TBRs. Additionally, the quantified fluorescence maps appeared to contain a greater amount of details, showing clearer delineations between tissues and structures of interest.

These observations were confirmed by the biodistribution analysis where the retrieved signals from highly absorbing or lowly scattering organs were higher in the F/R and quantified fluorescence maps. However, the measured concentrations would need to be validated by comparison to a standard concentration estimation method, such as tissue solubilization.

The increased SBR and TBR values represent an additional asset for tumor detection and delineation. F/R images produced a more modest improvement due to the relatively low differences in absorption between the tumors and healthy tissues. Overall, the lower SBR and TBR values observed in the pancreatic group could stem from the employed tracer. Indeed, its relatively low molar weight favors its diffusion across the body. However, an additional validation step would be required to confirm the detected concentrations at the tumor sites. A cell-counting method such as flow cytometry could provide a ground-truth measurement.

SFDI does not enable real-time imaging because of the large number of images to be acquired. Using a state-of-the-art deep learning-based SSOP alternative implementation would make the optical properties imaging workflow real-time compatible while preserving accuracy and image quality [21]. An additional obstacle to the real-time implementation of this technique is the common use of the 800 nm imaging channel of the system for both optical properties imaging and fluorescence imaging. A possible solution would integrate an additional imaging channel, at the cost of losing detection efficiency and adding complexity to the imaging system.

## VIII.5. Conclusion

This study demonstrated to combination of endogenous optical properties imaging using SFDI with exogenous fluorescence imaging using targeted agents for quantified fluorescence imaging of colorectal and pancreatic tumors. Using the previously described imaging platform, high-quality, widefield, quantitative fluorescence imaging was achieved. The ability to extract tracer concentration maps represents a great improvement in the reproducibility and objectivity of fluorescence imaging for tumor resection procedures. In particular, even though optical properties may vary drastically across organs, the

correction of induced fluorescence intensity distortions provided by the quantification process alleviates misinterpretations in the biodistribution analysis. Additionally, reduced background and sharper imaging greatly improves contrast between tumors and healthy tissues.

**References**


[1] Vahrmeijer A., Hutteman M., van der Vorst J., van de Velde C.J.H., Frangioni J.V., ''Image-guided cancer surgery using near-infrared fluorescence'', Nature Reviews Clinical Oncology, 10, pp. 507–518, (2013)

[2] van Manen L., Handgraaf H.J.M, Diana M., Dijkstra J., Ishiwaza T., Varhmeijer A.L., Mieog J.S.D., ''A practical guide for the use of indocyanine green and methylene blue in fluorescence-guided abdominal surgery'', Journal of Surgical Oncology, 118(2), pp. 283-300, (2018)

[3] Hernot S., van Manen L., Debie P., Mieog J.S.D., Vahrmeijer A.L., ''Latest developments in molecular tracers for fluorescence image-guided cancer surgery'', Lancet Oncology, 20(7), pp. 354-367, (2019)
[4] Koch M., Symvoulidis P., Ntziachristos V., '' Tackling standardization in fluorescence molecular imaging'', Nature Photonics, 12(9), pp. 505-515, (2018)
[5] Valdes P.A., Jacobs V., Harris B.T., Wilson B.C., Leblond F., Paulsen K.D., Roberts D.W., ''Quantitative fluorescence using 5-aminolevulinic acid-induced protoporphyrin IX biomarker as a surgical adjunct in low-grade glioma surgery'', Journal of Neurosurgery, 123(3), pp. 771-780, (2015)

[6] Valdes P.A., Millesi M., Widhalm G., Roberts D.W., ''5-aminolevulinic acid induced protoporphyrin IX (ALA-PpIX) fluorescence guidance in meningioma surgery'', Journal of Neurooncology, 141(3), pp. 555-565, (2019)

[7] Valdes P.A., Leblond F., Jacobs V.L., Wilson B.C., Paulsen K.D., Roberts D.W., ''Quantitative, spectrally-resolved intraoperative fluorescence imaging'', Scientific Reports, 2(798), pp. 1-7, (2012)

[8] Mieog J.S.D., Achterberg F.B., Zlitni A., Hutteman M., Burggraaf J., Swijnenburg R.J., Gioux S., Vahrmeijer A.L., ''Fundamentals and developments in fluorescence-guided cancer surgery'', Nature Reviews Clinical Oncology, 19(1), (2022)

[9] Valdes P.A., Leblond F., Kim A., Harris B.T., Wilson B.C., Fan X., Tosteson T.D., Hartov A., Ji S., Paulsen K.D., Roberts D.W., ''Quantitative fluorescence in intracranial tumor: implications for ALA-induced PpIX as a surgical biomarker to guide resection procedures'', Journal of Neurosurgery, 115(1), pp11-17, (2011)

[10] Ntziachristos V., Turner G., Dunham J., Windsor S., Soubret A., Ripoll J., Shih H.A., "Planar fluorescence imaging using normalized data", Journal of Biomedical Optics, 10(6), 064007, (2005)

[11] Themelis G., Yoo J.S., Soh K.S., Schulz R., Ntziachristos V., "Real-time intraoperative fluorescence imaging system using light-absorption correction", Journal of Biomedical Optics, 14(6), 064012, (2009)

[12] Kim A., Khurana M., Moriyama Y., Wilson B.C., ''Quantification of in vivo fluorescence decoupled from the effects of tissue optical properties using fiber-optic spectroscopy measurements", Journal of Biomedical Optics, 15(6), 067006, (2010)

[13] Valdes P.A., Angelo J.P., Choi H.S., Gioux S., ''qF-SSOP: real-time optical property corrected fluorescence imaging'', Biomedical Optics Express, 8(8), pp. 3597-3605, (2017)

[14] Cuccia D.J., Bevilacqua F., Durkin A.J., Ayers F.R., Tromberg B.J., "Quantitation and mapping of tissue optical properties using modulated imaging", Journal of Biomedical Optics, 14(2), 024012, (2009)

[15] Gioux S., Mazhar A., Cuccia D.J., Durkin A.J., Tromberg B.J., Frangioni J.V., ''Three-dimensional surface profile intensity correction for spatially modulated imaging'', Journal of Biomedical Optics, 14(3), 034045, (2009)

[16] Tseng W., Leong X., Engleman E., ''Orthotopic mouse model of colorectal cancer'', Journal of Visualized Experiments, 10(484), (2017)

[17] Moreno J. A., Sanchez A., Hoffman R. M., Nur S., Lambros M. P., ''Fluorescent Orthotopic Mouse Model of Pancreatic Cancer'', Journal of visualized experiments, (115), 54337, (2016)

[18] Boogerd L.S.F., Boonstra M.C., Prevoo H.A.J.M., Handgraaf H.J.M., Kuppen P.J.K., van de Velde C.J.H., Fish A., Cordfunke R.A., Valentijn A.R.P.M., Terwisscha van Scheltinga A.G., MacDonald G.C., Cizeau J., Premsukh A., Vinkenburg van Slooten M.L., Burggraaf J., Sier C.F.M., Vahrmeijer A.L., ''Fluorescence-guided

tumor detection with a novel anti-EpCAM targeted antibody fragment: Preclinical validation'', Surgical Oncology, 28, pp. 1-8, (2019)

[19] Handgraaf H.J.M., Boonstra M.C., Prevoo H.A.J.M., Kuil J., Bordo M.W., Boogerd L.S.F., Sibinga Mulder B.G., Sier C.F.M., Vinkenburg-van Slooten M.L., Valentijn A.R.P.M., Burggraaf J., van de Velde C.J.H., Frangioni J.V., Vahrmeijer A.L., ''Real-time near-infrared fluorescence imaging using cRGD-ZW800-1 for intraoperative visualization of multiple cancer types'', Oncotarget, 8(13), pp. 21054-21066, (2017)

[20] de Valk K.S., Deken M.M., Handgraaf H.J.M., Bhairosingh S.S., Bijlstra O.D., van Esdonk M.J., Terwisscha van Scheltinga A.G.T., Valentijn A.R.P.M., March T.L., Vuijk J., Peeters K.C.M.J., Holman F.A., Hilling D.E., Mieog J.S.D., Frangioni J.V., Burggraaf J., Vahrmeijer A.L., ''First-in-Human Assessment of cRGD-ZW800-1, a Zwitterionic, Integrin-Targeted, Near-Infrared Fluorescent Peptide in Colon Carcinoma'', Clinical Cancer Research, 26(15), pp. 3990-3998, (2020)

[21] Aguénounon E., Smith J.T., Al-Taher M., Diana M., Intes X., Sylvain Gioux S., "Real-time, wide-field and high-quality single snapshot imaging of optical properties with profile correction using deep learning", Biomedical Optics Express, 11(10), pp. 5701-5716, (2020)

# Conclusion

The lack of objective, reliable tools to assess tissues status in real-time, or their nonexistence in a clinically compatible implementation were the primary motivations for this thesis project. Consequently, the main contribution of this work has been the development of a clinically compatible multimodal imaging platform capable of real-time widefield oxygenation and fluorescence imaging as part as the surgical workflow.

The imaging platform described in Chapter V consists in a medical cart-based device supporting a mounted imaging head. This custom imaging head features illumination and detection paths allowing for both fluorescence and optical properties imaging. Assorted custom laser sources – 2 units with 6 interchangeable modules each – are used for tissue optical characterization and fluorophore excitation and bright filtered white light sources ensure illumination the surgical workflow. Finally, a high-performance computer equipped with a purposely developed software has been integrated to the platform for device control, data processing, and visualization. The state-of-the-art SSOP implementation showed optical properties extraction of tissue-mimicking phantoms within less than 2.7 % error compared to standard SFDI, showing good accuracy and ensuring the reliability of the measured $StO_2$ rates. *In-vitro* tests on fluorescent dilutions showed high sensitivity, necessary for real-time ICG fluorescence imaging. Finally, *in-vivo* validation during preclinical tests on small bowel total occlusion and reperfusion were performed. Real-time ischemia monitoring was demonstrated based on the extracted $StO_2$ rates, in agreement with ICG fluorescence imaging.

In order to further validate the reliability of $StO_2$ for ischemia quantification, additional preclinical trials were designed to confront the oxygenation imaging outcome with robust biomarkers such as local capillary lactates. As presented in Chapter VI, a first study in the small bowel with total occlusion and reperfusion showed strong negative correlation between the lactates levels and $StO_2$ rates, confirming the ability of the platform to not only detect but also quantify the level of ischemia. Histological analysis further confirmed the ischemia. Secondly, the ability of the platform to quantify ischemia in the stomach was validated in Chapter VII, using again confrontation to lactates levels and histological analysis. These sets of experiments constitute a demonstration of the suitability of oxygenation imaging for blood perfusion assessment. In particular, its use during colorectal surgery and esophagectomy procedures might lead to reducing the risk for anastomotic leakage, by identifying insufficiently perfused area within the anastomotic site.

Ultimately, the capability of the platform to perform high-quality widefield quantified fluorescence imaging was investigated in Chapter VIII. *In-vitro* validation was first performed on fluorescent tissue-mimicking phantoms with varying optical properties but fixed fluorophore concentration. The quantification algorithm showed a correction of the distortions induced in the raw fluorescence signals by the varying optical properties. A following study in mice aimed at evaluating the impact of quantitative fluorescence in tumor

surgery. Quantification of fluorescence showed an underestimation tracer concentration in high absorbing tissues. Moreover, quantified fluorescence images benefited from decreased background levels, and a clearer delineation of the tumors. Overall, such technology is expected to provide more objective assessment of fluorescence imaging, for improved surgical field navigation, tumor margin assessment but also increased outcome reproducibility.

## Perspectives

Perspectives for future work can be decomposed in several axes: reinforcing the validation of the employed methods or extending their application to different frameworks; improving the integration to the surgical workflow and the usability in the operating room; enhancing the technology capabilities or adding new functionalities. The next paragraphs offer suggestions for future work per work axis, as defined in Chapter IV:

*Work axis 1: Imaging platform development*

The images presented in this work were all obtained by post-processing the data. The integration of real-time processing and visualization would be an additional step towards a more complete imaging system, making full use of the high-performance workstation integrated to the platform. Moreover, in order to provide a more user-friendly experience, the platform should be equipped with a straightforward yet comprehensive user interface, allowing direct visualization of the imaging outcome, tuning of the overlay with the anatomical view, and recording of the data. As the visualization on remote display might disrupt the surgical workflow, the integration of an augmented reality device to the imaging could greatly enhance the user's experience. The addition of foot switch controls and touchscreens to interact with the interface would be suitable in a clinical environment.

To further enhance the usability of the imaging system in the operating room, the imaging head could be upgraded with motorized lenses and aperture controls for remote control of the focusing. The mobility of the platform could also be improved for easier handling in the operating room by miniaturizing the system, including the imaging head, laser sources and the cart base itself. A smaller footprint and improved ergonomics would further minimize the interferences with the surgical workflow.

The adaptation of the imaging device into an endoscopic form would greatly impact minimally invasive surgical procedures, as the possible interactions surgeons can have with the tissues are even more limited compared to open surgery. Such a device could share the same instrumentation base as described, including the laser and white light illumination solutions, as well as the integrated workstation for data acquisition, processing and storage.

If the platform integrates the latest SSOP developments for real-time high quality oxygenation imaging, the presented results were limited to optical properties characterization at only two wavelengths. Incrementing the number of wavelengths by implementing time modulation would enable the extraction of additional chromophores such as water and lipids, but also structural parameters including scattering power and amplitude. Increasing the number of wavelengths per channel while producing real-time imaging can be achieved by means of temporal modulation of the illumination. Such extra information could thus be used to further characterize the status of tissues. Moreover, similarly to hyperspectral approaches, this greater amount of information represents possible input to a tissue recognition algorithm, paving the way for the use of such technology for diagnosis purposes.

The integration of advanced SFDI-based technologies such as multifrequency illumination would add the ability to investigate different tissue layers. The use of neural networks for processing such data might be a suitable solution.

Structural imaging capabilities could also be extended by implementing laser speckle imaging, revealing blood flow in addition to oxygenation parameters for blood perfusion assessment. Finally, by adding a camera sensitive to the short-wave infrared wavelengths in the 900nm – 1700nm range (also referred to as the NIR-II range) increased penetration depth for fluorescence imaging could be achieved.

*Work axis 2: Blood perfusion assessment*

This work focused mainly on ischemia quantification using the $StO_2$ rate as metric. Validation was given by comparison against standard biomarkers assessment such as local capillary lactates or histological analysis. A further validation step would include the comparison with other optical NIR spectroscopy-based instrument such as $StO_2$ point probes and hyperspectral devices. Additionally, while the conducted studies were limited to total occlusion settings, partial occlusions – venous or arterial – were not considered. Additional studies could demonstrate the full potential of the platform by exploiting all of the extracted oxygenation parameters: $StO_2$, [HHb], [$HbO_2$], total hemoglobin; for further hemodynamics analysis. Additionally, ischemia quantification was performed in priority in the small bowel for practical reasons. Indeed, the good accessibility of this organ and of its vasculature make it an ideal test subject for ischemia monitoring. However, real-time blood perfusion assessment could be demonstrated for a variety of other surgical procedures such as reconstructive surgery and transplantation surgery (e.g. liver and kidney), requiring additional imaging protocols.

By increasing the number of wavelength acquisitions, additional chromophores relevant to blood perfusion assessment could be extracted. In particular, methemoglobin is a form of hemoglobin which cannot bind to oxygen, therefore not participating to the oxygenation process. For healthy subjects, the fraction of methemoglobin is low and is in practice neglected, but its quantification could lead to the investigation of

oxygenation disorders such as methemoglobinemia, where the fraction of methemoglobin is considerably higher than normal, reducing the oxygen transport to the tissues. Additionally, melanin would be a chromophore of interest when investigating blood perfusion in the skin. Indeed, depending on the skin type, varying amount of melanin can be found and introduce bias in the hemoglobin concentrations extraction. This would be particularly relevant in a point-of-care approach, for instance for the diagnosis of peripheral vascular diseases such as critical limb ischemia.

Ultimately, provided the capability of the imaging platform to identify tissue types, the a priori knowledge of the investigated organ type could be paired with the extracted oxygenation parameters to provide automatic detection of optimal resection lines, or tissue viability scores previously established.

*Work axis 3: Quantified fluorescence imaging*

In order to fully characterize the performances of quantitative fluorescence imaging, a validation by comparison with gold standard methods such a cell cytometry or tissue solubilization-based titration is required. This way, a correlation between the measured amount of fluorescent tracer and the amount of detected tumor cells could be established. The outcome of quantitative fluorescence imaging might differ from the standard methods based on several factors. First, the calibration process does not take into account the chemical environment of the fluorophore, which in turn affects it absorption and emission spectra. Second, the scope of the employed correction algorithm might not encompass tissues with higher absorption and lower scattering coefficients, as well as situations where the fluorophore concentration increases such that the absorption from the fluorophore is comparable to that of the tissue itself. Following these considerations, alternative correction algorithms might be employed.

Further application to *ex-vivo* human tissues immediately after tumor resection would also enable better assessment of the performances by benefiting from observable features at larger scales, as well as bringing the technology one step closer to clinical translation. Repeating the experiments for various tracers and cancer models will be required to identify clinical applications where the impact of this technique is the strongest.

While the current implementation involves standard SFDI measurements, by employing the state-of-the-art SSOP technique and adapting the acquisition workflow, real-time high-quality imaging could be achieved. Moreover, the tissue optical properties characterization is currently limited to an input to the fluorescence quantification algorithm, but could be used to extract functional parameters as well. These extra outputs could be useful throughout the tumor resection procedure, as a correlation between the distribution of endogenous chromophores and tissue structural parameters, and the distribution of fluorescent tracer could be established. Such correlation could yield more accurate tumor margin

assessment. Ultimately, the potential subsequent reconstruction procedure could benefit from the extraction of functional parameters for tissue viability assessment.

# A1. Appendix 1

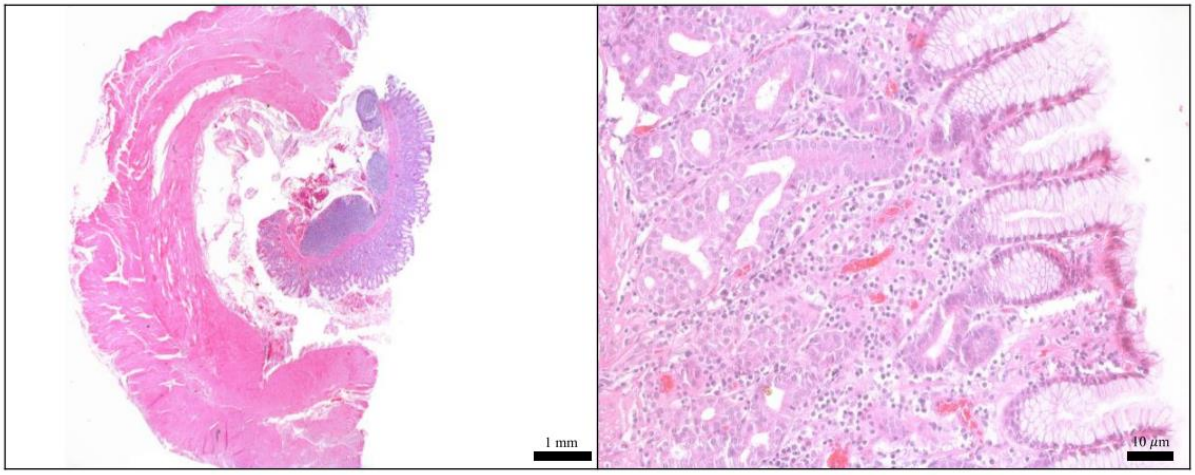


**Figure A1.1 – Control biopsy of the stomach (T0). Hematoxylin and Eosin staining of ROI-R (Pig 1) before the tubulization (T0). Both full thickness (left) and mucosae (right) magnification show no alteration of the tissue before surgery.**

**A**

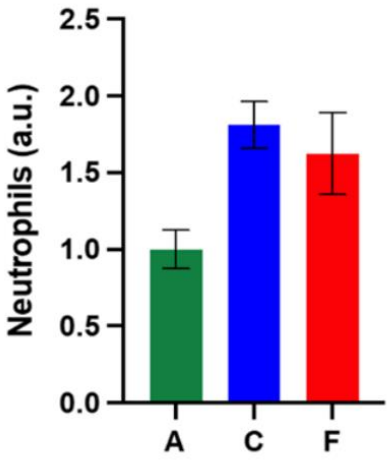


**B**

| | A | C | F |
|---|---|---|---|
| **Number of values** | **6** | **6** | **6** |
| **Minimum** | 0.3750 | 1.500 | 0.7500 |
| **25% Percentile** | 0.9375 | 1.500 | 1.031 |
| **Median** | 1.125 | 1.688 | 1.688 |
| **75% Percentile** | 1.125 | 2.250 | 2.063 |
| **Maximum** | 1.125 | 2.250 | 2.625 |
| **Mean** | 1.000 | 1.813 | 1.625 |
| **Std. Deviation** | 0.3062 | 0.3687 | 0.6567 |
| **Std. Error of Mean** | 0.1250 | 0.1505 | 0.2681 |
| **Lower 95% CI** | 0.6787 | 1.426 | 0.9358 |
| **Upper 95% CI** | 1.321 | 2.199 | 2.314 |

*A = antrum (ROI-A)*
*C = corpus (ROI-C)*
*F = fundus (ROI-F)*

**Figure A1.2 – Neutrophils distribution (A) and quantification (B). The overall neutrophils number in corpus and fundus was 81.3% and 62.5% higher than antrum, respectively. Data are expressed as mean and ± SEM and normalized for ROI-A.**

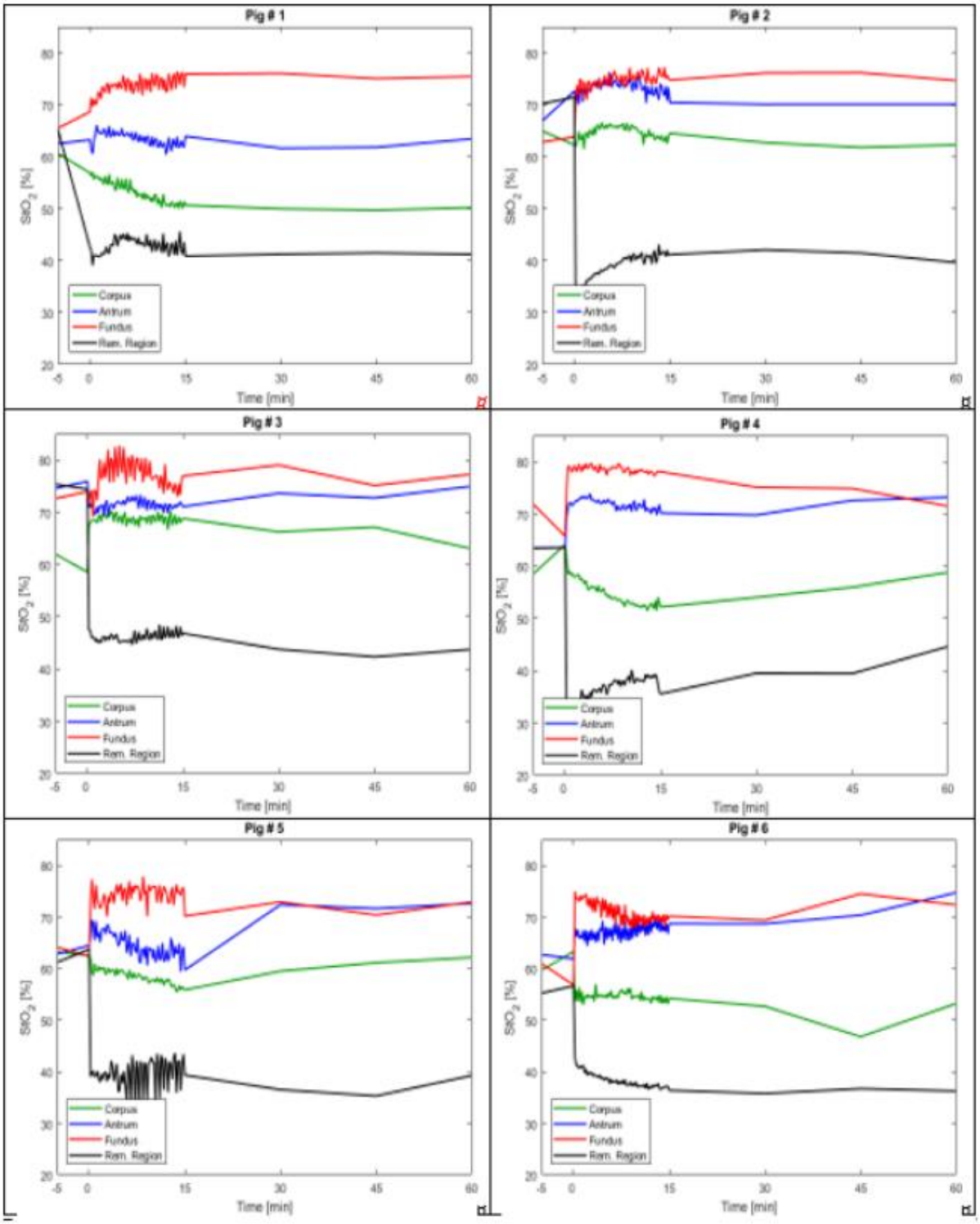


**Figure A1.3 – StO2% temporal trends for all subjects. StO2% measurements at ROI-R (black) are lower than ROI-A (green), ROI-C (corpus) and ROI-F (fundus) at T15, T30, T45, and T60. Instead, after GC completion, StO2% values increase from corpus to fundus.**

| pH | T0 | T15 | T30 | T45 | T60 |
|---|---|---|---|---|---|
| Mean | 1,000 | 1,001 | 1,001 | 1,002 | 1,001 |
| Std. Error of Mean | 0,002 | 0,002 | 0,002 | 0,002 | 0,002 |
| **Dunnett's multiple comparisons test** | **Mean Diff,** | **95,00% CI of diff,** | **Adjusted P Value** | | |
| 0 vs. 15 | -0,00136 | -0,004086 to 0,001368 | 0,350 | | |
| 0 vs. 30 | -0,00136 | -0,004346 to 0,001628 | 0,414 | | |
| 0 vs. 45 | -0,00159 | -0,004423 to 0,001253 | 0,277 | | |
| 0 vs. 60 | -0,00091 | -0,005884 to 0,004073 | 0,914 | | |
| **pCO2** | **T0** | **T15** | **T30** | **T45** | **T60** |
| Mean | 1,000 | 0,944 | 0,936 | 0,980 | 0,995 |
| Std. Error of Mean | 0,025 | 0,043 | 0,046 | 0,003 | 0,031 |
| **Dunnett's multiple comparisons test** | **Mean Diff,** | **95,00% CI of diff,** | **Adjusted P Value** | | |
| 0 vs. 15 | 0,0561 | -0,06330 to 0,1754 | 0,391 | | |
| 0 vs. 30 | 0,0639 | -0,09896 to 0,2268 | 0,520 | | |
| 0 vs. 45 | 0,0199 | -0,06439 to 0,1041 | 0,827 | | |
| 0 vs. 60 | 0,0047 | -0,05201 to 0,06136 | 0,994 | | |
| **pO2** | **T0** | **T15** | **T30** | **T45** | **T60** |
| Mean | 1,000 | 1,043 | 1,143 | 1,131 | 1,098 |
| Std. Error of Mean | 0,054 | 0,051 | 0,043 | 0,075 | 0,058 |
| **Dunnett's multiple comparisons test** | **Mean Diff,** | **95,00% CI of diff,** | **Adjusted P Value** | | |
| 0 vs. 15 | -0,0432 | -0,1315 to 0,04523 | 0,364 | | |
| 0 vs. 30 | -0,1429 | -0,2630 to -0,02282 | **0,026** | | |
| 0 vs. 45 | -0,1308 | -0,2387 to -0,02276 | **0,024** | | |
| 0 vs. 60 | -0,0978 | -0,1443 to -0,05134 | **0,002** | | |
| **HCO3-** | **T0** | **T15** | **T30** | **T45** | **T60** |
| Mean | 1,000 | 0,982 | 0,991 | 1,003 | 1,000 |
| Std. Error of Mean | 0,025 | 0,041 | 0,044 | 0,011 | 0,010 |
| **Dunnett's multiple comparisons test** | **Mean Diff,** | **95,00% CI of diff,** | **Adjusted P Value** | | |
| 0 vs. 15 | 0,0180 | -0,1257 to 0,1617 | 0,9738 | | |
| 0 vs. 30 | 0,0095 | -0,1545 to 0,1736 | 0,9983 | | |
| 0 vs. 45 | -0,0032 | -0,1156 to 0,1092 | 0,9999 | | |
| 0 vs. 60 | 0,0005 | -0,08727 to 0,08833 | >0,9999 | | |
| **Systemic lactates** | **T0** | **T15** | **T30** | **T45** | **T60** |
| Mean | 1,000 | 1,111 | 1,136 | 1,182 | 1,204 |
| Std. Error of Mean | 0,113 | 0,075 | 0,086 | 0,119 | 0,104 |
| **Dunnett's multiple comparisons test** | **Mean Diff,** | **95,00% CI of diff,** | **Adjusted P Value** | | |
| 0 vs. 15 | -0,111 | -0,2503 to 0,02826 | 0,107 | | |
| 0 vs. 30 | -0,136 | -0,3925 to 0,1207 | 0,310 | | |
| 0 vs. 45 | -0,182 | -0,3285 to -0,03453 | **0,022** | | |
| 0 vs. 60 | -0,204 | -0,3800 to -0,02872 | **0,028** | | |
| **BE(a)** | **T0** | **T15** | **T30** | **T45** | **T60** |
| Mean | 1,000 | 0,923 | 1,036 | 1,036 | 1,011 |

| | | | | | |
|---|---|---|---|---|---|
| Std. Error of Mean | 0,147 | 0,221 | 0,186 | 0,086 | 0,073 |
| **Dunnett's multiple comparisons test** | **Mean Diff,** | **95,00% CI of diff,** | **Adjusted P Value** | | |
| 0 vs. 15 | 0,07735 | -0,7151 to 0,8698 | 0,9891 | | |
| 0 vs. 30 | -0,03591 | -0,7287 to 0,6568 | 0,999 | | |
| 0 vs. 45 | -0,03591 | -0,6719 to 0,6000 | 0,9985 | | |
| 0 vs. 60 | -0,01105 | -0,5606 to 0,5385 | >0,9999 | | |
| **BE(b)** | **T0** | **T15** | **T30** | **T45** | **T60** |
| Mean | 1,000 | 0,901 | 1,026 | 1,023 | 0,984 |
| Std. Error of Mean | 0,158 | 0,214 | 0,179 | 0,107 | 0,087 |
| **Dunnett's multiple comparisons test** | **Mean Diff,** | **95,00% CI of diff,** | **Adjusted P Value** | | |
| 0 vs. 15 | 0,0987 | -0,7036 to 0,9010 | 0,9754 | | |
| 0 vs. 30 | -0,0263 | -0,6895 to 0,6369 | 0,9998 | | |
| 0 vs. 45 | -0,0230 | -0,6740 to 0,6280 | 0,9998 | | |
| 0 vs. 60 | 0,0165 | -0,5607 to 0,5936 | 0,9999 | | |
| **CsO2** | **T0** | **T15** | **T30** | **T45** | **T60** |
| Mean | 1,000 | 1,023 | 1,050 | 1,035 | 1,034 |
| Std. Error of Mean | 0,028 | 0,022 | 0,015 | 0,030 | 0,025 |
| **Dunnett's multiple comparisons test** | **Mean Diff,** | **95,00% CI of diff,** | **Adjusted P Value** | | |
| 0 vs. 15 | -0,0230 | -0,05895 to 0,01299 | 0,201 | | |
| 0 vs. 30 | -0,0502 | -0,1233 to 0,02297 | 0,166 | | |
| 0 vs. 45 | -0,0346 | -0,07627 to 0,007141 | 0,095 | | |
| 0 vs. 60 | -0,0344 | -0,06738 to -0,001347 | **0,043** | | |
| **Na++** | **T0** | **T15** | **T30** | **T45** | **T60** |
| Mean | 1,000 | 1,011 | 1,008 | 1,001 | 0,999 |
| Std. Error of Mean | 0,011 | 0,011 | 0,015 | 0,011 | 0,011 |
| **Dunnett's multiple comparisons test** | **Mean Diff,** | **95,00% CI of diff,** | **Adjusted P Value** | | |
| 0 vs. 15 | -0,011 | -0,03478 to 0,01317 | 0,420 | | |
| 0 vs. 30 | -0,008 | -0,04035 to 0,02354 | 0,775 | | |
| 0 vs. 45 | -0,001 | -0,01479 to 0,01239 | 0,992 | | |
| 0 vs. 60 | 0,001 | -0,01641 to 0,01881 | 0,997 | | |
| **K+** | **T0** | **T15** | **T30** | **T45** | **T60** |
| Mean | 1,000 | 1,071 | 1,108 | 1,146 | 1,179 |
| Std. Error of Mean | 0,044 | 0,072 | 0,084 | 0,046 | 0,057 |
| **Dunnett's multiple comparisons test** | **Mean Diff,** | **95,00% CI of diff,** | **Adjusted P Value** | | |
| 0 vs. 15 | -0,071 | -0,2752 to 0,1335 | 0,606 | | |
| 0 vs. 30 | -0,108 | -0,3420 to 0,1256 | 0,402 | | |
| 0 vs. 45 | -0,146 | -0,2738 to -0,01725 | **0,031** | | |
| 0 vs. 60 | -0,179 | -0,3124 to -0,04581 | **0,016** | | |
| **Ca++** | **T0** | **T15** | **T30** | **T45** | **T60** |
| Mean | 1,000 | 0,954 | 0,951 | 0,974 | 0,989 |
| Std. Error of Mean | 0,021 | 0,017 | 0,024 | 0,027 | 0,015 |
| **Dunnett's multiple comparisons test** | **Mean Diff,** | **95,00% CI of diff,** | **Adjusted P Value** | | |

| | | | | | |
|---|---|---|---|---|---|
| 0 vs. 15 | 0,0465 | -0,05464 to 0,1476 | 0,406 | | |
| 0 vs. 30 | 0,0490 | -0,07968 to 0,1777 | 0,541 | | |
| 0 vs. 45 | 0,0264 | -0,05388 to 0,1066 | 0,643 | | |
| 0 vs. 60 | 0,0113 | -0,05350 to 0,07611 | 0,924 | | |
| **Cl-** | **T0** | **T15** | **T30** | **T45** | **T60** |
| Mean | 1 | 1,015 | 1,026 | 1,012 | 1,007 |
| Std. Error of Mean | 0,02108 | 0,01571 | 0,02578 | 0,0194 | 0,0177 |
| **Dunnett's multiple comparisons test** | **Mean Diff,** | **95,00% CI of diff,** | **Adjusted P Value** | | |
| 0 vs. 15 | -0,015 | -0,07158 to 0,04188 | 0,777 | | |
| 0 vs. 30 | -0,026 | -0,09787 to 0,04506 | 0,563 | | |
| 0 vs. 45 | -0,012 | -0,05723 to 0,03412 | 0,794 | | |
| 0 vs. 60 | -0,007 | -0,05418 to 0,04098 | 0,963 | | |
| **tCO2** | **T0** | **T15** | **T30** | **T45** | **T60** |
| Mean | 1,000 | 0,980 | 0,989 | 1,001 | 0,998 |
| Std. Error of Mean | 0,024 | 0,039 | 0,042 | 0,010 | 0,010 |
| **Dunnett's multiple comparisons test** | **Mean Diff,** | **95,00% CI of diff,** | **Adjusted P Value** | | |
| 0 vs. 15 | 0,0197 | -0,1144 to 0,1538 | 0,955 | | |
| 0 vs. 30 | 0,0112 | -0,1428 to 0,1652 | 0,996 | | |
| 0 vs. 45 | -0,0005 | -0,1066 to 0,1056 | >0,9999 | | |
| 0 vs. 60 | 0,0021 | -0,08119 to 0,08546 | 1,000 | | |
| **Htc** | **T0** | **T15** | **T30** | **T45** | **T60** |
| Mean | 1,000 | 1,098 | 1,110 | 1,129 | 1,123 |
| Std. Error of Mean | 0,065 | 0,092 | 0,092 | 0,053 | 0,051 |
| **Dunnett's multiple comparisons test** | **Mean Diff,** | **95,00% CI of diff,** | **Adjusted P Value** | | |
| 0 vs. 15 | -0,0982 | -0,2719 to 0,07562 | 0,270 | | |
| 0 vs. 30 | -0,1104 | -0,3369 to 0,1161 | 0,365 | | |
| 0 vs. 45 | -0,1288 | -0,2557 to -0,001946 | **0,047** | | |
| 0 vs. 60 | -0,1227 | -0,2654 to 0,02005 | 0,084 | | |
| **cHb** | **T0** | **T15** | **T30** | **T45** | **T60** |
| Mean | 1,000 | 1,092 | 1,110 | 1,130 | 1,134 |
| Std. Error of Mean | 0,067 | 0,093 | 0,093 | 0,053 | 0,053 |
| **Dunnett's multiple comparisons test** | **Mean Diff,** | **95,00% CI of diff,** | **Adjusted P Value** | | |
| 0 vs. 15 | -0,0921 | -0,2598 to 0,07568 | 0,287 | | |
| 0 vs. 30 | -0,1101 | -0,3263 to 0,1060 | 0,336 | | |
| 0 vs. 45 | -0,1300 | -0,2671 to 0,007166 | 0,061 | | |
| 0 vs. 60 | -0,1336 | -0,2763 to 0,009183 | 0,063 | | |
| **Glu** | **T0** | **T15** | **T30** | **T45** | **T60** |
| Mean | 1,000 | 0,943 | 0,947 | 1,011 | 0,977 |
| Std. Error of Mean | 0,149 | 0,163 | 0,174 | 0,215 | 0,211 |
| **Dunnett's multiple comparisons test** | **Mean Diff,** | **95,00% CI of diff,** | **Adjusted P Value** | | |
| 0 vs. 15 | 0,0573 | -0,06392 to 0,1784 | 0,387 | | |
| 0 vs. 30 | 0,0534 | -0,2030 to 0,3099 | 0,874 | | |

| | | | | | |
|---|---|---|---|---|---|
| 0 vs. 45 | -0,0115 | -0,2878 to 0,2649 | 1,000 | | |
| 0 vs. 60 | 0,0229 | -0,2280 to 0,2738 | 0,991 | | |
| **BUN** | **T0** | **T15** | **T30** | **T45** | **T60** |
| Mean | 1,00 | 0,94 | 0,95 | 1,01 | 0,98 |
| Std. Error of Mean | 0,15 | 0,16 | 0,17 | 0,22 | 0,21 |
| **Dunnett's multiple comparisons test** | **Mean Diff,** | **95,00% CI of diff,** | **Adjusted P Value** | | |
| 0 vs. 15 | 0,0573 | -0,06392 to 0,1784 | 0,387 | | |
| 0 vs. 30 | 0,0534 | -0,2030 to 0,3099 | 0,874 | | |
| 0 vs. 45 | -0,0115 | -0,2878 to 0,2649 | 1,000 | | |
| 0 vs. 60 | 0,0229 | -0,2280 to 0,2738 | 0,991 | | |
| **Urea** | **T0** | **T15** | **T30** | **T45** | **T60** |
| Mean | 1 | 1,218 | 1,277 | 1,317 | 1,317 |
| Std. Error of Mean | 0,227 | 0,291 | 0,323 | 0,329 | 0,327 |
| **Dunnett's multiple comparisons test** | **Mean Diff,** | **95,00% CI of diff,** | **Adjusted P Value** | | |
| 0 vs. 15 | -0,218 | -0,4880 to 0,05231 | 0,103 | | |
| 0 vs. 30 | -0,277 | -0,7158 to 0,1614 | 0,206 | | |
| 0 vs. 45 | -0,317 | -0,7217 to 0,08808 | 0,113 | | |
| 0 vs. 60 | -0,317 | -0,7111 to 0,07740 | 0,104 | | |
| **Crea** | **T0** | **T15** | **T30** | **T45** | **T60** |
| Mean | 1,000 | 1,025 | 1,096 | 1,110 | 0,982 |
| Std. Error of Mean | 0,150 | 0,154 | 0,133 | 0,098 | 0,223 |
| **Dunnett's multiple comparisons test** | **Mean Diff,** | **95,00% CI of diff,** | **Adjusted P Value** | | |
| 0 vs. 15 | -0,025 | -0,3679 to 0,3169 | 0,996 | | |
| 0 vs. 30 | -0,096 | -0,5700 to 0,3783 | 0,884 | | |
| 0 vs. 45 | -0,110 | -0,4458 to 0,2256 | 0,644 | | |
| 0 vs. 60 | 0,018 | -0,7438 to 0,7796 | 1,000 | | |

**Table A1.1 – Blood gas analysis comparison dataset.**

| **Mucosae** | **Antrum** | **Corpus** | **Fundus** | **Removed Region** |
|---|---|---|---|---|
| Mean | 1,000 | 1,909 | 1,455 | 2,455 |
| Std. Error of Mean | 0,168 | 0,234 | 0,230 | 0,234 |
| **Dunnett's multiple comparisons test** | **Mean Diff,** | **95,00% CI of diff,** | **Adjusted P Value** | |
| Antrum vs Corpus | -0,909 | -1,692 to -0,1259 | **0,021** | |
| Antrum vs Fundus | -0,455 | -1,238 to 0,3287 | 0,343 | |
| Antrum vs Removed region | -1,455 | -2,238 to -0,6713 | **0,000** | |
| **Sub-Mucosae** | **Antrum** | **Corpus** | **Fundus** | **Removed Region** |
| Mean | 1,000 | 1,429 | 2,571 | 2,286 |
| Std. Error of Mean | 0,143 | 0,286 | 0,221 | 0,361 |
| **Dunnett's multiple comparisons test** | **Mean Diff,** | **95,00% CI of diff,** | **Adjusted P Value** | |

| | | | | |
|---|---|---|---|---|
| Antrum vs Corpus | -0,429 | -1,382 to 0,5248 | 0,538 | |
| Antrum vs Fundus | -1,571 | -2,525 to -0,6181 | **0,001** | |
| Antrum vs Removed region | -1,286 | -2,239 to -0,3324 | **0,007** | |
| **Muscolaris Externa** | **Antrum** | **Corpus** | **Fundus** | **Removed Region** |
| Mean | 1 | 8 | 3,5 | 5 |
| Std. Error of Mean | 1 | 1,265 | 0,922 | 1 |
| **Dunnett's multiple comparisons test** | **Mean Diff,** | **95,00% CI of diff,** | **Adjusted P Value** | |
| Antrum vs Corpus | -7 | -10,79 to -3,210 | **0,0004** | |
| Antrum vs Fundus | -2,5 | -6,290 to 1,290 | 0,2505 | |
| Antrum vs Removed region | -4 | -7,790 to -0,2104 | **0,0373** | |
| **Sierosa** | **Antrum** | **Corpus** | **Fundus** | **Removed Region** |
| Mean | 1,000 | 1,167 | 1,000 | 1,056 |
| Std. Error of Mean | 0,122 | 0,075 | 0,211 | 0,102 |
| **Dunnett's multiple comparisons test** | **Mean Diff,** | **95,00% CI of diff,** | **Adjusted P Value** | |
| Antrum vs Corpus | -0,167 | -0,6597 to 0,3263 | 0,727 | |
| Antrum vs Fundus | 0,000 | -0,4930 to 0,4930 | >0,9999 | |
| Antrum vs Removed region | -0,056 | -0,5485 to 0,4374 | 0,984 | |
| **Histology Score** | **Antrum** | **Corpus** | **Fundus** | **Removed Region** |
| Mean | 1,000 | 1,789 | 1,553 | 1,895 |
| Std. Error of Mean | 0,078 | 0,097 | 0,170 | 0,153 |
| **Dunnett's multiple comparisons test** | **Mean Diff,** | **95,00% CI of diff,** | **Adjusted P Value** | |
| Antrum vs Corpus | -0,790 | -1,257 to -0,3220 | **0,001** | |
| Antrum vs Fundus | -0,553 | -1,020 to -0,08511 | **0,0187** | |
| Antrum vs Removed region | -0,895 | -1,362 to -0,4272 | **0,0003** | |

**Table A1.2 – Histologic analysis comparison dataset.**

| **Multiple comparisons ANTRUM vs other ROIs** | | | | |
|---|---|---|---|---|
| | **Dunnett's multiple comparisons test** | **Mean Diff,** | **95,00% CI of diff,** | **Adjusted P Value** |
| **T0** | Antrum vs. Corpus | 0,012 | -0,9192 to 0,9424 | >0,9999 |
| | Antrum vs. Fundus | -0,116 | -1,015 to 0,7831 | 0,9674 |
| | Antrum vs. Removed Region | 0,046 | -0,7201 to 0,8129 | 0,9965 |
| **T15** | Antrum vs. Corpus | -0,557 | -1,388 to 0,2750 | 0,2111 |
| | Antrum vs. Fundus | -0,475 | -1,492 to 0,5417 | 0,4603 |
| | Antrum vs. Removed Region | -4,046 | -6,756 to -1,337 | **0,0091** |
| **T30** | Antrum vs. Corpus | 0,070 | -0,6510 to 0,7901 | 0,9856 |

| | | | | |
|---|---|---|---|---|
| | Antrum vs. Fundus | -0,673 | -1,488 to 0,1435 | 0,1068 |
| | Antrum vs. Removed Region | -5,009 | -6,719 to -3,298 | **0,0003** |
| **T45** | Antrum vs. Corpus | 0,301 | -0,3981 to 1,001 | 0,5205 |
| | Antrum vs. Fundus | -0,278 | -1,123 to 0,5663 | 0,6864 |
| | Antrum vs. Removed Region | -5,264 | -7,365 to -3,162 | **0,0007** |
| **T60** | Antrum vs. Corpus | -0,104 | -0,7503 to 0,5416 | 0,9375 |
| | Antrum vs. Fundus | -0,673 | -1,542 to 0,1975 | 0,1367 |
| | Antrum vs. Removed Region | -7,548 | -9,878 to -5,218 | **0,0002** |
| **Multiple comparisons CORPUS vs other ROIs** | | | | |
| | **Dunnett's multiple comparisons test** | **Mean Diff,** | **95,00% CI of diff,** | **Adjusted P Value** |
| **T0** | Corpus vs. Antrum | -0,012 | -0,9424 to 0,9192 | >0,9999 |
| | Corpus vs. Fundus | -0,128 | -1,170 to 0,9152 | 0,9734 |
| | Corpus vs. Removed Region | 0,035 | -0,9222 to 0,9917 | 0,9992 |
| **T15** | Corpus vs. Antrum | 0,557 | -0,2750 to 1,388 | 0,2111 |
| | Corpus vs. Fundus | 0,081 | -0,8635 to 1,026 | 0,9894 |
| | Corpus vs. Removed Region | -3,490 | -6,208 to -0,7715 | **0,0186** |
| **T30** | Corpus vs. Antrum | -0,070 | -0,7901 to 0,6510 | 0,9856 |
| | Corpus vs. Fundus | -0,742 | -1,630 to 0,1461 | 0,1046 |
| | Corpus vs. Removed Region | -5,078 | -6,788 to -3,368 | **0,0002** |
| **T45** | Corpus vs. Antrum | -0,301 | -1,001 to 0,3981 | 0,5205 |
| | Corpus vs. Fundus | -0,580 | -1,449 to 0,2893 | 0,2132 |
| | Corpus vs. Removed Region | -5,565 | -7,664 to -3,466 | **0,0005** |
| **T60** | Corpus vs. Antrum | 0,104 | -0,5416 to 0,7503 | 0,9375 |
| | Corpus vs. Fundus | -0,568 | -1,374 to 0,2373 | 0,1699 |
| | Corpus vs. Removed Region | -7,443 | -9,786 to -5,101 | **0,0003** |
| **Multiple comparisons FUNDUS vs other ROIs** | | | | |
| | **Dunnett's multiple comparisons test** | **Mean Diff,** | **95,00% CI of diff,** | **Adjusted P Value** |
| **T0** | Fundus vs. Antrum | 0,116 | -0,7831 to 1,015 | 0,9674 |
| | Fundus vs. Corpus | 0,128 | -0,9152 to 1,170 | 0,9734 |
| | Fundus vs. Removed Region | 0,162 | -0,7652 to 1,090 | 0,9281 |
| **T15** | Fundus vs. Antrum | 0,475 | -0,5417 to 1,492 | 0,4603 |
| | Fundus vs. Corpus | -0,081 | -1,026 to 0,8635 | 0,9894 |
| | Fundus vs. Removed Region | -3,571 | -6,277 to -0,8646 | **0,0155** |
| **T30** | Fundus vs. Antrum | 0,673 | -0,1435 to 1,488 | 0,1068 |
| | Fundus vs. Corpus | 0,742 | -0,1461 to 1,630 | 0,1046 |
| | Fundus vs. Removed Region | -4,336 | -6,054 to -2,619 | **0,0004** |

| | | | | |
|---|---|---|---|---|
| **T45** | Fundus vs. Antrum | 0,278 | -0,5663 to 1,123 | 0,6864 |
| | Fundus vs. Corpus | 0,580 | -0,2893 to 1,449 | 0,2132 |
| | Fundus vs. Removed Region | -4,986 | -7,084 to -2,887 | **0,0007** |
| **T60** | Fundus vs. Antrum | 0,673 | -0,1975 to 1,542 | 0,1367 |
| | Fundus vs. Corpus | 0,568 | -0,2373 to 1,374 | 0,1699 |
| | Fundus vs. Removed Region | -6,875 | -9,201 to -4,550 | **0,0002** |
| **Multiple comparisons REMOVED REGION vs other ROIs** | | | | |
| | **Dunnett's multiple comparisons test** | **Mean Diff,** | **95,00% CI of diff,** | **Adjusted P Value** |
| **T0** | Removed Region vs. Antrum | -0,046 | -0,8129 to 0,7201 | 0,9965 |
| | Removed Region vs. Corpus | -0,035 | -0,9917 to 0,9222 | 0,9992 |
| | Removed Region vs. Fundus | -0,162 | -1,090 to 0,7652 | 0,9281 |
| **T15** | Removed Region vs. Antrum | 4,046 | 1,337 to 6,756 | **0,0091** |
| | Removed Region vs. Corpus | 3,490 | 0,7715 to 6,208 | **0,0186** |
| | Removed Region vs. Fundus | 3,571 | 0,8646 to 6,277 | **0,0155** |
| **T30** | Removed Region vs. Antrum | 5,009 | 3,298 to 6,719 | **0,0003** |
| | Removed Region vs. Corpus | 5,078 | 3,368 to 6,788 | **0,0002** |
| | Removed Region vs. Fundus | 4,336 | 2,619 to 6,054 | **0,0004** |
| **T45** | Removed Region vs. Antrum | 5,264 | 3,162 to 7,365 | **0,0007** |
| | Removed Region vs. Corpus | 5,565 | 3,466 to 7,664 | **0,0005** |
| | Removed Region vs. Fundus | 4,986 | 2,887 to 7,084 | **0,0007** |
| **T60** | Removed Region vs. Antrum | 7,548 | 5,218 to 9,878 | **0,0002** |
| | Removed Region vs. Corpus | 7,443 | 5,101 to 9,786 | **0,0003** |
| | Removed Region vs. Fundus | 6,875 | 4,550 to 9,201 | **0,0002** |

**Table A1.3 – Local capillary lactates comparison dataset.**

| **Multiple comparisons ANTRUM vs other ROIs** | | | | |
|---|---|---|---|---|
| | **Dunnett's multiple comparisons test** | **Mean Diff,** | **95,00% CI of diff,** | **Adjusted P Value** |
| **T0** | Antrum vs. Corpus | -0,062 | -0,1591 to 0,03515 | 0,2996 |
| | Antrum vs. Fundus | -0,07479 | -0,1719 to 0,02236 | 0,1686 |
| | Antrum vs. Removed Region | -0,0561 | -0,1532 to 0,04105 | 0,3784 |
| **T15** | Antrum vs. Corpus | -0,1549 | -0,2521 to -0,05778 | **0,0007** |
| | Antrum vs. Fundus | -0,275 | -0,3721 to -0,1778 | **<0,0001** |
| | Antrum vs. Removed Region | 0,2584 | 0,1612 to 0,3555 | **<0,0001** |
| **T30** | Antrum vs. Corpus | -0,1918 | -0,2889 to -0,09464 | **<0,0001** |
| | Antrum vs. Fundus | -0,2354 | -0,3325 to -0,1382 | **<0,0001** |
| | Antrum vs. Removed Region | 0,3128 | 0,2157 to 0,4100 | **<0,0001** |

| | | | | |
|---|---|---|---|---|
| **T45** | Antrum vs. Corpus | -0,1999 | -0,2971 to -0,1028 | **<0,0001** |
| | Antrum vs. Fundus | -0,2263 | -0,3235 to -0,1292 | **<0,0001** |
| | Antrum vs. Removed Region | 0,3289 | 0,2318 to 0,4261 | **<0,0001** |
| **T60** | Antrum vs. Corpus | -0,2416 | -0,3387 to -0,1444 | **<0,0001** |
| | Antrum vs. Fundus | -0,2421 | -0,3393 to -0,1450 | **<0,0001** |
| | Antrum vs. Removed Region | 0,3231 | 0,2260 to 0,4203 | **<0,0001** |
| **Multiple comparisons CORPUS vs other ROIs** | | | | |
| | **Dunnett's multiple comparisons test** | **Mean Diff,** | **95,00% CI of diff,** | **Adjusted P Value** |
| **T0** | Corpus vs. Antrum | 0,062 | -0,03515 to 0,1591 | 0,2996 |
| | Corpus vs. Fundus | -0,01279 | -0,1099 to 0,08436 | 0,9792 |
| | Corpus vs. Removed Region | 0,005903 | -0,09125 to 0,1031 | 0,9979 |
| **T15** | Corpus vs. Antrum | 0,1549 | 0,05778 to 0,2521 | **0,0007** |
| | Corpus vs. Fundus | -0,12 | -0,2172 to -0,02289 | **0,0111** |
| | Corpus vs. Removed Region | 0,4133 | 0,3162 to 0,5105 | **<0,0001** |
| **T30** | Corpus vs. Antrum | 0,1918 | 0,09464 to 0,2889 | **<0,0001** |
| | Corpus vs. Fundus | -0,04358 | -0,1407 to 0,05357 | 0,5771 |
| | Corpus vs. Removed Region | 0,5046 | 0,4075 to 0,6018 | **<0,0001** |
| **T45** | Corpus vs. Antrum | 0,1999 | 0,1028 to 0,2971 | **<0,0001** |
| | Corpus vs. Fundus | -0,02643 | -0,1236 to 0,07072 | 0,854 |
| | Corpus vs. Removed Region | 0,5288 | 0,4317 to 0,6260 | **<0,0001** |
| **T60** | Corpus vs. Antrum | 0,2416 | 0,1444 to 0,3387 | **<0,0001** |
| | Corpus vs. Fundus | -0,0005538 | -0,09770 to 0,09660 | >0,9999 |
| | Corpus vs. Removed Region | 0,5647 | 0,4676 to 0,6619 | **<0,0001** |
| **Multiple comparisons FUNDUS vs other ROIs** | | | | |
| | **Dunnett's multiple comparisons test** | **Mean Diff,** | **95,00% CI of diff,** | **Adjusted P Value** |
| **T0** | Fundus vs. Antrum | 0,07479 | -0,02236 to 0,1719 | 0,1686 |
| | Fundus vs. Corpus | 0,01279 | -0,08436 to 0,1099 | 0,9792 |
| | Fundus vs. Removed Region | 0,01869 | -0,07846 to 0,1158 | 0,9402 |
| **T15** | Fundus vs. Antrum | 0,275 | 0,1778 to 0,3721 | **<0,0001** |
| | Fundus vs. Corpus | 0,12 | 0,02289 to 0,2172 | **0,0111** |
| | Fundus vs. Removed Region | 0,5334 | 0,4362 to 0,6305 | **<0,0001** |
| **T30** | Fundus vs. Antrum | 0,2354 | 0,1382 to 0,3325 | **<0,0001** |
| | Fundus vs. Corpus | 0,04358 | -0,05357 to 0,1407 | 0,5771 |
| | Fundus vs. Removed Region | 0,5482 | 0,4510 to 0,6453 | **<0,0001** |
| **T45** | Fundus vs. Antrum | 0,2263 | 0,1292 to 0,3235 | **<0,0001** |

| | | | | |
|---|---|---|---|---|
| | Fundus vs. Corpus | 0,02643 | -0,07072 to 0,1236 | 0,854 |
| | Fundus vs. Removed Region | 0,5553 | 0,4581 to 0,6524 | **<0,0001** |
| **T60** | Fundus vs. Antrum | 0,2421 | 0,1450 to 0,3393 | **<0,0001** |
| | Fundus vs. Corpus | 0,0005538 | -0,09660 to 0,09770 | >0,9999 |
| | Fundus vs. Removed Region | 0,5653 | 0,4681 to 0,6624 | **<0,0001** |
| **Multiple comparisons REMOVED REGION vs other ROIs** | | | | |
| | **Dunnett's multiple comparisons test** | **Mean Diff,** | **95,00% CI of diff,** | **Adjusted P Value** |
| **T0** | Removed Region vs. Antrum | 0,0561 | -0,04105 to 0,1532 | 0,3784 |
| | Removed Region vs. Corpus | -0,005903 | -0,1031 to 0,09125 | 0,9979 |
| | Removed Region vs. Fundus | -0,01869 | -0,1158 to 0,07846 | 0,9402 |
| **T15** | Removed Region vs. Antrum | -0,2584 | -0,3555 to -0,1612 | **<0,0001** |
| | Removed Region vs. Corpus | -0,4133 | -0,5105 to -0,3162 | **<0,0001** |
| | Removed Region vs. Fundus | -0,5334 | -0,6305 to -0,4362 | **<0,0001** |
| **T30** | Removed Region vs. Antrum | -0,3128 | -0,4100 to -0,2157 | **<0,0001** |
| | Removed Region vs. Corpus | -0,5046 | -0,6018 to -0,4075 | **<0,0001** |
| | Removed Region vs. Fundus | -0,5482 | -0,6453 to -0,4510 | **<0,0001** |
| **T45** | Removed Region vs. Antrum | -0,3289 | -0,4261 to -0,2318 | **<0,0001** |
| | Removed Region vs. Corpus | -0,5288 | -0,6260 to -0,4317 | **<0,0001** |
| | Removed Region vs. Fundus | -0,5553 | -0,6524 to -0,4581 | **<0,0001** |
| **T60** | Removed Region vs. Antrum | -0,3231 | -0,4203 to -0,2260 | **<0,0001** |
| | Removed Region vs. Corpus | -0,5647 | -0,6619 to -0,4676 | **<0,0001** |
| | Removed Region vs. Fundus | -0,5653 | -0,6624 to -0,4681 | **<0,0001** |

**Table A1.4 – $StO_2$ comparison dataset.**

# Scientific contributions

- Journal Publications

Cinelli L., Felli E., Baratelli L., **Ségaud S.**, Baiocchini A., Okamoto N., Rodriguez-Luna M.R., Elmore U., Rosati R., Partelli S., Marescaux J., Gioux S., Diana M., ''Single snapshot imaging of optical properties (SSOP) for perfusion assessment during gastric conduit creation for esophagectomy: An experimental study on pigs'', Cancers , Volume 13 , Number 23, 2021.

(In preparation) Rodriguez-Luna M.R., Okamoto N., Cinelli L., Baratelli L, **Ségaud S.**, Rodriguez-Gomez A., Bannone E., Zonoobi E., Keller D.S., Marescaux J., Diana M., Gioux S., ''Quantification of bowel ischaemia using real-time single snapshot imaging of optical properties''

(In preparation) **Ségaud S.**, Baratelli L., Diana M., Lecler S., Gioux S., ''Novel Multimodal Imaging Platform for Intraoperative Blood Perfusion Assessment''

- Oral Communications

SPIE Photonics Europe 2022

- (accepted) ''Intraoperative blood perfusion assessment using real-time oxygenation imaging'', **Ségaud S.**, Baratelli L., Diana M., Lecler S., Gioux S.

European Conferences on Biomedical Optics (ECBO) 2021

- (invited talk) '' Multimodal Imaging Platform for Surgery: Application to Tissue Status Assessment'', **Ségaud S.**, Baratelli L., Aguenounon E., van Manen L., Muynck L.D.A.N., Mieog J.S.D., Vahrmeijer A.L., Diana M., Lecler S., Gioux S.

SPIE Photonics West BIOS 2021

- ''Multimodal imaging platform for image-guided surgery: application to blood perfusion assessment'', **Ségaud S.**, Aguenounon E., Angelo J., Gravelyn S., Waxin H., Zorn L., Lamy J., Torregrossa M., Diana M., Lecler S., Gioux S.
- ''Widefield quantitative fluorescence imaging applied to tumor margin assessment'', **Ségaud S.**, van Manen L., Muynck L.D.A.N., Mieog J.S.D., Vahrmeijer A.L., Lecler S., Gioux S.

GDR ISIS & GDR ONDES – Journées Imagerie Optique Non-Conventionnelle (JIONC) 2021

- ''Blood perfusion assessment in the small bowel using a novel multimodal imaging platform'', **Ségaud S.**, Baratelli L., Aguénounon E., Diana M., Lecler S., Gioux S.

8ème journées scientifiques de la Fédération de Médecine Translationnelle de Strasbourg (FMTS) 2021

- ''Novel Multimodal Imaging Platform for Intraoperative Tissue Status Assessment'', **Ségaud S.**, Baratelli L., Aguénounon E., Diana M., Lecler S., Gioux S.

Silvère SÉGAUD

# Multispectral Optical Imaging in real-time for surgery


## Abstract

The deployment of technology in operating rooms dramatically accelerated over the last decades. More precisely, the surgeons' ability to distinguish healthy from diseased tissues is still mostly based on their own subjective perception. As tissue status assessment is of upmost importance in oncologic surgery, both for tumor resection and reconstruction procedures, the ability to assess the tissues intraoperatively and in real-time over a large field is crucial for surgical act guidance. The lack of tools for biological intraoperative tissue status assessment has been the main source of motivation for this thesis work. A clinically-compatible imaging platform has been developed for oxygenation and fluorescence imaging in real-time. The capability of the platform to detect and quantify ischemia has been demonstrated through preclinical trials, by comparison with standard of care methods. Furthermore, the multimodal nature of the developed imaging device has been exploited by combining endogenous imaging of optical properties with exogenous fluorescence imaging, in the context of oncologic surgery. A fluorescence quantification technique was validated in preclinical trials with colorectal and pancreatic cancer models, highlighting the limitations of conventional fluorescence imaging.


**Keywords**: Image-guided surgery, Oxygenation imaging, Fluorescence imaging, Clinical translation, Spatial Frequency Domain Imaging, Diffuse optical imaging


## Résumé

Le développent technologique des salles d'opérations a accéléré de manière spectaculaire ces dernières années. Cependant, la capacité des praticiens à différencier les tissus sains des tissus malsains à travers le champ chirurgical est principalement basée sur leur propre perception et expérience. Ceci est pourtant d'une importance majeure en chirurgie oncologique, tant pour la résection de tumeurs que pour les actes de reconstruction. C'est pourquoi la capacité d'évaluer le statut des tissus biologiques à travers des zones étendues en temps réel est cruciale. Le manque d'outils permettant l'évaluation de la viabilité des tissus biologique dans un contexte intra opératoire a été la motivation principale de ce projet. Un prototype d'imageur multimodal clinique a été développé pour l'imagerie d'oxygénation et de fluorescence en temps-réel. La capacité de la plateforme à quantifier l'ischémie a été démontrée lors de tests précliniques, par comparaison avec les méthodes standards. Le caractère multimodal de la plateforme d'imagerie a été exploité pour combiner l'imagerie endogène mesurant les propriétés optiques des tissus et l'imagerie exogène par fluorescence, dans le cadre de la chirurgie du cancer. Une méthode de quantification a été employée lors d'essais précliniques sur des modèles de cancers colorectaux et pancréatiques, mettant en évidence les défaillances de l'imagerie de fluorescence conventionnelle.


**Mots-clés** : Chirurgie guidée par l'image, Imagerie d'oxygénation, Imagerie de fluorescence, Translation clinique, Spatial Frequency Domain Imaging, Optique diffuse